Charles University in Prague
Faculty of Mathematics and Physics

MASTER THESIS

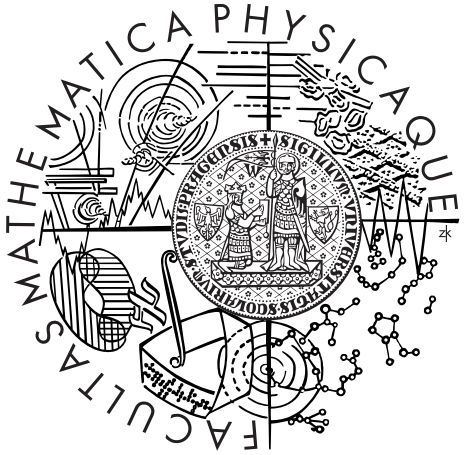

Vít Kučera

Studium produkce jetů v experimentu ALICE na urychlovači LHC

Study of jet production with the ALICE experiment at the LHC

Institute of Particle and Nuclear Physics

Supervisor of the master thesis: RNDr. Jana Bielčíková, Ph.D.

Study programme: Physics

Specialisation: Nuclear and Subnuclear Physics

Prague 2012

Acknowledgments

I would like to express my sincere gratitude to my supervisor Jana Bielčíková for her support, help, patience, for inspiring discussions and for her time. I am very grateful to Marta Verweij who helped me a lot with understanding track reconstruction and jet analysis. I wish to thank Michal Vajzer, Dagmar Adamová, Filip Křížek and Christian Klein-Bösing for their help with overcoming technical difficulties. I wish to thank Mario Sitta and Leonardo Milano for giving me opportunity to get involved in monitoring detectors in the ALICE experiment. I wish to thank Michal Šumbera, Jaroslav Bielčík, Boris Tomášik and Vojtěch Petráček for their direct or indirect help with my progress. Special acknowledgement belongs to my parents for their continuous support and encouragement.

In memory of Šupír,
my best animal friend.

I declare that I carried out this master thesis independently, and only with the cited sources, literature and other professional sources.

I understand that my work relates to the rights and obligations under the Act No. 121/2000 Coll., the Copyright Act, as amended, in particular the fact that the Charles University in Prague has the right to conclude a license agreement on the use of this work as a school work pursuant to Section 60 paragraph 1 of the Copyright Act.

In Prague, August 3, 2012 signature of the author

Název práce: Studium produkce jetů v experimentu ALICE na urychlovači LHC

Autor: Vít Kučera

Katedra: Ústav částicové a jaderné fyziky

Vedoucí diplomové práce: RNDr. Jana Bielčíková, Ph.D., Ústav jaderné fyziky AV ČR, v.v.i.

Abstrakt: Teorie silné interakce, kvantová chromodynamika, předpovídá fázový přechod mezi hadronovou hmotou a kvarkovým-gluonovým plazmatem, v němž jsou kvarky a gluony volné. Předpokládá se, že takový stav hmoty lze vytvořit v ultra-relativistických srážkách těžkých iontů. Jety z partonů, které interagují se silně interagující hmotou vzniklou ve srážkách těžkých iontů, mohou být použity jako sondy ke zkoumání tohoto prostředí. Experiment ALICE, umístěný na Velkém hadronovém srážeči (LHC) v CERN, umožňuje použití jetů ke zkoumání prostředí vytvořeného ve srážkách těžkých iontů. V práci je předložena analýza dat naměřených experimentem ALICE v roce 2010 ve srážkách jader olova při energii $\sqrt{s_{\mathrm{NN}}} = 2.76$ TeV. Výsledky této analýzy jsou předloženy ve studii jetů rekonstruovaných pomocí algoritmů k_{t} a anti-k_{t}. Studie zahrnuje analýzu drah, analýzu pozadí a zaměřuje se na analýzu inkluzivních spekter jetů. Jsou zkoumány rozličné vlastnosti jetových spekter včetně pozměnění jetů v centrálních srážkách vyjádřeného poměrem R_{CP}. Také je předložen souhrn autorova krátkodobého projektu týkajícího se sledování křemíkových driftových detektorů experimentu ALICE.

Klíčová slova: těžké ionty, jety, jetové algoritmy

Title: Study of jet production with the ALICE experiment at the LHC

Author: Vít Kučera

Department: Institute of Particle and Nuclear Physics

Supervisor: RNDr. Jana Bielčíková, Ph.D., Nuclear Physics Institute of the ASCR, v.v.i.

Abstract: The theory of strong interaction, quantum chromodynamics, predicts a phase transition between hadronic matter and the quark-gluon plasma where quarks and gluons are deconfined. This state of matter is expected to be created in ultra-relativistic collisions of heavy ions. Jets from partons which interact with the strongly interacting matter created in heavy-ion collisions can be used as probes to study this medium. The ALICE experiment installed at the Large Hadron Collider at CERN enables using jets to study medium in heavy-ion collisions. An analysis of data measured with the ALICE experiment in 2010 in lead nuclei collisions at energy $\sqrt{s_{\mathrm{NN}}} = 2.76$ TeV is presented in the thesis. The results of this analysis are presented in a study of jets reconstructed with the k_{t} and anti-k_{t} algorithms. The study includes an analysis of tracks, an analysis of background and focuses on an analysis of inclusive jet spectra. Various aspects of jet spectra are studied including modification of jets in the central collisions expressed by the ratio R_{CP}. Also a summary of author's short-term project on monitoring the Silicon Drift Detectors of the ALICE experiment is presented.

Keywords: heavy ions, jets, jet algorithms

Contents

Introduction

According to current theories, our Universe originated in a "Big Bang" and due to extreme initial conditions the quarks and gluons, which constitute hadrons, were deconfined in a state called "quark-gluon plasma" (QGP) up to a few microseconds after the Big Bang. When the energy density of the Universe fell below the critical value $e_{\mathrm{cr}} \approx 1\ \mathrm{GeV/fm^3}$ and its temperature decreased below $T_{\mathrm{cr}} \approx 170\ \mathrm{MeV}$, coloured degrees of freedom became confined into colour singlet bound states of quarks, antiquarks and gluons, i.e. the first hadrons [1].

The phase transition between hadronic matter and the QGP is predicted by the theory of strong interaction — quantum chromodynamics (QCD). QCD and results of recent experiments indicate that the QGP can be recreated in ultra-relativistic collisions of heavy nuclei ("nucleus-nucleus collisions", "heavy-ion collisions").

Strongly interacting matter has been studied experimentally for the last 30 years with only few research facilities. The most encouraging results have been reached at the Super Proton Synchrotron (SPS) at CERN and at the Relativistic Heavy Ion Collider (RHIC) at the Brookhaven National Laboratory. The research continues at the Large Hadron Collider (LHC) at CERN. The crucial step was made in November 2010, when the LHC produced the first lead-lead ("Pb + Pb") collisions at a centre-of-mass energy per nucleon pair $\sqrt{s_{\mathrm{NN}}} = 2.76\ \mathrm{TeV}$. This represents an increase of more than one order of magnitude over the highest energy previously reached [2].

Properties of the unknown state of strongly interacting matter may be studied by using jets. Production of jets is well described theoretically. When propagating through the medium created in a heavy-ion collision, jets are expected to be modified relative to proton collisions by interaction with this medium.

The ALICE experiment at the LHC was designed to study medium created in heavy-ion collisions. Its features enable to fulfil this task using different probes including fully reconstructed jets.

This diploma thesis presents a study of jets reconstructed in lead-nuclei collisions at the centre-of-mass energy per nucleon pair $\sqrt{s_{\mathrm{NN}}} = 2.76\ \mathrm{TeV}$, measured with ALICE in 2010.

The objectives of the thesis are:

1. to reconstruct jets using sequential recombination algorithms k_{t}, anti-k_{t},

2. to study background and its fluctuations,

3. to study inclusive spectra of jets.

In Chapter 1, I present the motivation for studying heavy-ion collisions and current status of knowledge of the strongly interacting matter and of the way it affects fast partons. In Chapter 2, I present the motivation for studying jets in heavy-ion collisions including the methods of their reconstruction. In Chapter 3, I present the experiment ALICE, describe the main features of the detector components, charged particle reconstruction and determination of collision centrality. In Chapter 4, I present a summary of my mini-project concerning monitoring the

Silicon Drift Detectors in ALICE. In Chapter 5, I present tools used in my analysis, describe in detail structure of the analysis, its components and settings. In Chapter 6, I present the results of my analysis.

1 Introduction to physics of heavy-ion collisions

This chapter introduces some basic facts about the motivation and aspects of studying strongly interacting matter at high energy densities and high temperatures.

1.1 The phase diagram of strongly interacting matter

Fig. 1.1 shows the phase diagram of strongly interacting matter in the plane of temperature T vs baryon chemical potential μ_{B}. At temperatures above the critical value T_{cr}, quarks, antiquarks and gluons in hadronic matter are expected to be deconfined. The motion of deconfined partons is no longer restricted by the strong interaction to the dimensions of nucleons. These partons are free to move in the whole volume of the plasma [3]. Deconfinement results in the release of a large

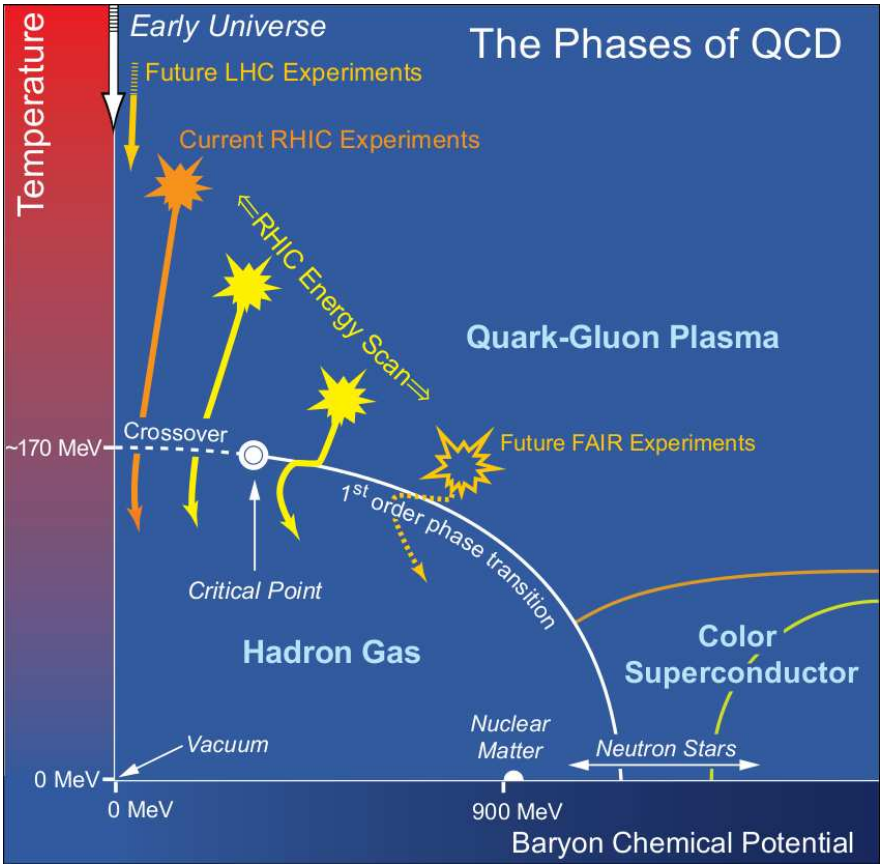

Figure 1.1: Phase diagram of strongly interacting matter [4].

number of gluons which can produce additional quark-antiquark pairs and enable the system to establish chemical balance among quarks, antiquarks and gluons. Above T_{cr}, the dynamical masses of quarks get lower which lowers the threshold

for production of quark-antiquark pairs. This affects the way thermal processes tune the abundances of quarks and antiquarks of different flavours during the short time of a heavy-ion collision [1].

Heavy-ion collisions represent a tool for exploring different areas in this diagram. For a lead nucleus there is $T = 0$ MeV and $\mu_B \approx m_N$. The collision evolution starts at the coordinates of cold nuclear matter, continues through a non-equilibrium stage, which cannot be drawn in the diagram, then the system possibly thermalises and reappears in the phase diagram, as depicted for various experiments in the phase diagram, at a high temperature [1].

When the centre-of-mass energy of collision increases, a decreasing fraction of the beam energy and of the colliding nucleons get stopped in the centre-of-mass system. The volume of created matter (the "collision fireball") therefore contains fewer of the original baryons and becomes more symmetric in terms of numbers of baryons vs of antibaryons (i.e. μ_B decreases) [1].

Although the conditions in the nuclei collisions at the LHC are still far from those in the early Universe, the created medium may be for all practical purposes considered a "baryon-free" (i.e. $\mu_B = 0$ GeV) QCD matter [1].

1.2 The space-time evolution of a collision

The key stages of relativistic heavy-ion collisions are: thermalisation, expansion and decoupling [1].

Partons created in the primary nuclei collisions rescatter of each other both elastically and inelastically and create a form of dense, strongly interacting matter. When it thermalises quickly enough and at sufficiently large energy density, this matter is a quark-gluon plasma [1].

Thermal pressure of the thermalised system leads to collective hydrodynamic expansion of the collision fireball which results in cooling and decrease of energy density. When the energy density of the system reaches the critical value of $e_{cr} \approx 1\ \mathrm{GeV/fm^3}$, the medium constituents undergo a phase transition through hadronisation and the partons convert to hadrons [1].

Created hadrons rescatter with each other and distances between them increase. When the average distance between hadrons exceeds the range of the strong interactions, scattering stops and the hadrons decouple ("freeze out") [1].

In this sense heavy-ion collisions do not provide conditions for studying the process of deconfinement, but rather for probing the confinement phase transition, which corresponds to the evolution of the early Universe [1].

1.3 Centrality

Properties of the final state in a collision of nuclei strongly depend on the impact parameter of that collision. The impact parameter b is the distance between centres of colliding nuclei in the transverse plane with respect to the collision axis. Since it cannot be measured directly, other quantities, directly related to the impact parameter, are introduced to describe geometry of a nuclei collision.

The most frequently used parameters are centrality, number N_{part} of participating nucleons (i.e. nucleons which undergo at least one inelastic nucleon-nucleon

collision [5]) and number N_{coll} of binary collisions of nucleons.

Centrality is expressed as percentage of the total geometric cross section of the collision of two nuclei. The scale begins at the most central collisions, i.e. centrality of 0 % corresponds to the most central collision and centrality of 100 % corresponds to the most peripheral collision.

Numbers N_{part} and N_{coll} are calculated in the Glauber model and determine, via simulations, the number of charged particles created in the nuclei collision (charged multiplicity) [5]. This number may be measured as signal in a detector. The soft processes are sensitive to the value of N_{part}, whereas N_{coll} is a scale for the hard processes [1].

According to QCD, hard particles are produced on short time scales and their production in the nucleon collisions therefore happens incoherently [1], so the nucleus-nucleus collision may be considered as a superposition of independent nucleon-nucleon interactions [6]. Thus the production of partons with high transverse momenta p_{T} can be calculated perturbatively and is proportional to the number of binary nucleon-nucleon collisions which for a nucleus-nucleus collision A + B at impact parameter b is given by

$$N_{\mathrm{coll}}(b) = \sigma_0 \int \rho_{\mathrm{coll}}\left(x, y, b\right) \mathrm{d}x\, \mathrm{d}y \tag{1.1}$$

where σ_0 is the total inelastic nucleon-nucleon cross section, the integral is over the transverse plane,

$$\rho_{\mathrm{coll}}\left(x, y, b\right) = T_{\mathrm{A}}\left(x + b/2, y\right) T_{\mathrm{B}}\left(x - b/2, y\right) \tag{1.2}$$

is the density of production points in an overlap region of two nuclei A and B where

$$T_{\mathrm{A}}\left(x, y\right) = \int \rho_{\mathrm{A,WS}}\left(x, y, z\right) \mathrm{d}z \tag{1.3}$$

is the transverse nuclear density of the nucleus A calculated as integral of the Wood–Saxon nuclear profile $\rho_{\mathrm{A,WS}}\left(x, y, z\right)$ over the collision axis z [1, 6].

1.4 Parton interaction in medium

In heavy-ion collisions, the soft particles with $p_{\mathrm{T}} \lesssim 2\ \mathrm{GeV}/c$ manifest collective hydrodynamic behaviour. For hard particles with larger p_{T}, the description by hydrodynamic models fails. The transition from collective hydrodynamic behaviour to hard scattering is reflected in a change of shape in the single particle spectra. The spectra change from a thermal exponential shape to a power law above $p_{\mathrm{T}} \gtrsim 3$–$4\ \mathrm{GeV}/c$ as predicted by perturbative QCD [1].

Hard particles with large mass or large $p_{\mathrm{T}} \gg 1\ \mathrm{GeV}/c$ are created in the early collision stages within a short time $\tau_{\mathrm{form}} \sim 0.1\ \mathrm{fm}/c$. Their production can be calculated from the nuclear structure functions in perturbative QCD due to large momentum transfers $Q^2 \gg 1\ \mathrm{GeV}^2$. Fragmentation of created hard partons produces high-p_{T} jets which can be used to probe the soft matter created by the bulk of soft particles [1].

In a central collision between two lead nuclei, the reaction region has a transverse diameter of about 12 fm, so a hard particle created near the edge and moving inward needs $12\ \mathrm{fm}/c$ before it leaves the region on the other side. During this

time, the soft matter thermalises, expands, cools down and almost decouples. All these stages get probed by the fast particle which scatters off the evolving medium and loses energy while propagating to the opposite border of the medium. The energy loss is proportional to the density of the medium and to the cross section of scattering between the probe and the medium constituents, integrated along the path of that probe [1].

High-p_{T} partons, created at the early stages of the collision, propagate through the evolving collision fireball. While interacting with the hot matter, they probe properties of this medium such as density, opacity etc. [1].

In QCD, a fast parton with $E \gg 1\,\mathrm{GeV}$ loses energy mainly by induced gluon radiation. The colour charge of the fast parton interacts with the colour charges of the medium and, as a result, emits a much softer bremsstrahlung gluon which again interacts with the colour charges in the medium. The reinteractions of the emitted gluon with the medium are characterised by a mean free path λ_{g} [1].

Energetic losses of hard partons in nuclei collisions are theoretically described for example in the BDMPS[1] model. When an initially-produced hard parton is traversing the dense matter produced in nuclei collisions, it loses energy mainly by multiple scatterings and medium-induced gluon radiation (gets quenched). In a simplified picture, subsequent multiple scatterings that the parton undergoes in the dense medium can be characterised as random events with mean free path λ, which decreases with increasing medium density. In this process, the parton radiates gluons which take away transverse momentum k_{t} with respect to the parton direction. Characteristic energy ω_{c} of the radiated gluons depends on the path length L in medium and on the properties of the medium as

$$\omega_{\mathrm{c}} = \hat{q}L^2/2, \tag{1.4}$$

where $\hat{q}$ is the transport coefficient of the medium, defined as the average transverse momentum squared transferred to the projectile per unit path length

$$\hat{q} \stackrel{\mathrm{def}}{=} \left\langle k_{\mathrm{t}}^2 \right\rangle / \lambda, \tag{1.5}$$

which is proportional to the density of the scattering centres [6].

The average energy loss $\langle \Delta E \rangle$ of the parton is proportional to the QCD coupling (Casimir) factor C_{R}, to the strong coupling constant α_{S}, to $\hat{q}$, to L^2 and is independent of the initial parton energy E [6].

This model however does not consider evolution of the medium which plays an important role in the process of a heavy-ion collision. More recent model calculations {e.g. ASW (Armesto-Salgado-Wiedemann) formalism [7], YaJEM (Yet another Jet Energy-loss Model) [7], AdS/CFT [8]} try to include these effects.

[1] R. Baier, Yu. L. Dokshitzer, A. H. Mueller, S. Peigné and D. Schiff

2 Studying jets

2.1 Jets in medium

In QCD, jet is defined as a cascade of successive emissions of partons induced by a parton created in an initial hard scattering. The partons get confined again by converting into the observable hadrons [6], where the leading hadron takes away on average about half the p_{T} of the initial hard parton [1].

In perturbative QCD, hard partons are produced in pairs emitted in angle of 180° in the system of the centre-of-mass of that pair. This leads to a pair of jets going in opposite directions [1].

If a fast parton or partons of a jet travel a too long distance through the dense matter formed in the collision, they lose so much energy in the medium that they can no longer produce hadrons with $p_{\mathrm{T}} > 2\ \mathrm{GeV}/c$. Due to massive energetic losses, inward-moving partons with $p_{\mathrm{T}} \lesssim 10\ \mathrm{GeV}/c$ do not reach the opposite edge of the medium volume and become part of the low-p_{T} background. As a result, outward-moving jets come only from a thin surface layer [1].

Jets from partons which lost too much energy are no longer recognizable as jets and become part of the hot matter of soft particles [1]. This makes jet finding a difficult task since a huge number of soft hadrons with $p_{\mathrm{T}} < 2\mathrm{GeV}/c$ contributes to the background [1].

Jets from sufficiently energetic partons probe the medium, through which they propagate, and experience modifications in energy, shape, particle composition etc. by strong interaction with constituents of the medium. This process, including total jet suppression, is called "jet quenching". Thus jets carry information about their own history and, when observed, may be used as a probing tool for investigating properties of the hot and dense strongly interacting medium created in heavy-ion collisions.

2.2 Evaluation of jet properties

First indications that a new state of matter was created in laboratory conditions emerged from Pb + Pb collisions at energy of 158 GeV per nucleon ($\sqrt{s_{\mathrm{NN}}} = 17.2$ GeV) at the SPS at CERN [1, 3, 9]. The experiments at RHIC brought convincing results from observations of jet quenching in hadrons at $\sqrt{s_{\mathrm{NN}}} = 130\,\mathrm{GeV}$ [10, 11], in two-hadron correlations at $\sqrt{s_{\mathrm{NN}}} = 200\,\mathrm{GeV}$ [12] and recently from first full reconstruction of jets [13] and from measurements of their modification [14]. At the LHC, jet quenching was experimentally observed first at the ATLAS experiment [15]. The effect of jet quenching is depicted in Figure 2.1. A pair of jets is detected in calorimeters. One jet is clear with narrow angular energy distribution whereas the energy of the jet going in opposite direction is spread across a wide range of angles. This observation indicates a jet modification by strongly interacting medium.

One of the basic tools for investigating jet properties is studying spectra of their transverse momenta (p_{T} spectra).

Since jet cross sections manifest a strong angular dependence, one of the basic kinematic variables of interest is pseudorapidity η. Pseudorapidity (of a particle,

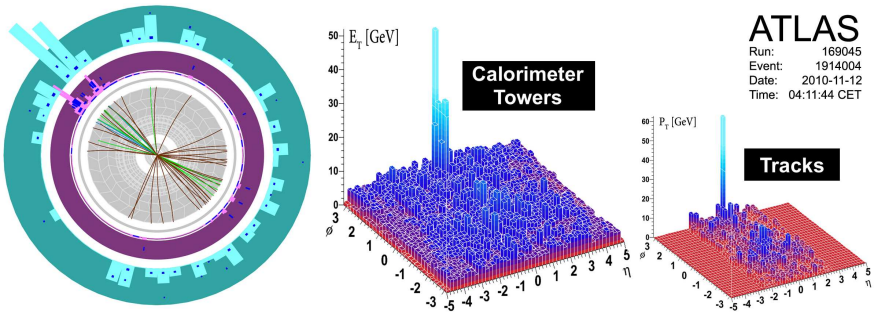

Figure 2.1: Observation of jet quenching at ATLAS [15]. A pair of detected jets with significantly different energy distributions which indicates a passage of the suppressed jet through a strongly interacting medium.

jet etc.) is defined as

$$\eta \stackrel{\text{def}}{=} -\ln\tan\left(\theta/2\right) \tag{2.1}$$

where θ is the (polar) angle between the motion direction and the beam axis (z axis).

As mentioned earlier, there is an important contribution of background in the measured p_{T} which needs to be handled properly in order to eliminate its influence.

For jets with transverse momenta $p_{\mathrm{T},i}$ and areas A_i, the background density of transverse momenta ρ is introduced as follows:

$$\rho \stackrel{\text{def}}{=} \text{median}\left\{\frac{p_{\mathrm{T},i}}{A_i}\right\}. \tag{2.2}$$

This density is used for subtraction of background contribution from raw p_{T} of reconstructed jets.

To quantify how jets (or any particles) produced in heavy-ion collisions differ from jets in $\mathrm{p}+\mathrm{p}$ collisions, the nuclear modification factor R_{AA} is introduced. This factor is defined as spectrum in heavy-ion collisions normalised to a single nucleon-nucleon collision and divided by spectrum in $\mathrm{p}+\mathrm{p}$ collisions:

$$R_{\mathrm{AA}}\left(p_{\mathrm{T}},\eta,b\right) \stackrel{\text{def}}{=} \frac{1}{\left\langle N_{\mathrm{coll}}\left(b\right)\right\rangle}\frac{\mathrm{d}^2N_{\mathrm{AA}}\left(p_{\mathrm{T}},\eta\right)/\mathrm{d}p_{\mathrm{T}}\,\mathrm{d}\eta}{\mathrm{d}^2N_{\mathrm{pp}}\left(p_{\mathrm{T}},\eta\right)/\mathrm{d}p_{\mathrm{T}}\,\mathrm{d}\eta}. \tag{2.3}$$

If the medium created in heavy-ion collisions did not modify properties of observed jets, it would mean that nuclei collisions are equivalent to a superposition of independent nucleon collisions and R_{AA} would be equal to 1 by construction.

Figure 2.2 shows results of measurements of R_{AA} of hadrons in various experiments at SPS, RHIC and LHC. Figure 2.3 shows values of R_{AA} of jets measured with the STAR experiment at RHIC.

Another tool for estimating the influence of medium on jets is the ratio R_{CP} of jet p_{T} spectrum in the central collisions to the spectrum in the most peripheral collisions

$$R_{\mathrm{CP}}\left(p_{\mathrm{T}},\eta,b_{\mathrm{C}},b_{\mathrm{P}}\right) \stackrel{\text{def}}{=} \frac{\left\langle N_{\mathrm{coll}}\left(b_{\mathrm{P}}\right)\right\rangle}{\left\langle N_{\mathrm{coll}}\left(b_{\mathrm{C}}\right)\right\rangle}\frac{\mathrm{d}^2N\left(p_{\mathrm{T}},\eta,b_{\mathrm{C}}\right)/\mathrm{d}p_{\mathrm{T}}\,\mathrm{d}\eta}{\mathrm{d}^2N\left(p_{\mathrm{T}},\eta,b_{\mathrm{P}}\right)/\mathrm{d}p_{\mathrm{T}}\,\mathrm{d}\eta} \tag{2.4}$$

where indices C, P indicate the central and the most peripheral collisions respectively. In analogy with R_{AA}, if the medium created in central collisions did not

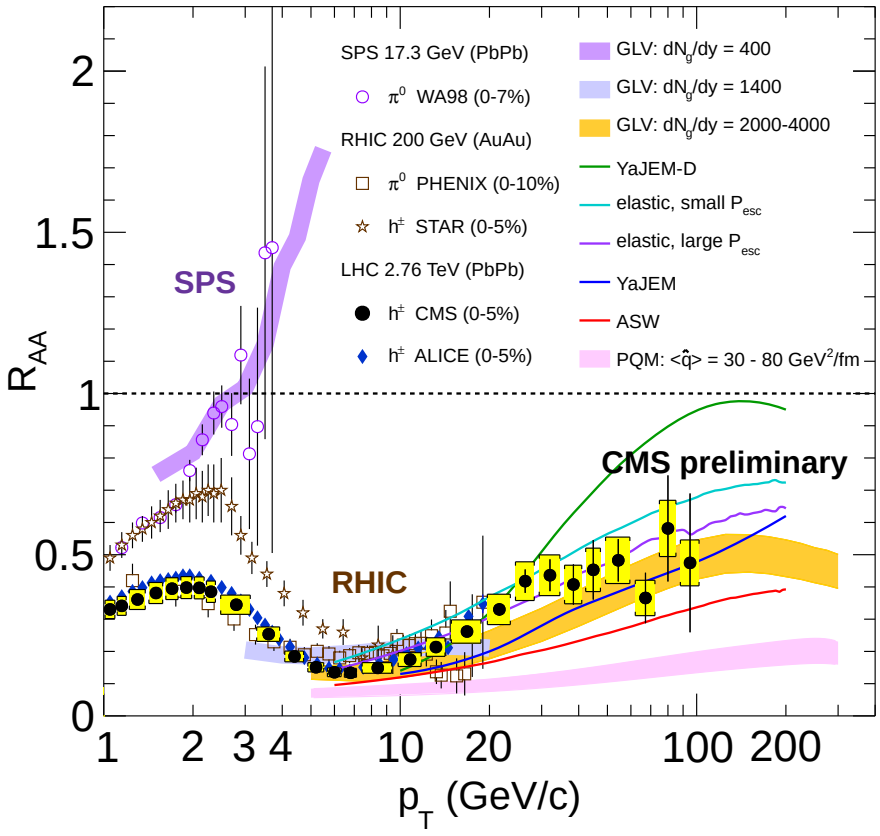

Figure 2.2: R_{AA} of hadrons in experiments at SPS, RHIC and LHC [16].

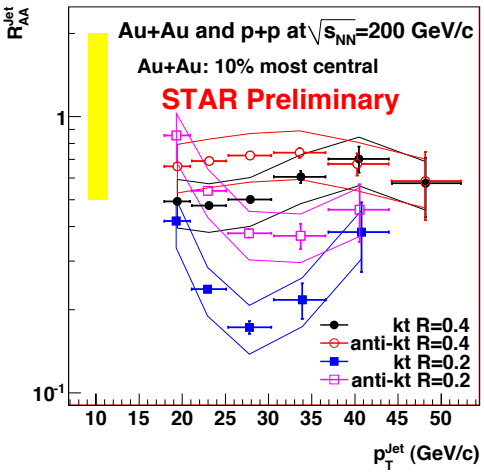

Figure 2.3: R_{AA} of jets in the STAR experiment at RHIC [14].

affect properties of observed jets, spectra of jets in central collisions would not differ from spectra in peripheral collisions and R_{CP} would be equal to 1. Since measuring R_{CP} does not require any reference measurements from proton collisions, it provides much smaller systematic errors compared to measuring R_{AA}.

Since the conditions created in heavy-ion collisions depend strongly on the impact parameter of colliding nuclei, all the jet variables must be studied as functions of centrality.

2.3 Jet algorithms

2.3.1 General concept

A jet algorithm is a process which is supposed to take a list of calorimeter towers, detected hadrons or (simulated) partons and associate these into jets so that kinematic properties of the jets may be associated to the corresponding properties of the energetic partons in the hadronic final state produced in the hard scattering process [17].

Jet algorithm selects a set of particles, which are typically emitted close to each other in angle, and marks them to belong to a common jet. In the 4-momentum formalism, all particles are considered to be massless. In a process called "recombination scheme", momenta of particles in a jet are combined to form the momentum of the jet [17].

The key parameter of a jet algorithm is a radius R defined as distance in $\eta \times \phi$ space. Its meaning depends on the algorithm.

The ideal jet algorithm should meet the following criteria [17]:

1. Full specification: The jet selection algorithm, the jet kinematic variables and the corrections should be clearly and completely defined, including definitions of preclustering, merging and splitting algorithms, if necessary.

2. Theoretically good behaviour: The algorithm should be infrared and collinear safe with no ad hoc clustering parameters.

    - Infrared safety: Jet finding procedure should be insensitive to the presence of soft radiation between jets.
    - Collinear safety: Jet finding procedure should be insensitive to the splitting of jet transverse energy into multiple collinear particles.
    - Invariance under boosts: The algorithm should find the same jets independent of boosts in the direction of collision axis.

3. Detector independence: The jet algorithm should be independent of cell type, numbers, detector segmentation or size.

4. Order independence: The algorithms should find the same jets at the parton, particle and detector level.

2.3.2 Cone algorithms

In a cone jet algorithm, all particles reconstructed trajectories of which lie inside a cone of radius R are grouped together and considered to constitute a protojet. The cone axis is corrected, replaced by the updated centroid — a new axis calculated as a weighted average of directions of tracks inside the cone. The weight of a direction is taken to be the transverse energy $E_{\mathrm{T}} = E \sin\theta$ of the track. These corrections are repeated iteratively until a stable cone axis is found [17].

The searching for cone axes usually starts from the most energetic particles, the so called "seeds", which pass a certain energy threshold [17].

Because the final stable cones may overlap, a procedure how to split or merge overlapping cones must be specified. The concept of cone algorithms with seeds (such as Snowmass and UA1) brings also other difficulties such as infrared and collinear sensitivity [17]. To eliminate these drawbacks, the Seedless Infrared-Safe Cone jet algorithm (SISCone) has been developed [18].

2.3.3 Sequential recombination algorithms

Sequential recombination (or clustering) jet finders have simple definitions and are all infrared safe [19].

A sequential recombination jet finder is defined according to the following general scheme [20].

1. $\forall\, i, j$: calculate distance d_{ij} between particles i and j and distance $d_{i\mathrm{B}}$ between particle i and the beam (B):

$$d_{ij} = \min\left(k_{\mathrm{T},i}^{2p}, k_{\mathrm{T},j}^{2p}\right) \frac{\Delta_{ij}^2}{R^2}, \quad \Delta_{ij}^2 = (y_i - y_j)^2 + (\phi_i - \phi_j)^2\,, \tag{2.5}$$

$$d_{i\mathrm{B}} = k_{\mathrm{T},i}^{2p}, \tag{2.6}$$

   where $k_{\mathrm{T},i}$, y_i, and ϕ_i are respectively the transverse momentum, rapidity and azimuth of particle i.

2. Find $d_{\min}$:

$$d_{\min} = \min\left(d_{ij}, d_{i\mathrm{B}}\right). \tag{2.7}$$

   - If $\exists\, i, j : d_{\min} = d_{ij}$, merge particles i and j into a single particle and combine their momenta.
   - If $\exists i : d_{\min} = d_{i\mathrm{B}}$, declare particle i to be a final jet and remove it from the list.

These steps are repeated until no particles are left.

Specific algorithms differ in the power of the transverse momentum taken in the distance calculation (2.5). This general scheme allows to include all three mentioned algorithms by introducing the parameter p.

$$p = \begin{cases} 1 & k_{\mathrm{t}} \\ 0 & \text{Cambridge/Aachen} \\ -1 & \text{anti-}k_{\mathrm{t}} \end{cases} \tag{2.8}$$

The characteristic property of the anti-k_t algorithm is that distances between hard and soft particles are smaller than between similarly separated soft particles. Therefore soft particles cluster with hard ones long before they cluster among themselves. Hard particles accumulate soft particles within a circle of radius R, resulting in a perfectly conical jet. In case of two hard particles close to each other, corresponding jets are separated by a line of shape depending on transverse momenta of the hard particles. Boundaries of final jets are determined by the directions of hard particles whereas soft particles do not modify them [20].

Fig. 2.4 illustrates behaviour of different jet algorithms in a generated event of partons. Coloured areas correspond to the "active" catchment areas of jets, i.e. the regions within which the random soft "ghost" particles are clustered into that jet. In case of the anti-k_t algorithm, the hard jets are all circular with a radius R, and only the softer jets have more complex shapes. For other algorithms, areas and borders of jets depend on the distribution of random soft particles.

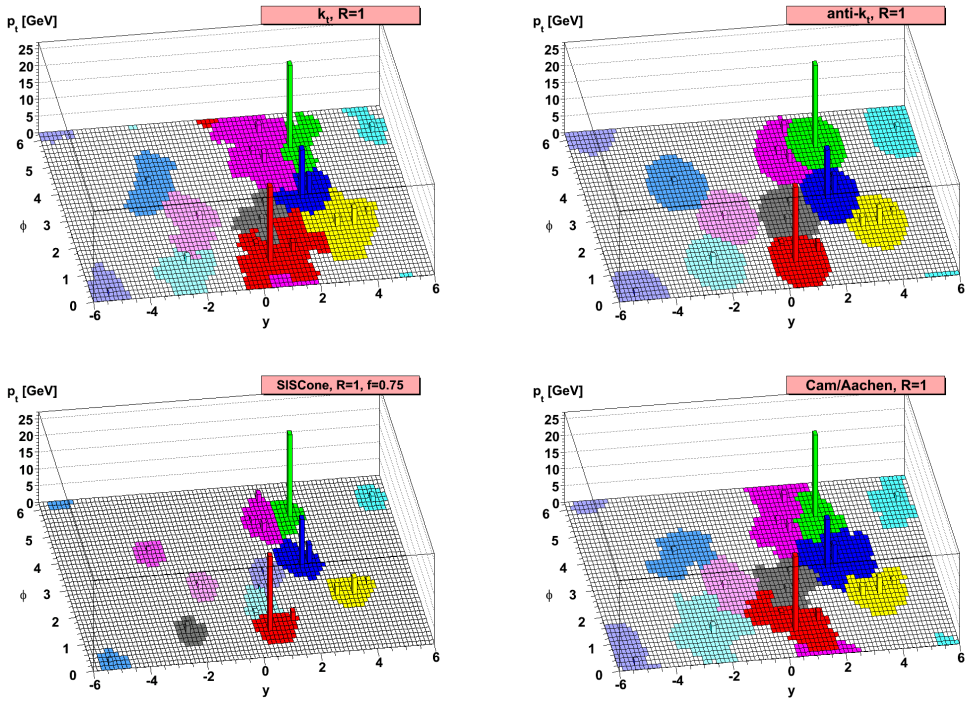

Figure 2.4: Active catchment areas of jets for different algorithms [20].

3 The ALICE experiment

ALICE (A Large Ion Collider Experiment) is a general-purpose heavy-ion experiment designed to study the physics of strongly interacting matter and the quark-gluon plasma in collisions of lead nuclei at the Large Hadron Collider (LHC) at CERN [6]. The ALICE collaboration groups over 1000 specialists from 30 countries involved in construction and operating of the experiment [21].

ALICE is one of the four main experiments installed at the LHC, running since 2009. The Large Hadron Collider is a particle accelerator, built at CERN inside a ring tunnel of nearly 27 km in circumference. It has been designed to accelerate protons and lead nuclei to maximum energies of 7 TeV and 2.76 TeV/nucleon respectively. Two beams orbiting in opposite directions may cross in four interaction points where the detectors are installed [22].

Both collisions of protons and collisions of lead nuclei are measured with the ALICE detectors. Compared to other experiments at the LHC, ALICE features unique capability of tracking and identification of detected particles.

3.1 Apparatus

ALICE detectors have been designed to allow tracking and identification of particles from wide range of p_{T} from $\sim 100\,\mathrm{MeV}/c$ up to $\sim 100\,\mathrm{GeV}/c$ and reconstruction of short-lived particles such as hyperons, D mesons and B mesons. Detectors of the apparatus have to be able to cope with large particle multiplicities, up to 8000 charged particles per rapidity unit at mid-rapidity [23].

The apparatus consists of a central part, which measures hadrons, electrons and photons in full range of azimuth angle ϕ, and of a forward spectrometer to measure muons (see the ALICE apparatus layout in Fig. 3.1).

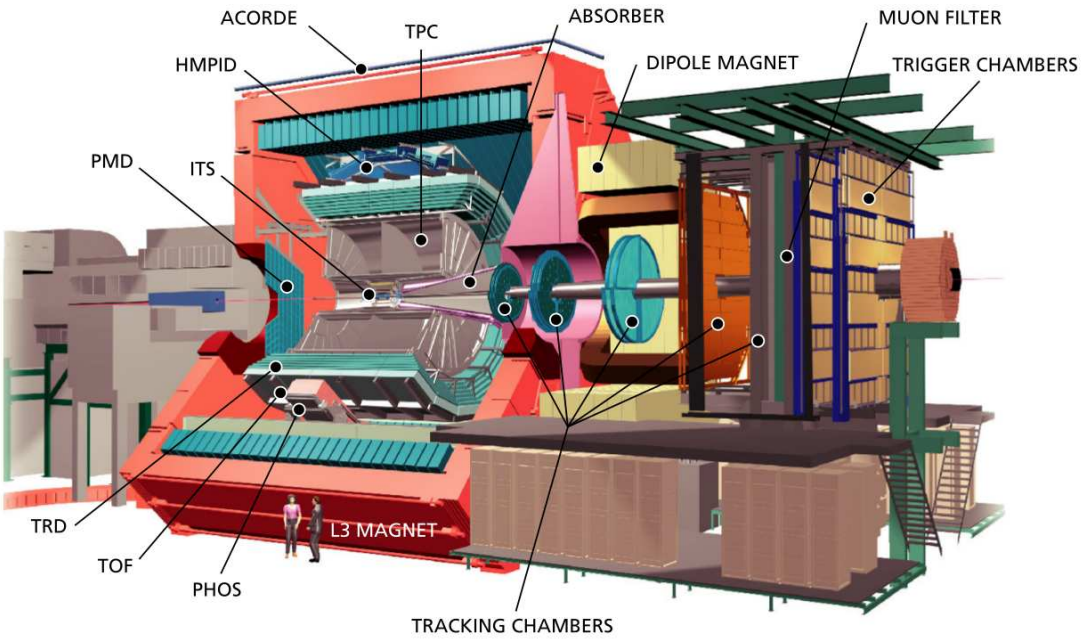

Figure 3.1: Layout of the ALICE apparatus [23].

A moderate magnetic field of induction of 0.5 T is provided by a large solenoidal magnet surrounding the central part of the apparatus [23].

Tracking is provided by the detectors of the central barrel covering a pseudorapidity range of $|\eta| \leq 0.9$. This system includes an Inner Tracking System (ITS), a Time-Projection Chamber (TPC) and a Transition-Radiation Detector (TRD) [23].

3.1.1 The Inner Tracking System

The Inner Tracking System (ITS) consists of six cylindrical layers of silicon detectors. Pixel, drift and strip silicon detectors are located in pairs of layers at radii (distance from the apparatus axis) $r = 3.9, 7.6, 15.0, 23.9, 38.4$ and 43.4 cm [23]. Arrangement of layers of the ITS detectors is presented in the layout in Fig. 3.2.

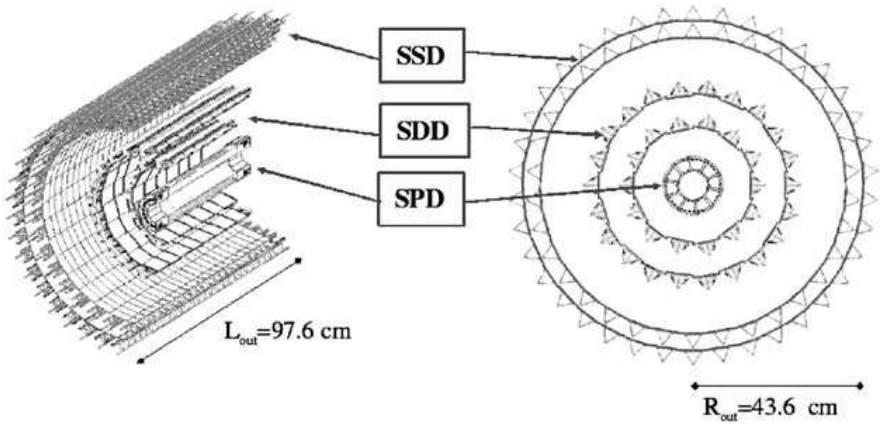

Figure 3.2: Layout of the ITS [23].

The functions of the ITS are:

- to localise the place of collision (primary vertex) with a resolution better than 100 μm,
- to reconstruct the secondary vertices from decays of hyperons, D mesons and B mesons,
- to track and identify particles with momenta below 100 MeV/c,
- to improve the momentum and angle resolution for the high-p_{T} particles traversing the TPC,
- to reconstruct (with limited momentum resolution) particles traversing dead regions of the TPC [23].

The Silicon Pixel Detectors

The two innermost layers of the ITS are formed by the Silicon Pixel Detectors (SPD). They serve for the determination of the position of the primary vertex and for measurement of the impact parameter of secondary tracks from the weak decays of strange, charm, and beauty particles. They must be able to operate in conditions where the track density could reach 80 cm^{-2}.

The SPD provide an average spatial resolution of 12 μm in the (r, ϕ) plane and 100 μm in the z direction (along the beam pipe axis) [23].

The Silicon Drift Detectors

The Silicon Drift Detectors (SDD) occupy the two intermediate layers of the ITS. Besides tracking capabilities they provide also energy loss ($\mathrm{d}E/\mathrm{d}x$) measurement needed for the particle identification in the ITS. Each module has its sensitive area split by the central cathode strip into two drift regions. A nominal voltage of -2.4 kV is applied to the cathode. Each drift region has 256 collection anodes with 294 μm pitch and three rows of 33 point-like ($20 \times 100\ \mu\mathrm{m}^2$) MOS[1] charge injectors. The injectors provide monitoring of the drift speed v and calibration of measurements. The drift speed depends on temperature as $v \propto T^{-2.4}$. The nominal value of the drift speed is $8.1\ \mu\mathrm{m} \cdot \mathrm{ns}^{-1}$.

Modules of the SDD provide an average spatial resolution of 35 μm in the (r, ϕ) plane and 25 μm in the z direction [23].

The Silicon Strip Detectors

The outer layers of the ITS are equipped with the Silicon Strip Detectors (SSD). The importance of the SSD is in the connection of tracks from the TPC to the ITS. They also provide $\mathrm{d}E/\mathrm{d}x$ measurement to help identify low-momentum particles. The SSD sensors are double-sided strip detectors, where the active area of each is $73 \times 40\ \mathrm{mm}^2$.

The spatial resolution of the SSD is 20 μm in the (r, ϕ) plane and 830 μm in the z direction [23].

3.1.2 The Time-Projection Chamber

The Time-Projection Chamber (TPC) is the main tracking detector of the ALICE central barrel. This device enables to measure charged-particle momenta, to identify particles and helps determine the vertex position. The measurement of tracks in the TPC covers the range in pseudorapidity of $|\eta| \leq 0.9$ (up to $|\eta| \approx 1.5$ for tracks with reduced length and momentum resolution) and in p_{T} up to $100\ \mathrm{GeV}/c$ [23].

The TPC is the main detector for the study of hadrons in the collisions at the LHC. Measuring properties of hard probes such as high-p_{T} jets requires very good momentum resolution up to high values. Momentum resolution of about 1 % is needed for momenta close to $100\ \mathrm{MeV}/c$. Using the TPC in combination with the other tracking detectors (i.e. the ITS and the TRD) allows to achieve momentum resolution of about 10 % for tracks with p_{T} of $100\ \mathrm{GeV}/c$ [23].

A schematic layout of the TPC is in Fig. 3.3. The device is made of a cylindrical field cage and has an inner radius of about 85 cm, an outer radius of about 250 cm and a total length of 500 cm. The detector cage is filled with $88\ \mathrm{m}^3$ of a gas mixture consisting of Ne (90 %) and CO_2 (10 %). The primary electrons are transported over a distance of up to 2.5 m on either side of the central electrode to the end-plates. Each end-plate is divided into into 18 trapezoidal sectors where the multi-wire proportional chambers with cathode pad readout are mounted [23].

[1] Metal-Oxide Semiconductor

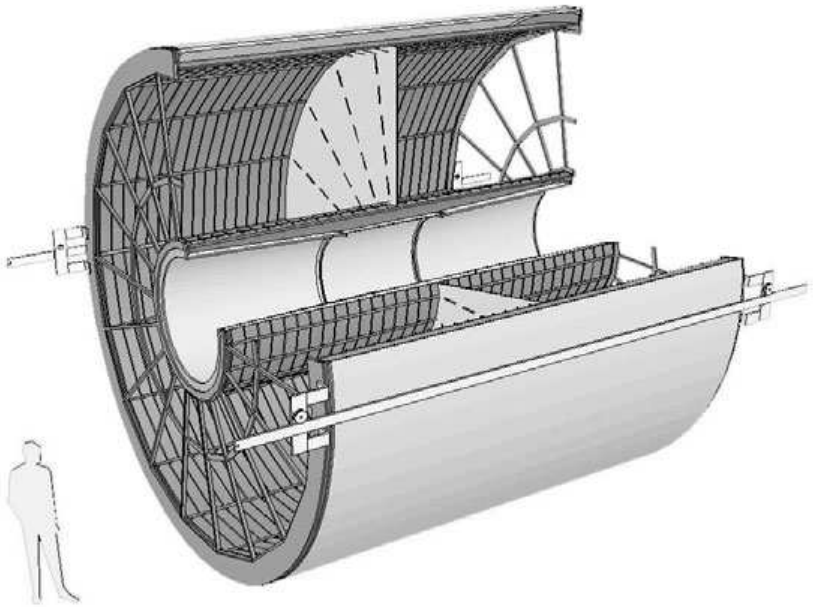

Figure 3.3: Layout of the TPC [23].

3.1.3 The Transition-Radiation Detector

The role of the Transition-Radiation Detector (TRD) is to identify electrons in the central barrel with momenta greater than $1\,\mathrm{GeV}/c$. The TRD consists of six individual layers which cover the same range in pseudorapidity as the TPC. Arrangement of 18 sectors matches the azimuthal segmentation of the TPC. A module of the TRD includes a radiator and a multi-wire proportional readout chamber [23].

3.1.4 The Time-Of-Flight detector

The Time-Of-Flight (TOF) detector is included for particle identification (PID) in the intermediate momentum range (0.2–2.5 GeV/c) and in polar angle range $|\theta - 90°| < 45°$, i.e. in roughly the same range in pseudorapidity as the TPC. The TOF identifies pions, kaons and protons and contributes to the track and vertex reconstruction and to $\mathrm{d}E/\mathrm{d}x$ measurements in the range of low momenta. The modules are arranged in a scheme similar to that of the TRD. Modules consist of Multi-gap Resistive-Plate Chamber (MRPC) strips subdivided into pads [23].

3.1.5 V0 detector

V0 detector is a pair of arrays (V0A and V0C), located asymmetrically on each side of the interaction point at 340 cm and 90 cm from the vertex [23], which cover the full azimuth within $2.8 < \eta < 5.1$ and $-3.7 < \eta < -1.7$ respectively [2]. It provides a minimum bias trigger for the central barrel detectors, centrality trigger, centrality indicator and other signals. Each array of the detector consists of 32 elementary scintillator counters arranged in four rings [23].

3.1.6 Other detectors

Other detectors contribute to the measurements at ALICE such as the High-Momentum Particle Identification Detector (HMPID) consisting of Ring Imaging Cherenkov counters (RICH) to measure high-p_{T} hadrons ($p_{\mathrm{T}} > 1$ GeV/c), the Photon Spectrometer (PHOS) which is a high-resolution electromagnetic spectrometer to detect electromagnetic particles, the Forward muon spectrometer to detect decays of heavy quark vector mesons into muon pairs, the Zero-Degree Calorimeter (ZDC), placed at 116 m from the Interaction Point, to detect non-interacting (spectator) nucleons, the Photon Multiplicity Detector (PMD), the Forward Multiplicity Detector (FMD), the T0 detector, the Cosmic-ray trigger detector and the recently installed Electromagnetic Calorimeter (EMCal) which enables full reconstruction of energetic jets and improves measurement of photons and electrons with high momenta [23, 24].

3.2 Track reconstruction

Track reconstruction is one of the most complex measurements in the ALICE experiment. The track reconstruction requires precise determination of the particle momenta as close as possible to the point of their origin. Also a good track-finding efficiency and a reconstruction precision for tracks down to $p_{\mathrm{T}} = 100$ MeV/c are required as well and the tracks need to be extrapolated to the outer detectors which provide the particle identification. The primary-vertex position is reconstructed in ALICE with track measurement by the SPD [6].

The Kalman filtering is used for track determination. It is the most advanced local track-finding method which takes into account additional effects, such as multiple scattering, energy loss or non-homogeneous magnetic field, which are difficult to handle using global fit [6, 25].

The tracking procedure starts from the the outer radius of the TPC, where the track density is minimal. First, searching for track candidates is performed. The tracking proceeds towards the smaller TPC radii and the track parameters are getting more refined by associating new clusters using the Kalman filter. When all of the track candidates are extrapolated to the inner limit of the TPC, the tracking continues in the ITS. The ITS tracking process tries to prolong the tracks found in the TPC as close as possible to the primary vertex while assigning additional ITS clusters to the tracks. After the tracking process attributes to all the track candidates from the TPC their clusters in the ITS, a special ITS stand-alone tracking procedure tries to recover more tracks from the rest of the ITS clusters [6].

When the tracking reaches the primary vertex, the procedure discards all previous information except the track angles. Then the tracking is restarted from the primary vertex back to the outer layer of the ITS. When the outer wall of the ITS is reached, the χ^2 is calculated between the fit and the hits in the ITS. If the χ^2 is good and the track has at least 3 hits in the ITS, then the track gets the ITS refit assigned. The tracking continues propagating outwards through the TPC. At the outer radius of the TPC, the tracks have sufficiently precisely estimated parameters, so that they can be extrapolated to the outer detectors (TRD, TOF, HMPID, PHOS), where they obtain the PID information if available [26, 6].

Finally, another fit with the Kalman filter is applied on all the tracks backwards to the primary vertex. The reconstructed tracks (together with the PID information) are then stored in the Event Summary Data (ESD) [6].

3.3 Centrality determination

In the calculation in the Glauber model, the nuclear density for ^{208}Pb is modelled by the Woods–Saxon distribution for a spherical nucleus with a radius of 6.62 fm and a skin depth of 0.546 fm [2]. Calculated parameters of a collision geometry are presented in Table 3.1 as functions of centrality ranges.

Table 3.1: Geometrical parameters of heavy-ion collisions [27].

Centrality [%]	b_{min} [fm]	b_{max} [fm]	N_{part}	Sys. err.	N_{coll}	Sys. err.
0–10	0.00	4.95	356.5	3.6	1502.7	169.9
10–20	4.95	6.98	260.5	4.4	923.26	99.6
20–30	6.98	8.55	186.4	3.9	558.68	56.4
30–40	8.55	9.88	128.9	3.3	321.20	31.0
40–50	9.88	11.04	85.0	2.6	171.67	15.2
50–60	11.04	12.09	52.8	2.0	85.13	8.0
60–70	12.09	13.06	30.0	1.3	38.51	3.8
70–80	13.06	13.97	15.8	0.6	15.78	1.3
80–90	13.97	14.96	7.52	0.4	6.32	0.5
90–100	14.96	19.61	3.77	0.1	2.63	0.10

The correspondence between centrality and detector response in ALICE is obtained from a fit of the model to the measured V0 amplitude distribution, as shown in Fig. 3.4.

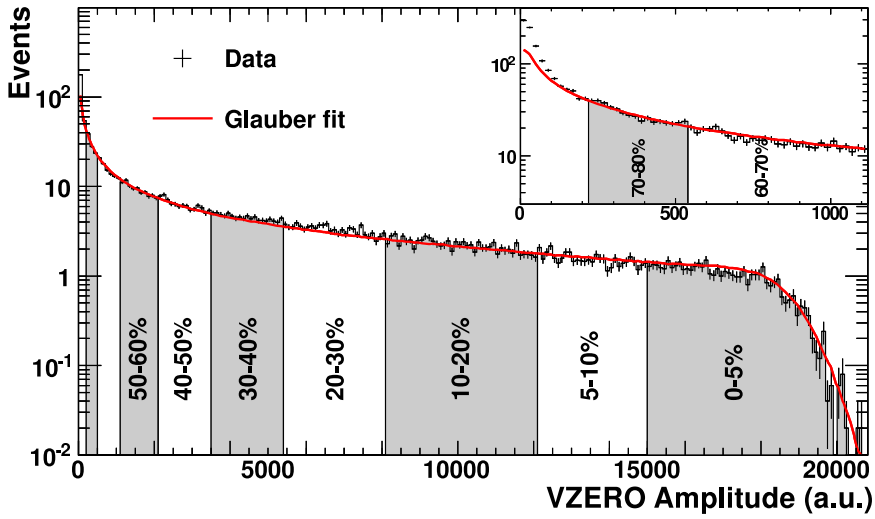

Figure 3.4: Centrality–signal correspondence used for the centrality measurement with the V0 detector [2].

4 Monitoring SDD

4.1 Silicon Drift Detectors

The Silicon Drift Detectors (SDD) represent the intermediate component of the ITS, consisting of two layers (Layer 3 and Layer 4) at average radii 15.03 cm and 23.91 cm from the detector axis respectively.

The SDD have 260 detectors (modules) in total $(84 + 176)$. The sensitive area of each module is divided into two drift regions — half-modules. There are 256 anodes in each half-module to collect the signal and 99 charge injectors to enable calibration of the drift speed, as shown in Fig 4.1.

The ITS is operated at room temperature. The drift speed values are in range 5.6–8.1 μm/ns and depend on temperature as $v \propto T^{-2.4}$. That means a variation of 0.8 %/K in these conditions [28].

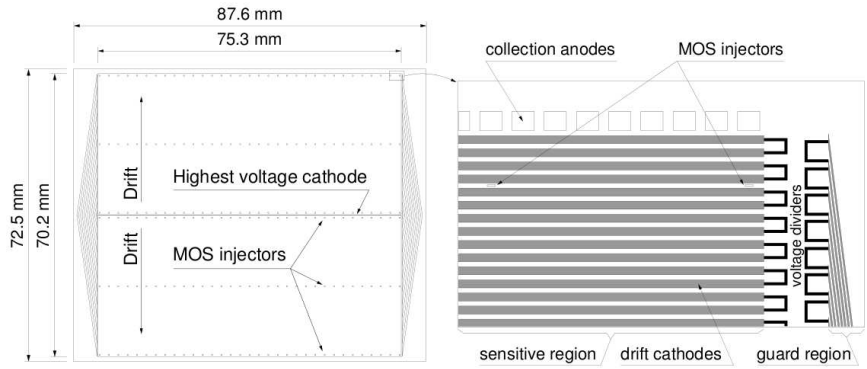

Figure 4.1: Layout of the SDD module [28].

4.2 Undergraduate project

During my stay at CERN in August 2011, I was given an opportunity to get involved in monitoring the ALICE Silicon Drift Detectors.

I collaborated with members of the SDD group for three weeks and within a mini-project I investigated drift-speed calibration data and studied reports in the ALICE e-logbook (database of technical logs from the LHC runs) to acquaint myself with the detector monitoring in ALICE. The results of the project were presented and discussed in two SDD group meetings[1] where additional objectives and detailed studies were suggested.

In total, following objectives were proposed:

- find unusual variations of the drift speed in the SDD modules for year 2011 and possible causes of the variations,
- find a time correlation between injector efficiency and humidity inside the ITS, namely get more details on humidity influence on the fraction of good

[1] `https://indico.cern.ch/conferenceDisplay.py?confId=124995`
`https://indico.cern.ch/conferenceDisplay.py?confId=124996`

modules, possibly related to the reported decrease of injectors efficiency caused by a loss of injectors on the Layer 4 in the middle of March,

- study the behaviour of the dependence of the drift speed on the anode number across modules and specify source of abnormalities.

Tools which I used to meet these objectives are listed bellow.

- Data at `/alice/data/2011/OCDB/ITS/Calib/DriftSpeedSDD/` [29]
- ROOT v5-28-00f [30]
- AliRoot v4-21-32-AN [25]
- AliRoot macros
  - `$ALICE_ROOT/ITS/macrosSDD/PlotDriftSpeedSDDVsTime.C`
  - `$ALICE_ROOT/ITS/macrosSDD/ShowDriftSpeedSDD.C`
- ALICE e-logbook at `https://alice-logbook.cern.ch/logbook/`

4.2.1 Drift speed

I studied how the measured drift speed changed in time. For this purpose, I used the macro `PlotDriftSpeedSDDVsTime.C`. The steps executed by this code are listed bellow.

For chosen data:

- get the object with array of drift speed objects
- for each half-module
  - load drift speed array
  - get time, injector status, drift speed value (v [μm/ns])
  - calculate charge mobility as $\sigma = v$ [cm/s]$/E$ where electrical drift field $E = (1800 - 45)/(291 \cdot 0.012)$
  - calculate temperature as T [K] $= 293.15 \cdot (\sigma/1350)^{-1/2.4}$
- count half-modules with good injector status ("good half-modules") for each layer
- calculate fraction of good half-modules (injector efficiency), average drift speed (total, Layer 3, Layer 4)

The macro then plots drift speed and fraction of good half-modules for chosen modules (4, 37, 87, 213) as functions of run number and time.

In order to study the calibration data in a detailed scope, I divided the available time scale into shorter periods. First, I studied the variations month by month.

The results are shown in Fig. 4.2. Since files for Jan and Aug contained no valid data, I focused on the range February–July only.

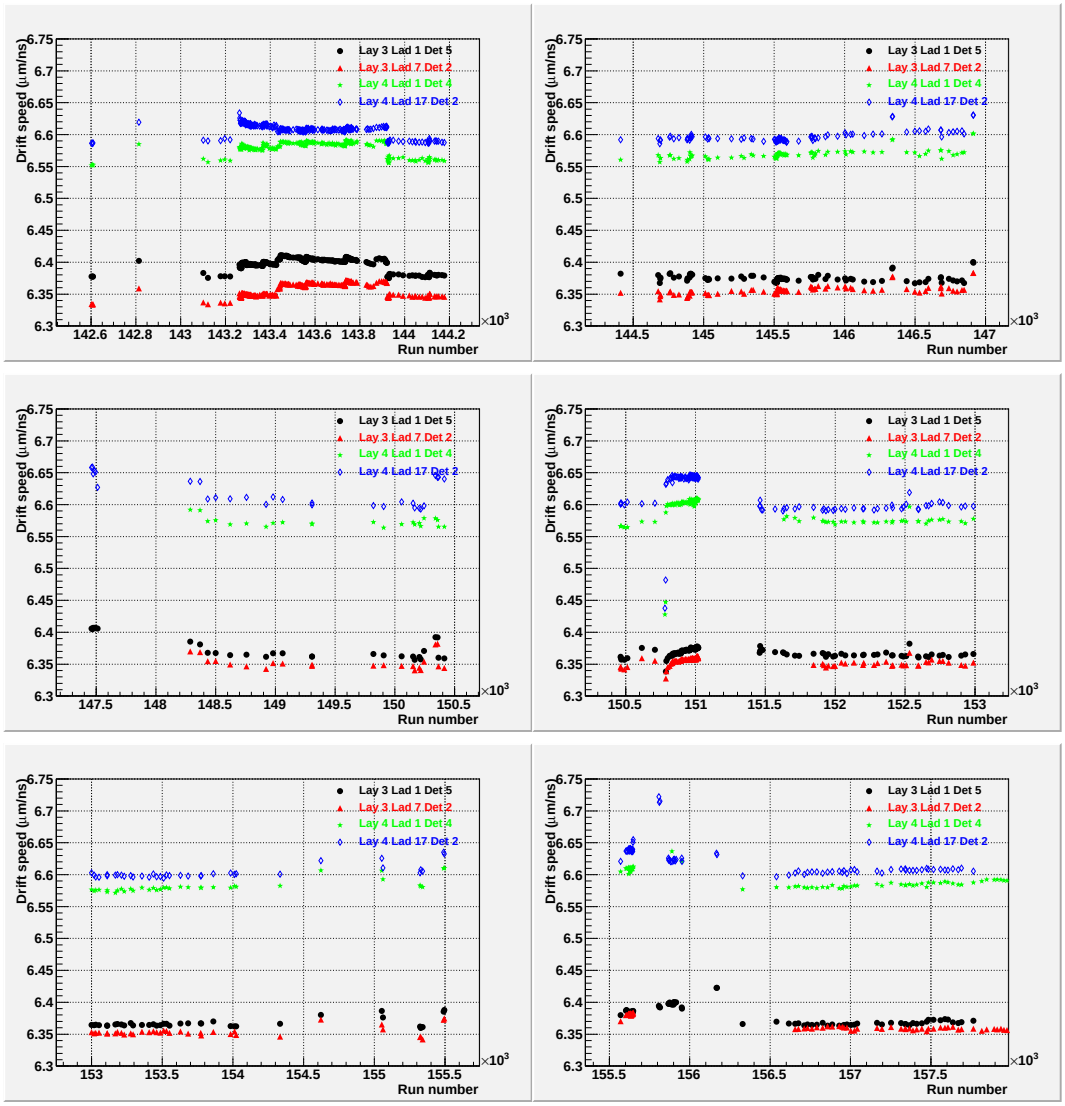

Figure 4.2: The drift speed for runs in different months (February–July).

I identified variations of the drift speed (from the plots for drift speed vs run number) and I roughly estimated ranges of runs where the speed changed more than cca 4 per mil. I studies variations for these chosen intervals in detail and created a list of the individual numbers of the suspicious runs.

I selected from the list only runs manifesting an abrupt rise of the drift speed preceded and followed by series of runs having normal values of the drift speed. The selected runs are listed in Table 4.1.

Table 4.1: Selected runs manifesting skips in drift speed.

Month	First run	Selected runs
February	140411	143263–143921
March	144358	146339–146342, 146913–146914
April	147346	150341–150357
May	150434	152531
June	152992	none
July	155502	none

I also recorded the numbers of the last previous normal run and of the first next normal run for each abnormal run or a series of them in order to restrict the time period during which the event causing the rise of the drift speed might had happened.

Figure 4.3 shows an unusual step-like periodic structure of drift speed variation found for February. The temperature variation for this period is shown in Fig. 4.4. Comparing both figures allows to demonstrate how the variation of temperature affects the drift speed (see the formula in the macro description above).

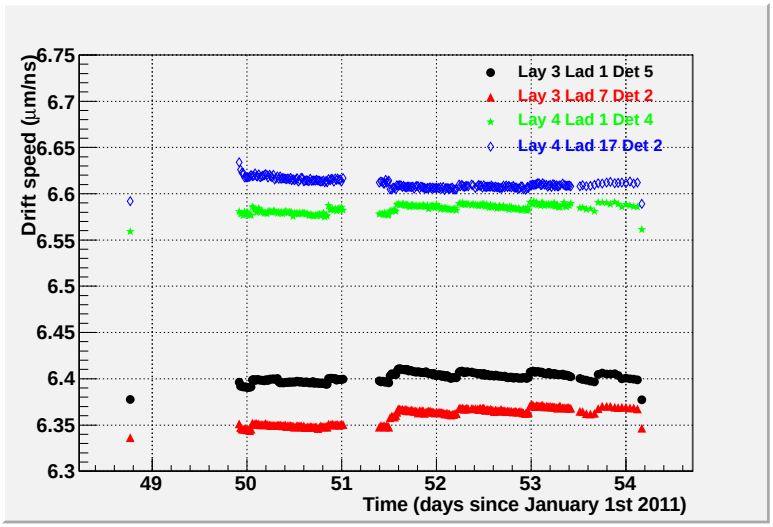

Figure 4.3: Periodic structure of drift speed variation for runs 143221–143923.

I studied the log entries within the time periods between peripheral normal runs, extended by a few hours after the first normal run. I looked for potentially related entries (containing such keywords as SDD, ITS, inject, cool, ventil, temper, humid) and chose those referring to errors, problems, unexpected behaviour or ventilation in the ITS and some reports on the injector tests. The log entries found

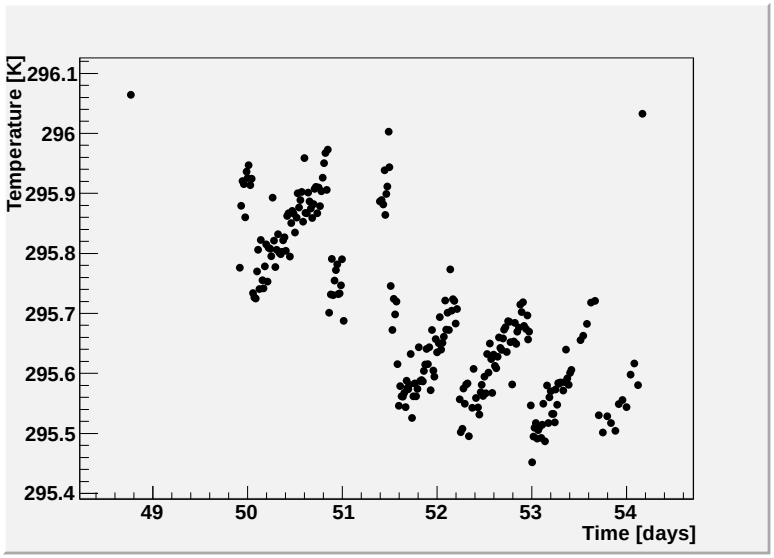

Figure 4.4: Temperature variation corresponding to the runs 143221–143923.

for the selected runs were listed in a table with indicated times of the peripheral normal runs.

4.2.2 Injector efficiency and humidity

I searched for the runs with low fraction of good half-modules (bellow 0.7) and I followed a procedure similar to the case of drift speed. I also studied the relation between injector efficiency and humidity. The plots are in Figures 4.5, 4.6, 4.7 where the lower rows show humidity values for corresponding periods. The plot with data from July shows a clear drop of injector efficiency at day 208 which corresponds to the loss of injectors in July 28 due to a damage caused by the beam loss.

Since values of humidity inside the SDD were not available for the studied period, I had to use humidity data measured by the SSD sensors [31] which consisted of two sets, for sensors installed at side A and at side C.

I studied time dependence of humidity for each month and searched for corresponding periods of abnormal humidity and low fraction of good modules by comparing plots in associated pairs.

I found an obvious correlation between high values of humidity and decrease of the injector efficiency. There is also a significant difference in the behaviour of the humidity time dependence for the side A and the side C and there are a few points with negative values of humidity. Data are shown and compared to the values of injector efficiency in Figures 4.5, 4.6, 4.7. Humidity for the side A is plotted in blue, for the side C in red.

Then I tried to verify this correlation and to discover reasons for this behaviour by searching for related problems (i.e. problems of ITS ventilation system) in the e-logbook.

I learned[2] that most of the correlations between high humidity and low fraction of good half-modules were related to ventilation system shutdowns and reflected

[2]from private communication in the SDD meetings

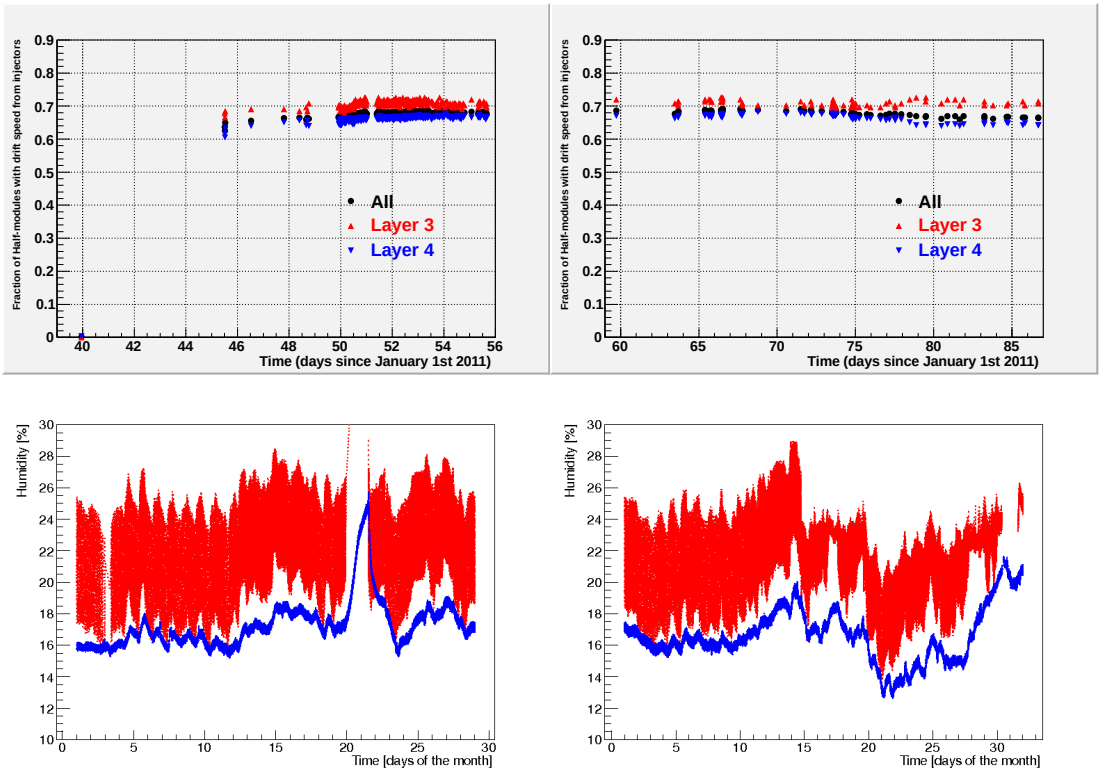

Figure 4.5: Fraction of good modules and humidity values for months February–March.

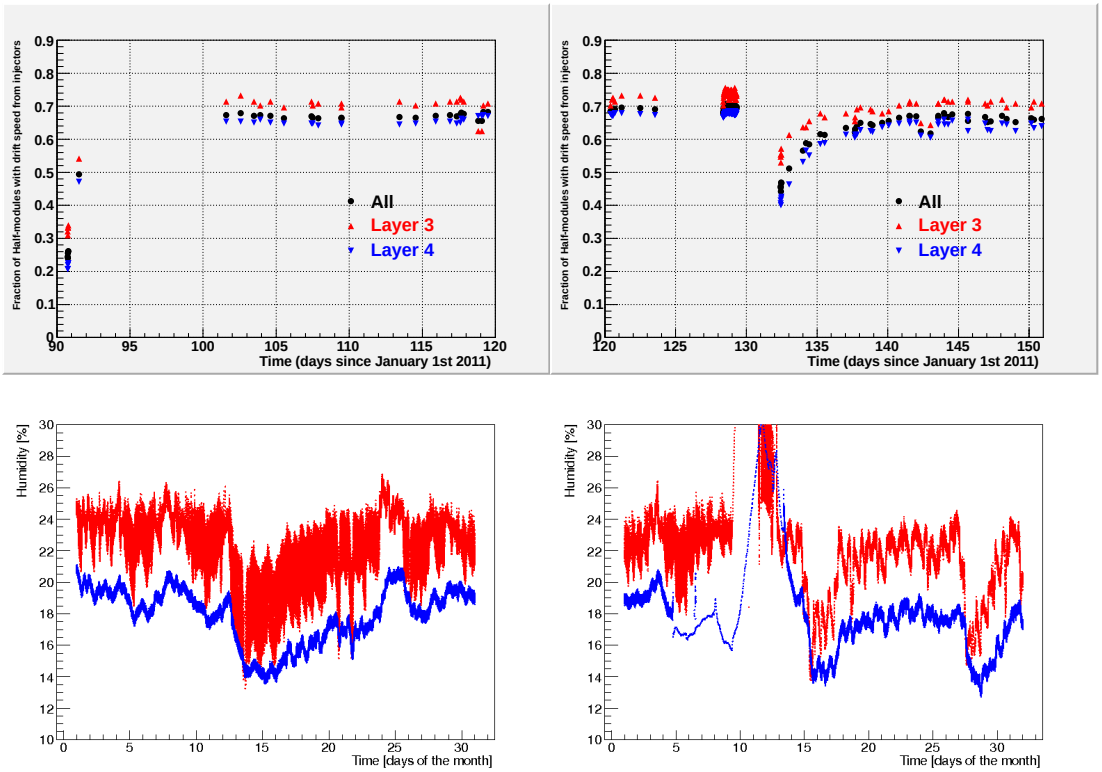

Figure 4.6: Fraction of good modules and humidity values for months April–May.

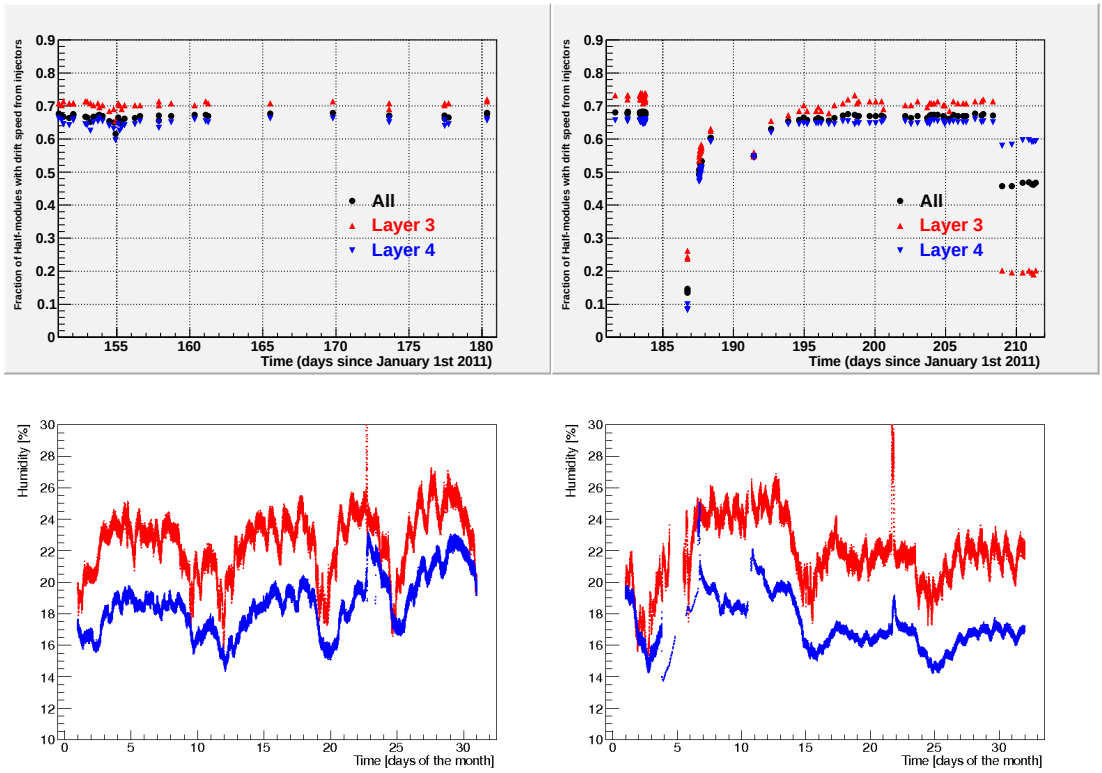

Figure 4.7: Fraction of good modules and humidity values for months June–July.

powering up detectors and switching up ventilation machines in the ITS which were starting decreasing humidity inside detectors at that moment.

The difference between humidity data from sides A and C might be explained by oscillations of the ventilation activity.

Despite detailed investigation I did not find any reports that might be assigned to the progressive injector efficiency decrease observed to have started in the middle of March. Only lower values of humidity may be observed for this period.

4.2.3 Drift speed dependence on anode number

To study how drift speed in calibration data depends on anode in modules, I used the macro `ShowDriftSpeedSDD.C`. This piece of code processes the calibration data in a similar way compared to `PlotDriftSpeedSDDVsTime.C`. It draws graphs showing drift speed and temperature as functions of module number (240–499) and also graphs showing drift speed dependence on anode number within each module.

After spotting a few non-standard behaving modules, I modified the macro and studied the data module by module. When looking at the dependence of the drift speed on the anode number for individual half-modules, some interesting irregularities may be found. A few examples are shown in Fig. 4.8.

I sorted the abnormal curves for the chosen suspicious modules by the injector status of the half-modules and rejected those with both bad statuses. Curves of the drift speed are received from a polynomial fit of measured values. For half-modules having bad injector status, requesting for the drift speed values results in obtaining identical curves representing averaged values in the given detector

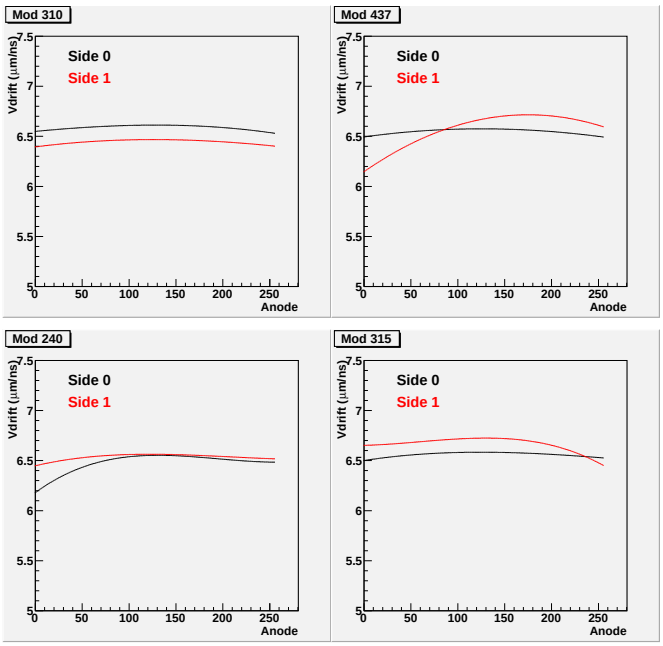

Figure 4.8: Irregularities of the dependence of drift speed on anode number.

layer. Therefore it is not possible to use these for studying any drift speed effects for individual half-modules.

I selected abnormal looking curves from plots for modules with good status. These were considered as candidates for fit failure. I found out that for some of these modules, the abnormal shape were changing from run to run. It was specified in the meetings for the presented set of plots whether the curve shapes might be caused by a fit failure or it might be a real drift speed dependence. Representative examples of found abnormalities are shown in Fig. 4.9. In case of the module presented in the upper row, curves tagged as OK probably manifest a real drift speed dependence, whereas data in the lower row indicate a fit failure.

I also spotted three modules (409, 390, 392) which had always significantly lower drift speed values compared to other modules which turned out to be a consequence of intentional decrease of the applied voltage.

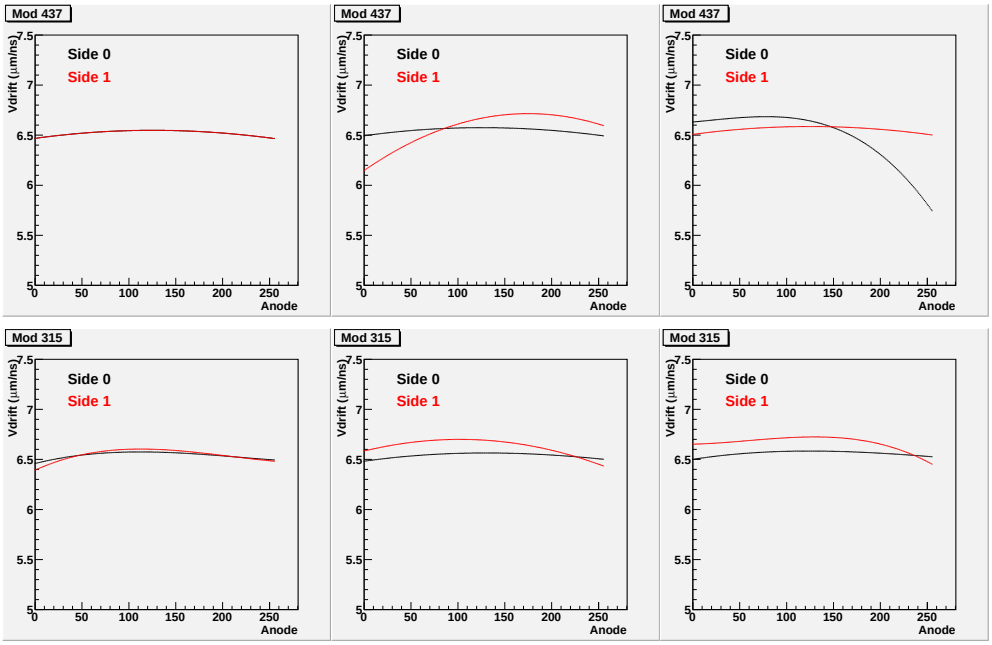

Figure 4.9: Examples of found irregularities of the drift speed dependence on anode number. Upper row: Comparison of shapes of curves for the same module in different runs and different injector statuses for the two sides (from the left: bad-bad, bad-OK, OK-bad). Lower row: Comparison of shapes of curves for the same module in different runs and all injector statuses tagged as OK.

5 Data analysis

5.1 Tools

The main tool for physics analysis of data and other statistical data processing in ALICE is ROOT [30]. ROOT is a framework based on object oriented programming and uses the C++ programming language as a scripting language for writing user analysis macros. This is provided by the C++ interpreter CINT.

To manipulate output data of the ALICE experiment a software called AliRoot [25] has been developed. AliRoot is a version of ROOT combined with libraries specialized for the ALICE experiment. AliRoot provides classes specific to the ALICE experiment. Using these classes enables simulation, reconstruction and further analysis of measured data.

The data analysis can be performed using ESD (Event Summary Data) files or AOD (Analysis Object Data) files. ESD files store information on detected events and represent a low level of processing raw data. An ESD file contains measured data from the detector organized in a fixed structure within branches of a tree. Results of processing ESD files are stored in AOD files.

In order to reconstruct jets, the FastJet package [19] is used, where various jet algorithms are implemented.

An international network of computer centres Grid [32] was used to perform computing-resources-demanding calculations. The analysis requests ("jobs") were submitted via AliEn framework [33]. Monitoring of running tasks and of data storages are provided by the project MonALISA Repository for ALICE [29].

Versions of used software are listed in Table 5.1.

Table 5.1: Versions of software used for the analysis.

Programme	Version
ROOT	v5-33-02b
AliRoot	v5-04-25-AN
FastJet	2.4.2

5.2 Analysis environment

A centrally coordinated analysis macro called "Train" is used to optimise requesting, reading and processing large data sets in complex analyses in ALICE. This macro creates an instance of an analysis manager and registers all user-defined tasks to it. All tasks are derived from a common general task prototype `AliAnalysisTaskSE`.

The Train macro used for jet analysis is `$ALICE_ROOT/PWG4/macros/AnalysisTrainPWG4Jets.C`. The body of the main Train function is divided into blocks which can be switched on and off by defining values of associated global variables. Each block corresponds to a specific type of analysis ("train wagon"). If the block is being executed (is active), tasks of the corresponding type are created, configured and added to the list of tasks treated by the analysis manager. This is handled by macros `AddTask<task name>`.

The analysis manager loads available data and for each event executes all registered tasks in serial mode where a task can process data produced by a previous task. The results are stored by default in an AOD file and user has possibility to define additional output files for each task.

In order to perform a jet analysis using cone algorithms and clustering algorithms, one can use the following task classes:
`$ALICE_ROOT/JETAN/AliAnalysisTaskJets`,
`$ALICE_ROOT/JETAN/AliAnalysisTaskJetCluster`.

To study properties of the background density of transverse momenta ρ, one can use the class
`$ALICE_ROOT/JETAN/AliAnalysisTaskJetBackgroundSubtract`.

5.3 Event and track selection

Selection of events (recorded data of detected collisions) is restricted to a range of centralities 0–80 % because of low capability to distinguish the most peripheral collisions from background events [34].

Definition of centrality bins used in my analysis is presented in Table 5.2.

Table 5.2: Definition of centrality bins.

bin number	0	1	2	3	4
centrality range [%]	0–10	10–20	20–40	40–60	60–80

Only events with primary vertex position within a range of $|z_{\mathrm{v}}| < 10$ cm, $r < 1$ cm were accepted.

The basic category of tracks for a physical analysis is "global tracks". Global tracks are a group of tracks which were reconstructed from signals in the TPC and the ITS and which meet a general set of criteria.

A subset of global tracks called "hybrid" tracks is used for jet reconstruction. A concept of hybrid tracks has been devised in order to have a maximum of tracks having reasonable resolution in transverse momentum and flat distribution in the (η, ϕ) plane [26].

A normal global track has one hit or two in the layers of the SPD and has passed the ITS refit successfully. It is therefore suitable to be used in an analysis without further modification. These tracks have the best p_{T} resolution [26].

The rest of global tracks do not have enough good hit points inside the ITS to be reconstructed properly, so they need to be modified in order to be usable. This is done by considering the event vertex to be the point of origin of the track. It is called constraining to the primary vertex and it improves the p_{T} resolution [26]. However, this operation modifies the calculation of pseudorapidity of the track and is performed after applying η cut so the final values are not affected by this cut (see Section 6.1).

The hybrid tracks consist of three categories:

- normal global tracks,
- global tracks without ITS refit, constrained to the primary vertex,

- global tracks with ITS refit but without SPD hits, constrained to the primary vertex.

Tracks may be selected according to the bit values of their mask. Each bit corresponds to a specific set of criteria on detector response and track properties. Requiring a combination of bits gives a filter (i.e. cut) for a track selection. The track is selected if it meets requirements from any of the bits included in the cut.

The categories of tracks and their bits are specified for each version of AliRoot in the macro `PWG4/macros/AddTaskESDFilterPWG4Train.C` when creating track cuts by configuring the ESD filter. Tracks are selected according to these filters when applying the ESD filter and when a track of type `AliESDtrack` is converted into a track of type `AliAODTrack` (i.e. when an ESD file is being converted into an AOD file), it gets its tags assigned.

The combination of categories of hybrid tracks used to be selected by the combination of bit filters 16 (normal global tracks) and 256 (global tracks without ITS refit or SPD hits) which make up the filter 272. These filters change in time so new functions have been written recently in order to make the track selection more straightforward. Hybrid tracks may be selected by checking
`Bool_t AliAODTrack::IsHybridGlobalConstrainedGlobal()`,
tracks constrained to the primary vertex may be selected by checking
`Bool_t AliAODTrack::IsGlobalConstrained()`.

5.4 Analysis components and settings

In this section I describe the parts of which my analysis consists. I present the purpose of each task and explain the steps of its procedure and the way it is handling data. The involved parameters of tasks are indicated in parentheses at the end of each step description. I also specify which parts of the listed features are added by me.

Since there exists no documentation of the classes used in the analysis Train, all my understanding of how these pieces of code work comes from studying their source files line by line.

The original versions of the Train and of the tasks, which I modified later, were taken from AliRoot v4-21-32-AN.

Bodies of main functions of the original tasks consist of thousands of lines of source code already and the task classes inherit their properties from more fundamental objects as a result of object oriented architecture of the framework. The original tasks also offer numerous features which I did not need. For this reasons only parts relevant for my work are mentioned in the following text. Description and explanation of the tasks procedures are simplified and reduced to a subset of needed features. However, I try to describe the key steps as precisely as possible.

For each of the listed tasks I present a table of its parameters. Only parameters relevant for the purpose of my work are included. For each parameter there are columns specifying default value of the parameter (initialized when calling constructor of the task class), value of parameter set by default during configuration of the task within the `AddTask` macro and value(s) set directly from the Train. Label "/t" in the column of values set in `AddTask` means that this parameter can

be set to a value received from the Train as an argument while calling the macro `AddTrack`. Label "x" means that the parameter is not set at all at that stage of configuration. Last column of the table contains explanation of the parameter meaning. The configuration of used tasks is presented in Tables 5.3, 5.4, 5.5, 5.6, 5.7, 5.8, 5.10.

5.4.1 General tasks

A few general purpose tasks need to be executed prior to user-defined and other specific tasks in case of having ESD files as analysis input. There was no need to modify these parts of the Train and they were therefore configured with default settings except for fixing minor bugs due to limited backward compatibility of newer versions of AliRoot.

In case of analysing AOD files, the results of these tasks are stored in the input AOD files already.

- Physics Selection

  The task `AliPhysicsSelectionTask` checks whether an event is a candidate for a collision or not and marks the event with the result of this decision. The decision is based on applying selection cuts on triggers. If another task has this kind of filter switched on, it is executed for an event only when the event is selected by this task.

- Centrality Selection

  The task `AliCentralitySelectionTask` is used to analyse determination of centrality from the input ESD file.

- ESD Filter

  The task `AliAnalysisTaskESDfilter` converts an input ESD file into an output AOD file. It also defines various cuts for track selection by combining requirements on response from different parts of detectors.

5.4.2 Tracks

I created the class `AliAnalysisTaskTracks` to display the distribution of the direction of momenta of reconstructed tracks in the η-ϕ plane.

The purpose of including this task in my jet analysis is to control uniform distribution of reconstructed particle tracks which are used as the input of jet finders. Acceptance-related defects of the detector and selection problems can be revealed by checking outputs of this task.

The task loads 4-momenta of received particle tracks and selects the tracks according to their filter type (`fFilterType`), bit mask (`fFilterMask`) and constraint (`fFilterConstrained`). Other options are to apply also η cut and p_{T} cut (`fTrackEtaWindow`, `fTrackPtCut`). Chosen properties of tracks are filled in the following histograms:

- p_{T}, ϕ, η, η-ϕ spectrum of tracks

- p_{T} spectrum of "good", "bad", all tracks — distribution of transverse momenta of tracks inside the TPC η range, of tracks outside the range and of all selected tracks
- $\Delta\eta$ spectrum of "bad" tracks — distribution of η excess of "bad" tracks $[\Delta\eta = \eta\,(1 - 0.9/\,|\eta|)]$

Table 5.3: Values of parameters used in the task `AliAnalysisTaskTracks`.

Parameter	Task	AddTask	Train	Description
`fTrackTypeRec`	0	x	1	type of tracks (AOD tracks)
`fFilterMask`	0	x	0, 272	track mask used as bit filter
`fFilterType`	0	x	2	track filter type (hybrid tracks)
`fFilterConstrained`	0	x	0, 1, 2	track constraint (all, constrained only, not constrained only)
`fTrackEtaWindow`	0.	x	0.	track η window
`fTrackPtCut`	0.	x	0.	min. track p_{T} to be accepted [GeV/c]

5.4.3 Cone jets finders

The task `AliAnalysisTaskJets` reconstructs jets with jet finders using cone algorithms UA1 and SISCone. It takes reconstructed tracks momenta as input, creates a branch to store found jets, creates and fills related histograms.

For cones algorithms used by this task, the jet finding itself is performed by an object of a class derived from a general class `AliJetFinder`. The process of finding jets is launched by calling the member function `FindJets()`, the body of which is specific to the algorithm being used.

The configuration parameters of the algorithm are stored in members of an associated class which is derived from the class `AliJetHeader`. Some other parameters are kept by class `AliJetAODReaderHeader` derived from the class `AliJetReaderHeader` (see Table 5.4).

Scheme of the task steps:

- run the jet finder
- if the leading jet has p_{T} greater than the cut value, set output event handler to fill this event in the AOD file (`fFilterPt`)

UA1 jet algorithm

In case of the algorithm UA1, the task procedure is handled by an object of the class `AliUA1JetFinderV1` where the finding procedure is implemented in the member function `RunAlgoritm()`.

Parameters values for this task are kept by the class `AliUA1JetHeaderV1`.

Scheme of steps of the member function `FindJets()`:

Table 5.4: Values of parameters used in the task `AliAnalysisTaskJets`.

Parameter	Task	AddTask	Train	Description
		`AliAnalysisTaskJets`		
`fFilterPt`	0.	x	x	min. p_{T} of leading jet to write event in AOD [GeV/c]
		`AliJetHeader`		
`fJetEtaMax`	0.5	1.5	x	max. jet η
`fJetEtaMin`	-0.5	-1.5	x	min. jet η
`fJetPhiMax`	2π	x	x	max. jet ϕ
`fJetPhiMin`	0	x	x	min. jet ϕ
		`AliJetReaderHeader`		
`fPtCut`	2.0	0.15/t	0.15/1./2.	min. track p_{T} to be accepted [GeV/c]
		`AliJetAODReaderHeader`		
`fTestFilterMask`	0	32/t	272	track mask used as bit filter

- get tracks from AOD
- fill η-ϕ map with p_{T} of tracks
- sum up p_{T} of all tracks as total transverse energy E_{T} in array
- calculate standard deviation of energy (p_{T}) in map array
- iterate until required precision (`fPrecBg`)
  - run cone algorithm finder (`RunAlgoritm()`)
  - take only accepted jets per event (`fNAcceptJets`)
  - subtract background from jet momenta
    (if `fBackgMode` = 1, call `SubtractBackg()`)
- apply η, E_{T} cut on jets (`fJetEtaMax`, `fJetEtaMin`, `fMinJetEt`)
- set jet area as $A_{\mathrm{jet}} = \pi R^2 - A_{\mathrm{out}}$, where A_{out} is area outside η acceptance (`fLegoEtaMax`, `fLegoEtaMin`, `fConeRadius`)
- add jet to the list

Scheme of steps of the member function `RunAlgoritm()`:

- fill array content (p_{T}, η, ϕ) into cells, treat p_{T} as transverse energy E_{T} (`fLegoNbinEta`, `fLegoNbinPhi`)
- load finder parameters from header (`fMinMove`, `fMaxMove`, `fConeRadius`, `fEtSeed`)
- sort cells by energy
- loop over cells (looking for centroids)

  - take cell as a centroid
  - apply seed energy filter (`fEtSeed`)
  - exclude used cells
  - loop over cells
    * calculate distance between two cells
    * if distance $< R$ (cell is inside cone) (`fConeRadius`)
      · calculate new η, ϕ of centroid including this cell weighted with cell energy
      · if cone did not move much, stop loop (`fMinMove`)
      · if cone moved too much, reset centroid values from previous iteration (`fMaxMove`)
      · else store new centroid values
  - sum up energy inside cone (`fConeRadius`)
  - estimate max fluctuation of background in cone
  - if E_{T} in cone > estimated background E_{T}, select jet
  - check whether there are not too many found jets (`kMaxJets` = 30)
- sort found jets by E_{T}
- store found jets

Scheme of steps of the member function `SubtractBackg()`:

- loop over all particles (calculate energy inside and outside cones)
  - loop over jets
    * if particle inside jet cone (`fConeRadius`)
      · apply p_{T} cut (`fReader->GetCutFlag()`)
      · add particle p_{T} to the jet E_{T}
  - if particle outside jet cone
    * apply p_{T} cut
    * add particle p_{T} to the outside E_{T} ($E_{\mathrm{T}}^{\mathrm{out}}$)
- calculate maximum acceptance area as $A_{\mathrm{acc}} = 4\pi\eta_{\mathrm{max}}$ (`fLegoEtaMax`)
- loop over jets (estimate jets and background areas)
  - calculate jet area A_{jet} within acceptance (`fLegoEtaMax`, `fLegoEtaMin`, `fConeRadius`)
  - subtract jet area from outside area A_{out}
- loop over jets (subtract background using area method)
  - calculate and set corrected jet E_{T} as $E_{\mathrm{T}\,\mathrm{jet}}^{\mathrm{corr}} = E_{\mathrm{T}\,\mathrm{jet}} - A_{\mathrm{jet}} E_{\mathrm{T}}^{\mathrm{out}} / A_{\mathrm{out}}$
- scale total background energy as $E_{\mathrm{T}}^{\mathrm{bg}} = E_{\mathrm{T}}^{\mathrm{out}} A_{\mathrm{acc}} / A_{\mathrm{out}}$ (`fLegoEtaMax`)

Table 5.5: Values of parameters used in the task `AliAnalysisTaskJets` by the jet finder for the UA1 algorithm (`AliUA1JetHeaderV1`).

Parameter	Task	AddTask	Train	Description
`fConeRadius`	0.3	0.4/t	0.4	cone radius
`fEtSeed`	3.0	4.	x	min. seed E_{T} [GeV]
`fMinJetEt`	10.	5.	x	min. jet E_{T} [GeV]
`fMinMove`	0.05	x	x	min. cone move
`fMaxMove`	0.15	x	x	max. cone move
`fBackgMode`	1	0/t	0/1	background subtraction mode
`fPrecBg`	0.035	x	x	maximum value of change for background [%]
`fNAcceptJets`	3	6	x	number of accepted jets per events
`fLegoNbinEta`	36	274	x	number of cells in η
`fLegoNbinPhi`	124	432	x	number of cells in ϕ
`fLegoEtaMin`	-0.9	-2	x	min. η of map
`fLegoEtaMax`	0.9	$+2$	x	max. η of map
`fLegoPhiMin`	0.	x	x	min. ϕ of map
`fLegoPhiMax`	2π	x	x	max. ϕ of map

SISCone jet algorithm

In case of the algorithm SISCone, the task procedure is handled by an object of the class `AliSISConeJetFinder` where the finding procedure is implemented through calling FastJet.

Parameters values for this task are kept by the class `AliSISConeJetHeader`.

Scheme of steps of the member function `FindJets()`:

- configure SISCone plugin (`fConeRadius`, `fPtProtoJetMin`)
- load 4-momenta of tracks
- apply minimum p_{T} cut on tracks (`fPtCut`)
- add 4-momenta of track as massive particles in the list
- set ghost jets parameters and define area type (`fAreaTypeNumber`, `fGhostEtaMax`, `fGhostArea`)
- find jets (run FastJet with SISCone plugin)
- extract inclusive jets having p_{T} above the cut value (`fMinJetPt`)
- sort jets by p_{T}
- set effective area of jets
- add jets to the list

Table 5.6: Values of parameters used in the task `AliAnalysisTaskJets` by the jet finder for the SISCone algorithm (`AliSISConeJetHeader`).

Parameter	Task	AddTask	Train	Description
`fAreaTypeNumber`	4	4	x	type of area (passive)
`fBGMode`	1	0	x	switch for background subtraction
`fConeRadius`	0.7	0.4/t	0.4	cone radius
`fGhostEtaMax`	4.0	4	x	max. η in which a ghost can be generated
`fGhostArea`	0.05	0.05	x	area of one ghost
`fMinJetPt`	2	5	x	min. jet energy [GeV]
`fPtProtoJetMin`	2	0	x	min. p_{T} of protojets [GeV/c]

5.4.4 Clustering jet finders

Task `AliAnalysisTaskJetCluster` reconstructs jets with jet finders using clustering algorithms k_{t} and anti-k_{t} and calculates p_{T} background density ρ. It takes reconstructed tracks 4-momenta as an input and uses them to find jets through calling FastJet. Calculating p_{T} background density from found jets is provided also by FastJet. The task generates a defined number of cones in random directions and sums up p_{T} of all particles inside each cone. A set of tracks with randomized directions of input momenta is generated while keeping original values of p_{T}. These randomized tracks are used to find random jets. Another value of background density (ρ_2) is calculated from the random jets. The task also creates and fills related histograms.

My modifications: I extracted the block of event selection based on centrality values and vertex position and I transformed it into a header function which may be included in any class in order to allow selection of the same events across different tasks. I extended the branch for random cones to 3 branches to allow generating random cones for different numbers of bypassed leading jets (0–2). I changed the system of naming output branches to a more reasonable scheme. I added several control log messages. I fixed a few bugs (jets were not stored in the detected extension output file, name of the branch for random cones had a suffix "Skip" which prevented the branch from being found by the subtraction task).

Scheme of the task steps:

- apply selection filter on the event (`fVtxZCut`, `fVtxR2Cut`, `fCentCutLo`, `fCentCutUp`)
- get tracks of reconstructed particles from AOD (`fTrackTypeRec`)
  - apply type filter (`fFilterType`)
  - apply bit filter (`fFilterMask`)
  - apply η cut (`fTrackEtaWindow`)
  - apply p_{T} cut (`fTrackPtCut`)
  - add track to the list
  - sort tracks

- loop over reconstructed tracks
  - add the track momentum as a massless reconstructed particle to the list
- specify ghosts parameters (`fGhostEtamax`, `fActiveAreaRepeats`, `fGhostArea`)
- define area and its type (active area)
- define jet finder (`fAlgorithm`, `fRparam`, `fRecombScheme`, `fStrategy`)
- find jets from the list of reconstructed particles (i.e. run FastJet)
- set ϕ-y range where to calculate background (`fGhostEtamax`, `fRparam`)
- sort jets by p_{T}
- loop over all reconstructed jets
  - apply $p_{\mathrm{T jet}}$ cut (`fJetOutputMinPt`)
  - store jet and its area (scalar area A_{jet} and 4-vector area) in the output jet branch
- add the random cones (if we want them), loop over number of leading jets to be bypassed (`fNSkipLeadingCone`)
  - loop over random cones creation (`fNRandomCones`)
    - create a random cone (massless jet with random η, ϕ) within the η acceptance with $p_{\mathrm{T}} = 1$ GeV/c (`fTrackEtaWindow`)
    - reject cone if overlapping with leading reconstructed jets (i.e. distance from jet centre $D < 2R + 0.2$) (`fRparam`)
    - reject cone if overlapping with previous cones to avoid double counting
    - write cone in the branch for random cones
  - loop over the reconstructed tracks
    - add the p_{T} of the track to the random cone background energy E_{bg} if the track is inside the cone (`fRparam`)
  - loop over random cones
    - rescale the random cone momentum so that $p_{\mathrm{T,RC}} = E_{\mathrm{bg}}$
    - set cone area $A_{\mathrm{RC}} = \pi R^2$ (`fRparam`)
- if we want to calculate background (`fUseBackgroundCalc`)
  - run FastJet to calculate background (scalar ρ_1, 4-vector ρ_0) from reconstructed jets, excluding 2 hardest jets
  - write ρ, σ, mean area values in the output branch for background
- if we want event $p_{\mathrm{T jet}}$ filter (`fJetTriggerPtCut`)

- if we have external background branch, load ρ_2 (`fBackgroundBranch`)
- loop over reconstructed jets
  - calculate corrected $p_{\mathrm{T jet}}$ as $p_{\mathrm{T jet}}^{\mathrm{corr}} = p_{\mathrm{T jet}} - \rho_2 A_{\mathrm{jet}}$
  - if $p_{\mathrm{T jet}}^{\mathrm{corr}}$ is above threshold, flag event as OK (`fJetTriggerPtCut`)

- if event is flagged as OK, set output event handler to fill this event in the AOD file

Table 5.7: Values of parameters used in the task `AliAnalysisTaskJetCluster`.

Parameter	Task	AddTask	Train	Description
`fUseBackgroundCalc`	0	x	x/1	switch for background calculations
`fEventSelection`	0	x	1	switch for event selection
`fFilterMask`	0	16/t	272	track filter mask
`fFilterType`	0	0	x	track filter type
`fTrackTypeRec`	0	1	x	type of tracks
`fNSkipLeadingRan`	0	0/t	0	number of leading tracks to be skipped in the randomized event
`fNSkipLeadingCone`	0	2/t	x/0/2	number of leading jets to be bypassed by the random cones
`fNRandomCones`	0	x	x/1	number of generated random cones
`fTrackEtaWindow`	0.9	0.9/t	0.9	track η window
`fTrackPtCut`	0.	0.15/t	0.15/1./2.	min. track p_{T} [GeV/c]
`fJetOutputMinPt`	0.15	0	x	min. p_{T} of jet to be written out
`fJetTriggerPtCut`	0	x	x/20	min. jet p_{T} for event to be written [GeV/c]
`fVtxZCut`	8	x	10	vertex z cut [cm]
`fVtxR2Cut`	1	x	1	vertex r^2 cut [cm^2]
`fCentCutUp`	0	x	0	min. centrality [%]
`fCentCutLo`	0	x	80	max. centrality [%]
`fBackgroundBranch`	""	x	k_{t}, $R = 0.4$	branch to load ρ from
`fRparam`	1.0	0.4/t	0.1–0.6	radius
`fAlgorithm`	0	0/t	0/2	jet algorithm (k_{t}, anti-k_{t})
`fStrategy`	Best	x	x	strategy of jet finder
`fRecombScheme`	BIpt	x	x	recombination scheme of jet finder
`fAreaType`	active	x	x	jet area type
`fGhostArea`	0.01	x	x	area of one ghost
`fGhostEtamax`	1.5	x	0.9	ghosts η window

5.4.5 Background subtraction

The task `AliAnalysisTaskJetBackgroundSubtract` is used to subtract underlying event background and to perform background analysis. Input for this task is a list of jet branches and a branch with background to be used for subtraction. The task creates a branch of jets having corrected momenta. Results of the background analysis are stored in the following histograms:

- ρ-vs-centrality distribution — distribution of ρ calculated from jets in accepted events, depending on event centrality
- $\Delta\rho$ distribution — comparison of ρ value with the value of ρ_{ref} calculated in a reference branch for the same event
- δp_{T} distribution — background p_{T} fluctuation calculated from the random cones

My modifications: I added event filter (centrality and vertex position), branch for reference background, definition of centrality bins, histograms for $\Delta\rho$, histograms for δp_{T}, requirement of positive ρ to be filled in histograms, control log messages. I extended the array for random cones to 3 arrays to allow comparison of background fluctuations for different numbers of bypassed leading jets.

Scheme of the task steps:

- apply selection filter on the event (`fVtxZCut`, `fVtxR2Cut`, `fCentCutLo`, `fCentCutUp`)
- load reference background branch (`fRefBranch`)
- load background branch (`fBackgroundBranch`)
- load branches with random cones
- load event centrality value
- load σ, ρ, reference ρ_{ref} values (ρ_1 for scalar subtraction, ρ_0 for 4-vector subtraction) (`fSubtraction`)
- if $\rho > 0$, fill ρ and centrality values in the ρ vs centrality histogram
- if $\rho > 0$ and $\rho_{\mathrm{ref}} > 0$, fill $\Delta\rho = \rho - \rho_{\mathrm{ref}}$ in the corresponding histogram according to defined centrality bins ranges
- loop over available branches with random cones
  - for each cone in the branch fill $\delta p_{\mathrm{T}} = p_{\mathrm{T,RC}} - \rho A_{\mathrm{RC}}$ in the corresponding histogram according to defined centrality bins ranges and the number of bypassed leading jets
- loop over branches of input jets
  - loop over input jets in the branch
    - load jet and copy it into a new jet

    - if scalar subtraction chosen
        - calculate background p_{T} as $p_{\mathrm{Tbg}} = \rho A_{\mathrm{jet}}$
        - calculate corrected p_{Tjet} as $p_{\mathrm{T}_{\mathrm{jet}}^{\mathrm{corr}}} = p_{\mathrm{Tjet}} - p_{\mathrm{Tbg}}$
        - if $p_{\mathrm{T}_{\mathrm{jet}}^{\mathrm{corr}}} < 0$, flag jet as not to be stored (bad)
        - else rescale momentum of the new jet with scaling ratio $p_{\mathrm{T}_{\mathrm{jet}}^{\mathrm{corr}}}/p_{\mathrm{Tjet}}$ (while keeping direction and mass)
        - store ρA_{jet} as the background energy of the new jet
    - if 4-vector subtraction chosen and if the jet has a defined area 4-vector $\mathbf{A}_{\mathrm{jet}}$
        - calculate 4-vector background momentum $\mathbf{P}_{\mathrm{bg}} = \rho \mathbf{A}_{\mathrm{jet}}$
        - calculate corrected p_{Tjet} as $p_{\mathrm{T}_{\mathrm{jet}}^{\mathrm{corr}}} = p_{\mathrm{Tjet}} - p_{\mathrm{Tbg}}$
        - if $E_{\mathrm{bg}} > E_{\mathrm{jet}}$ and $p_{\mathrm{Tbg}} > p_{\mathrm{Tjet}}$, flag jet as bad
        - else store the 4-momentum of the new jet $\mathbf{P}_{\mathrm{jet}}^{\mathrm{corr}} = \mathbf{P}_{\mathrm{jet}} - \mathbf{P}_{\mathrm{bg}}$
        - store magnitude of the background momentum as the background energy of the new jet
    - if the jet is flagged as OK
        - write the new jet in the output branch of corrected jets
- sort new jets

Table 5.8: Values of parameters used in the task `AliAnalysisTaskJetBackgroundSubtract`.

Parameter	Task	AddTask	Train	Description
`fSubtraction`	2	1/t	1/2	subtraction method
`fRefBranch`	""	x	k_{t}, $R = 0.4$, $p_{\mathrm{T}} \geq 150\,\mathrm{MeV}/c$	reference background branch
`zCut`	8	x	10	vertex z cut [cm]
`r2Cut`	1	x	1	vertex r^2 cut [cm^2]
`centCutLow`	0	x	0	min. centrality [%]
`centCutHigh`	100	x	80	max. centrality [%]

5.4.6 Jet histograms

The task `AliAnalysisTaskHisto` represents the final stage of processing data. It loads the branches of reconstructed jets and extracts from them interesting jet properties which are subsequently used to create histograms with jet spectra etc.

Following histograms are filled:

- number of events per centrality bin
- p_{T}, η, ϕ spectrum of all jets in a branch
- p_{T}, η spectra of jets in centrality bins
- η spectra of jets in p_{T} bins

- η-ϕ distribution of jets
- η-p_{T} distribution of jets
- distribution of number of jets per event (in total and in centrality bins)

The task also allows to enable an optional output file in which a tree is stored with properties of jets in its branches (energy, momentum, mass, p_{T}, η, ϕ, area, error of area determination, background energy, event centrality, event number).

Scheme of the task steps:

- apply event filter
- load centrality
- load event number
- find jet branch in output and load jets
- loop over jets
  - load values of jet properties
  - fill tree branches
  - fill jet histograms
- add event to the counter histogram of number of events in centrality bin
- add number of jets to the counter histogram of number of jets per event

Definition of p_{T} bins is presented in Table 5.9.

Table 5.9: Definition of p_{T} bins.

Bin number	0	1	2
p_{T} range [GeV/c]	0–10	10–20	20–1000

Table 5.10: Values of parameters used in the task `AliAnalysisTaskHisto`.

Parameter	Task	AddTask	Train	Description
`zCut`	8	x	10	vertex z cut [cm]
`r2Cut`	1	x	1	vertex r^2 cut [cm^2]
`centCutLow`	0	x	0	min. centrality [%]
`centCutHigh`	100	x	80	max. centrality [%]
`fillTree`	0	0/t	x	switch for saving jet tree

Overview of all configurations, for which the jet analysis was performed, is in Table 5.11. Combinations for the background analysis are listed in Table 5.12. The symbol $p_{\mathrm{T}}^{\mathrm{min}}$ denotes the threshold for minimum p_{T} of tracks accepted for jet reconstruction. For each jet branch used for background analysis the random cones generation was performed for the whole range of numbers of bypassed leading jets (i.e. 0, 1, 2).

Table 5.11: Parameter combinations used in jet analysis.

algorithm	R	$p_{\mathrm{T}}^{\mathrm{min}}$ [GeV/c]	subtraction method
UA1	0.4	0.15, 1, 2	none, area
SISCone	0.4	0.15, 1, 2	none, scalar
k_{t}	0.2, 0.3, 0.4	0.15, 1, 2	none, scalar, 4-vector
k_{t}	0.1, 0.5, 0.6	0.15	none, scalar, 4-vector
anti-k_{t}	0.2, 0.3, 0.4	0.15, 1, 2	none, scalar, 4-vector

Table 5.12: Parameter combinations used in background analysis.

algorithm	R	$p_{\mathrm{T}}^{\mathrm{min}}$ [GeV/c]
k_{t}	0.4	0.15, 1, 2
k_{t}	0.1, 0.2, 0.3, 0.5, 0.6	0.15

6 Analysis results

Analysed data were measured in 2010 in collisions of lead nuclei $^{208}_{82}$Pb at the energy per nucleon pair in the centre-of-mass system $\sqrt{s_{\mathrm{NN}}} = 2\frac{Z_{\mathrm{Pb}}}{A_{\mathrm{Pb}}}E_{\mathrm{beam}} = 2.76\,\mathrm{TeV}$ where the nominal beam energy was $E_{\mathrm{beam}} = 3.5\,\mathrm{TeV}$, $Z_{\mathrm{Pb}}, A_{\mathrm{Pb}}$ are the proton number and the nucleon number of the lead nucleus respectively.

Final analysis was performed on AOD files matching the pattern `/alice/data/2010/LHC10h/*/ESDs/pass2/AOD086/*/AliAOD.root`.
Analysed runs were selected according to the ALICE Run Condition Table[1] (complete list is in Table A.1).

The data sample consists of 13.4 millions of events (selected according to the criteria presented in Section 5.3). Number N_{ev} of analysed events in individual centrality bins are presented in Table 6.1 with corresponding values of N_{coll} and their systematic errors.

Table 6.1: Numbers of analysed events and of binary nucleon collisions [27].

Centrality [%]	N_{ev}	N_{coll}	Sys. err. of N_{coll}
0–10	1 674 151	1502.7	169.9
10–20	1 664 907	923.26	99.6
20–40	3 349 604	438.8	43.9
40–60	3 346 061	128.2	12.7
60–80	3 348 804	26.82	2.46
0–80	13 383 527	450.33	48.1

6.1 Track quality

Figures 6.1, 6.2, 6.3, 6.4 show distributions of p_{T}, ϕ, η, η-ϕ of hybrid tracks which met all selection criteria (see Table 5.3) and a subset of which was accepted to be used for jet reconstruction.

The spectrum of p_{T} for tracks has exponential shape for low p_{T} and for $p_{\mathrm{T}} > 4\,\mathrm{GeV}/c$ changes into power law. This is in qualitative agreement with predictions of perturbative QCD (see Section 1.4).

A shallow dip in the η spectrum of tracks is visible for $\eta \approx 0$ in Fig. 6.4. This is due to presence of the central electrode of the TPC which is slightly affecting the acceptance of the TPC.

When I checked the η-ϕ distribution of selected hybrid tracks, I noticed presence of a few tracks with $|\eta| > 0.9$. That seemed to be an unwanted phenomenon. I investigated this observation in detail in order to verify whether this fact might affect the estimation of the tracking efficiency [26].

For this purpose, I enriched the task with additional histograms to estimate the fraction of contribution of "bad" tracks. A candidate for a cause of this effect seemed to be the process of constraining to the primary vertex because pseudorapidity value of a track can be shifted during this procedure (see Section 5.3).

[1] `http://alimonitor.cern.ch/configuration/index.jsp?partition=LHC10h`

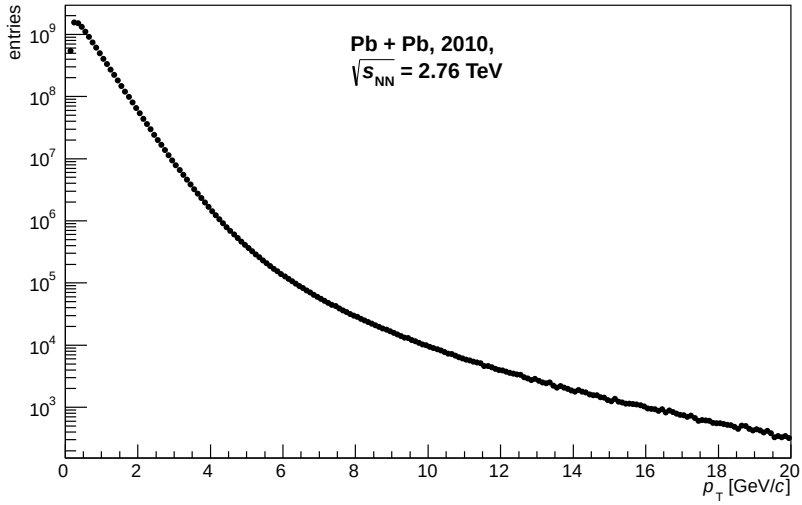

Figure 6.1: Uncorrected p_{T} spectrum of charged tracks. Pb + Pb, 2010, $\sqrt{s_{\mathrm{NN}}} = 2.76$ TeV.

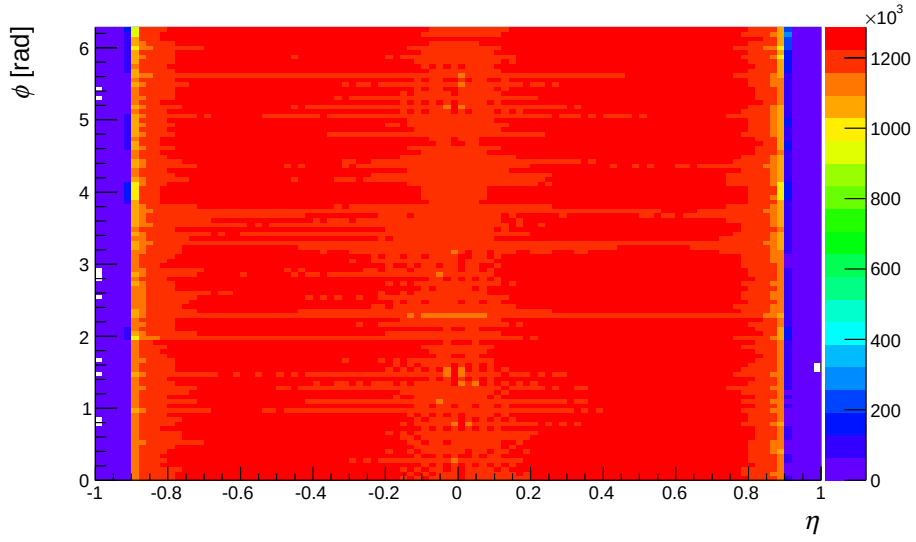

Figure 6.2: Distribution of charged-track directions in η-ϕ. Pb+Pb, 2010, $\sqrt{s_{\mathrm{NN}}} = 2.76$ TeV.

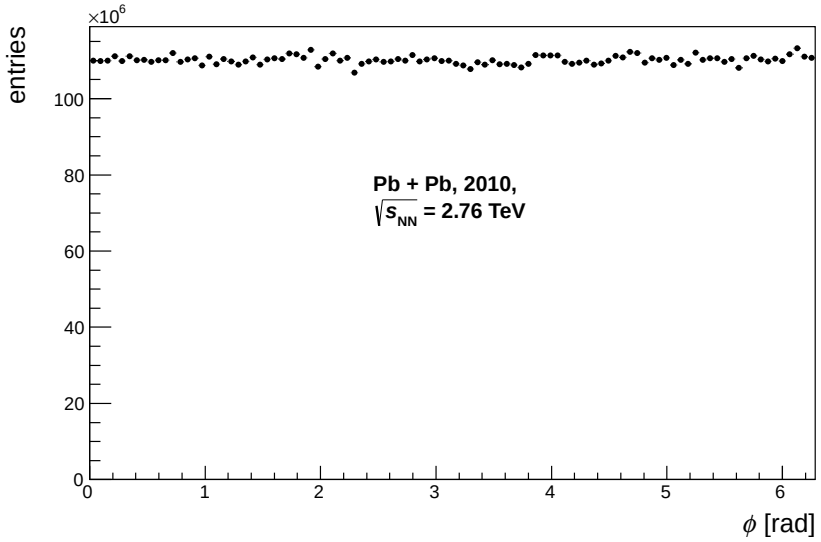

Figure 6.3: Distribution of charged tracks in ϕ. Pb + Pb, 2010, $\sqrt{s_{\mathrm{NN}}} = 2.76\,\mathrm{TeV}$.

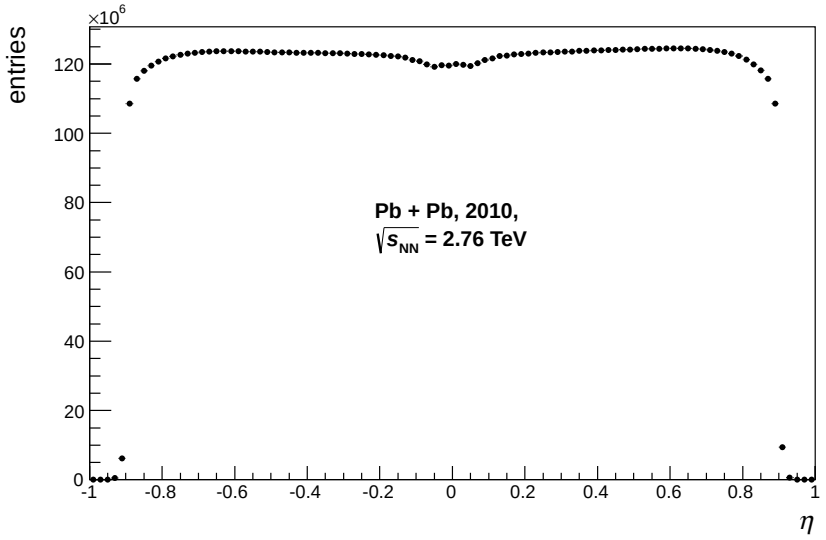

Figure 6.4: Distribution of charged tracks in η. Pb + Pb, 2010, $\sqrt{s_{\mathrm{NN}}} = 2.76\,\mathrm{TeV}$.

I investigated hybrid track distribution for events of the run 137844, where 74.6 % of tracks were normal hybrid tracks and 25.4 % were constrained hybrid tracks. In order to verify the influence of constraining, I checked the η distribution for normal tracks and for constrained tracks separately. The results confirmed that almost all tracks exceeding the η range come from the category of constrained tracks (see Figure 6.5).

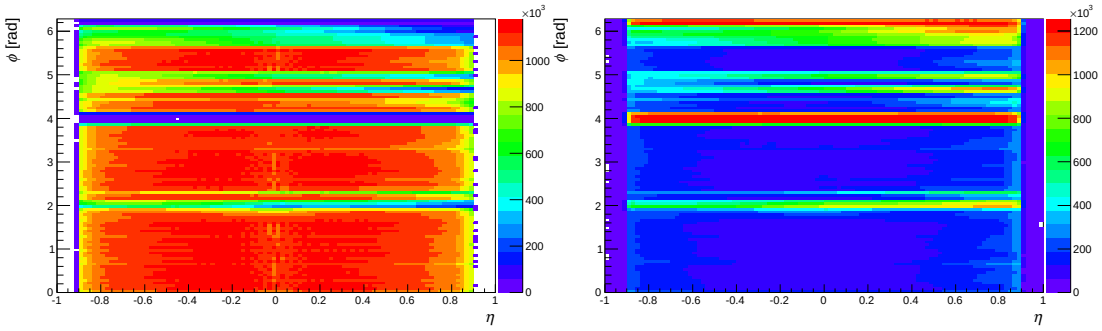

Figure 6.5: Distribution of charged-track directions in η-ϕ for normal (left) and constrained (right) tracks separately. (This plot is made for the whole analysed data set.) Pb + Pb, 2010, $\sqrt{s_{\mathrm{NN}}} = 2.76$ TeV.

In order to estimate and evaluate the contribution of "bad" tracks to the population of hybrid tracks, I produced p_{T} spectra of "bad" tracks and all hybrid tracks and made a ratio of them. This ratio is presented in Figure 6.6 where a fraction of "bad" tracks is displayed for each p_{T} bin.

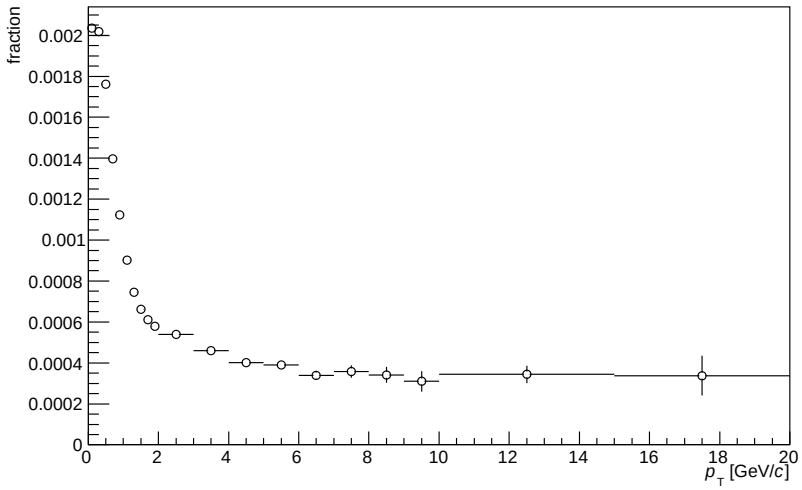

Figure 6.6: Fraction of number of charged tracks with $|\eta| > 0.9$ for different p_{T} bins. (This plot is made for the whole analysed data set.) Pb + Pb, 2010, $\sqrt{s_{\mathrm{NN}}} = 2.76$ TeV.

Low-p_{T} tracks represent the highest relative contribution with maximal value of fraction about 0.2 % which is within the 4 % uncertainty of the tracking efficiency [26].

Figure 6.7 shows the distribution of the excess in η of "bad" tracks. The excess is defined as $\Delta\eta = \eta\,(1 - 0.9/\,|\eta|)$. The excess values are observed to be restricted to a range of $|\Delta\eta| < 0.15$.

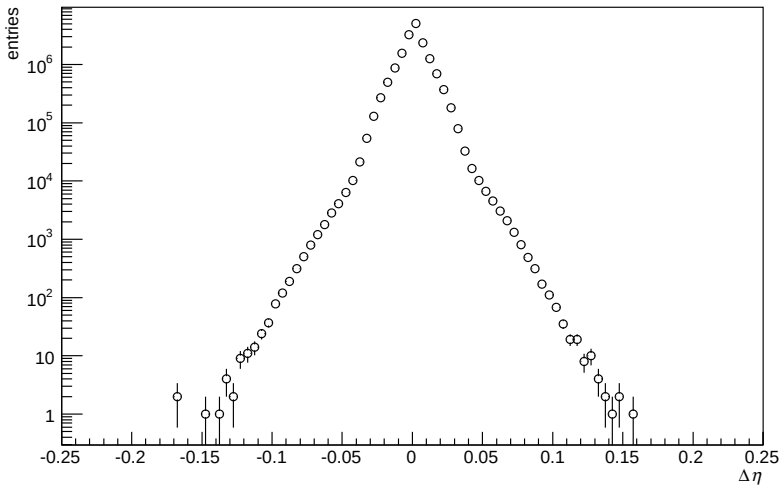

Figure 6.7: Distribution of the η excess. (This plot is made for the whole analysed data set.) Pb + Pb, 2010, $\sqrt{s_{\mathrm{NN}}} = 2.76$ TeV.

The results of this study were presented in a meeting[2] of the ALICE jet group (PWG-JE) and the subsequent discussion resulted in a decision to perform η cut and constraining in the reversed order, that means that in new versions of track cuts, cutting on η will be applied after constraining tracks to the primary vertex in order to prevent users from getting into potential trouble because of presence of tracks exceeding the expected range of pseudorapidity. Also an explanatory TWiki web page[3] page was created to document this issue.

6.2 Study of background from underlying event

The density of background transverse momenta ρ (see definition in equation (2.2)) was calculated for the jets reconstructed with the k_{t} jet algorithm with different settings of R and $p_{\mathrm{T}}^{\mathrm{min}}$ values, presented in Table 5.12.

6.2.1 Background dependence on centrality

The density of background strongly depends on centrality. The more central are nuclei collisions, the more difficult and challenging is the appropriate determination and subtraction of background from underlying event.

Figures 6.8, 6.9, 6.10 show the distribution of values of the background density ρ as a function of event centrality for $R = 0.4$ and of different values of the track-minimal-transverse-momentum threshold $p_{\mathrm{T}}^{\mathrm{min}}$. Plots have different y-axis scales in order to emphasise details.

[2] `https://indico.cern.ch/conferenceDisplay.py?confId=192221`

[3] `https://twiki.cern.ch/twiki/bin/viewauth/ALICE/HybridTrackEtaTooLarge`

Histograms were fitted with normal distribution in centrality bins of width of 10 %. The values of mean density $\langle\rho\rangle$ and of its standard deviation σ_ρ, obtained from the fit, are presented in Table 6.2 and depicted in the figures as black crosses of height $2\sigma_\rho$ centred at $\rho = \langle\rho\rangle$.

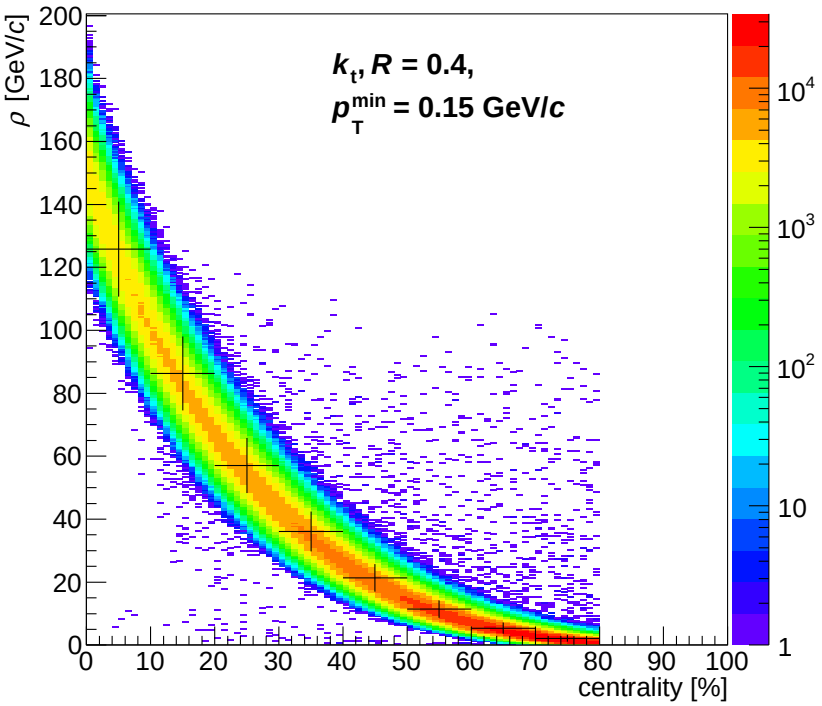

Figure 6.8: Dependence of background density on centrality for $p_{\mathrm{T}}^{\mathrm{min}} = 0.15\,\mathrm{GeV}/c$, $R = 0.4$. Pb + Pb, 2010, $\sqrt{s_{\mathrm{NN}}} = 2.76$ TeV.

Table 6.2: Mean background density $\langle\rho\rangle$ and its standard deviation σ_ρ for all $p_{\mathrm{T}}^{\mathrm{min}}$ values and for two centrality bins.

$p_{\mathrm{T}}^{\mathrm{min}}$ [GeV/c]	$\langle\rho\rangle$ [GeV/c]	σ_ρ [GeV/c]
0–10 %		
0.15	125.772 ± 0.014	15.075 ± 0.006
1.00	53.212 ± 0.007	7.861 ± 0.004
2.00	11.015 ± 0.003	2.665 ± 0.001
40–50 %		
0.15	21.318 ± 0.005	4.374 ± 0.002
1.00	8.235 ± 0.002	2.349 ± 0.001
2.00	4.647 ± 0.011	0.960 ± 0.008

The shape of the dependence of ρ on centrality confirms that the contribution of the particles from underlying events to the p_{T} of reconstructed jet candidates is highest for the most central collisions.

The influence of higher track-p_{T} threshold on reduction of background density is very strong. This indicates that soft particles with $p_{\mathrm{T}} \lesssim 2\,\mathrm{GeV}/c$ represent a large fraction of tracks constituting jets reconstructed with the k_{t} algorithm. If

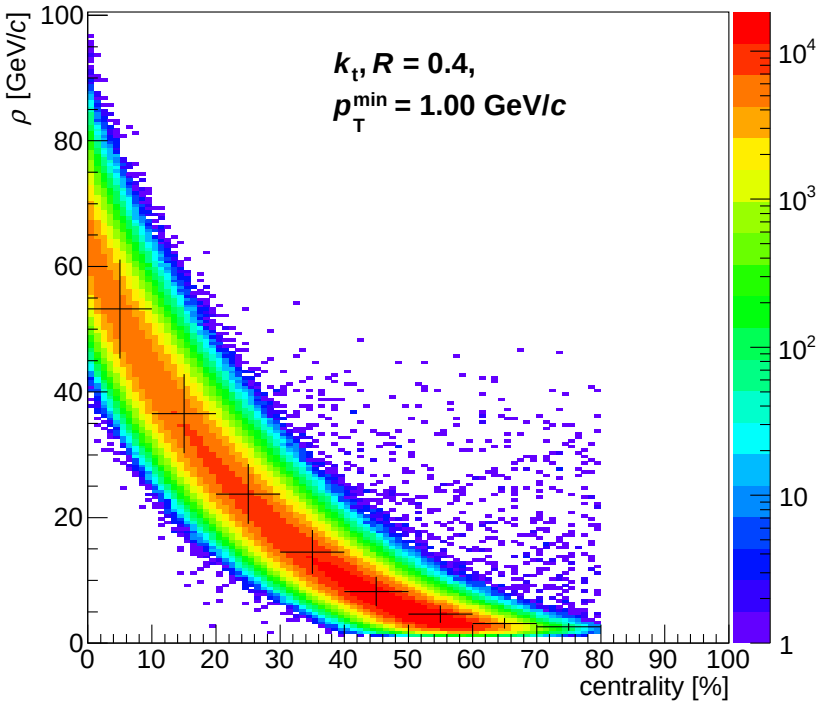

Figure 6.9: Dependence of background density on centrality for $p_{\mathrm{T}}^{\mathrm{min}} = 1\,\mathrm{GeV}/c, R = 0.4$. Pb + Pb, 2010, $\sqrt{s_{\mathrm{NN}}} = 2.76$ TeV.

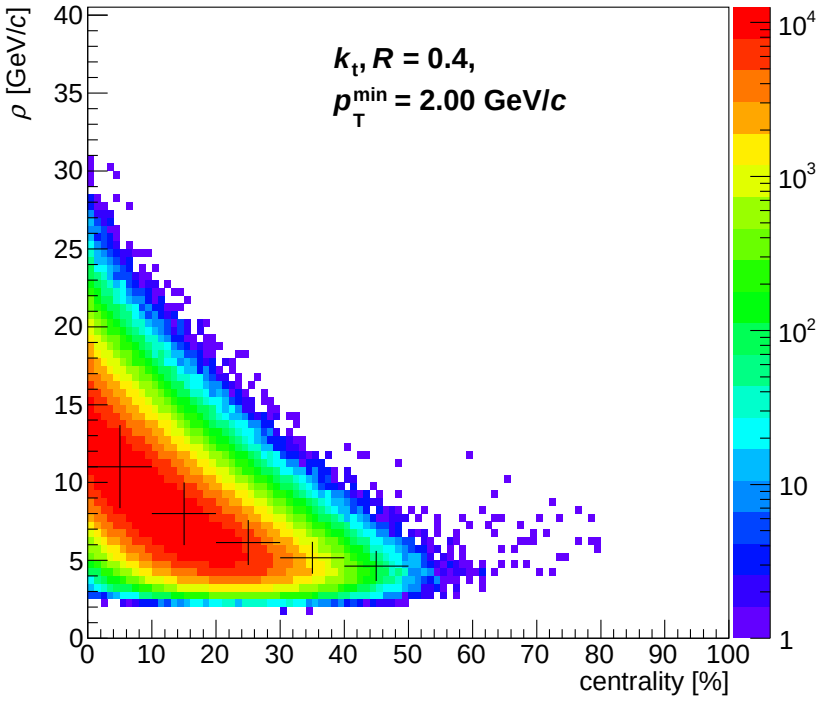

Figure 6.10: Dependence of background density on centrality for $p_{\mathrm{T}}^{\mathrm{min}} = 2\,\mathrm{GeV}/c, R = 0.4$. Pb + Pb, 2010, $\sqrt{s_{\mathrm{NN}}} = 2.76$ TeV.

all jets consisted only of hard particles, ρ value would be independent of $p_{\mathrm{T}}^{\mathrm{min}}$ up to the p_{T} of the softest jet constituent.

6.2.2 Background dependence on R

In case of proton collisions, jet reconstruction does not have to cope with such high level of background from soft particles as in case of heavy-ion collisions. Settings of the jet-finder algorithms used for proton collisions can afford using values of the distance parameter R up to $R \approx 1$. In Pb + Pb collisions, the tuning of R values is more complex.

If increasing R, higher contribution of background p_{T} in reconstructed jets might be expected. On the other hand, too low R might not be sufficient to allow reasonable reconstruction of jet candidates and further background calculations.

Recommended value for Pb + Pb collisions is $R = 0.4$ [34]. Following results compare outputs for other values.

Figure 6.11 shows how calculated values of ρ fluctuate with change of values of the radius R chosen for the jet algorithm which is used for the background density calculation. For each centrality bin, there are distributions of $\Delta\rho = \rho - \rho_{\mathrm{ref}}$ for different values of R, normalised by number of events and bin width. Values of ρ calculated for the standard setting: k_{t}, $R = 0.4$, $p_{\mathrm{T}}^{\mathrm{min}} = 0.15\,\mathrm{GeV}/c$ were used as the reference background.

Calculation of background density gives very similar results for the range of parameters $R = 0.2$–0.4. For $R = 0.1$, the calculated background values are significantly underestimated when compared to the reference values. In case of $R = 0.5, 0.6$, the difference distribution has larger tales but the most frequent background values do not differ from those of the reference background. The tales are in both cases wider at the right side, which indicates slight relative overestimation.

The width of $\Delta\rho$ distribution decreases with decreasing centrality according to the trend of the width of the ρ distribution itself. For this reason, calculation results do not differ much for jets in peripheral collisions (except for $R = 0.1$).

6.2.3 Background fluctuations

Understanding of fluctuations of the background transverse-momentum density is an important task required for correct event-by-event background subtraction. The fluctuations are expressed by the distribution of $\delta p_{\mathrm{T}} = p_{\mathrm{T,RC}} - \rho A_{\mathrm{RC}}$ [34] where $p_{\mathrm{T,RC}}$ is the sum of p_{T} of tracks inside a randomly oriented cone and $A_{\mathrm{RC}} = \pi R^2$ is the cone area.

Figures 6.12, 6.13, 6.14, 6.15, 6.16 show the background fluctuations for different settings of R and $p_{\mathrm{T}}^{\mathrm{min}}$. Each plot allows to compare results for different number of leading jets bypassed by the random cone. Distributions are normalised by number of events and bin width.

In case of 0 bypassed jets, generated random cones can overlap with any jet including the hardest one. In case of 1 bypassed jet, the random cones can overlap only with the second hardest jet and other softer jets. The probability of having a random cones with p_{T} significantly higher than background is lower. In case of 2 bypassed jets, the random cones can overlap with jets softer than two hardest

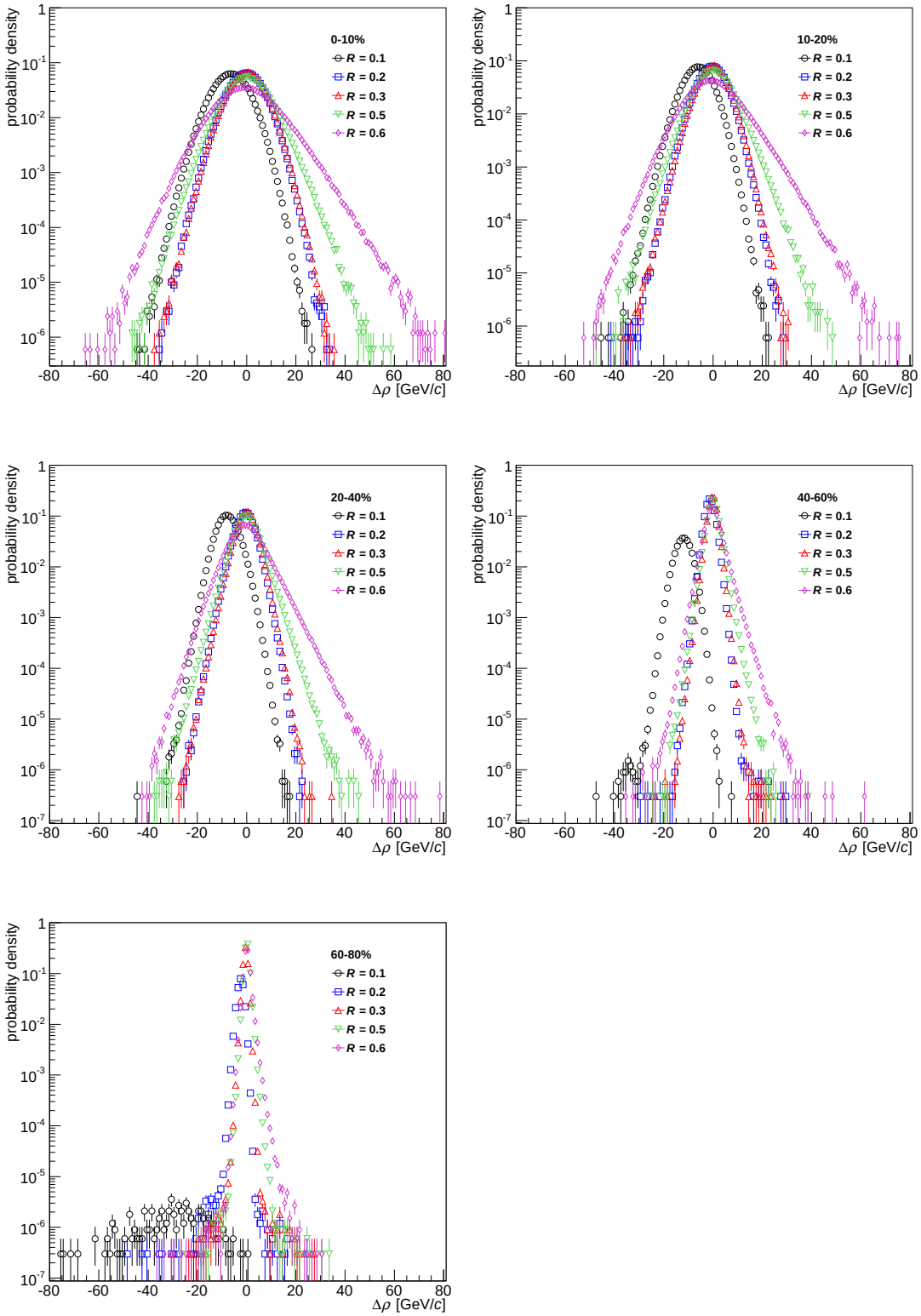

Figure 6.11: Dependence of the calculated background on the R parameter of the k_{t} jet finder. Each plot shows the distribution of $\Delta\rho$ for one centrality bin. Pb + Pb, 2010, $\sqrt{s_{\mathrm{NN}}} = 2.76$ TeV.

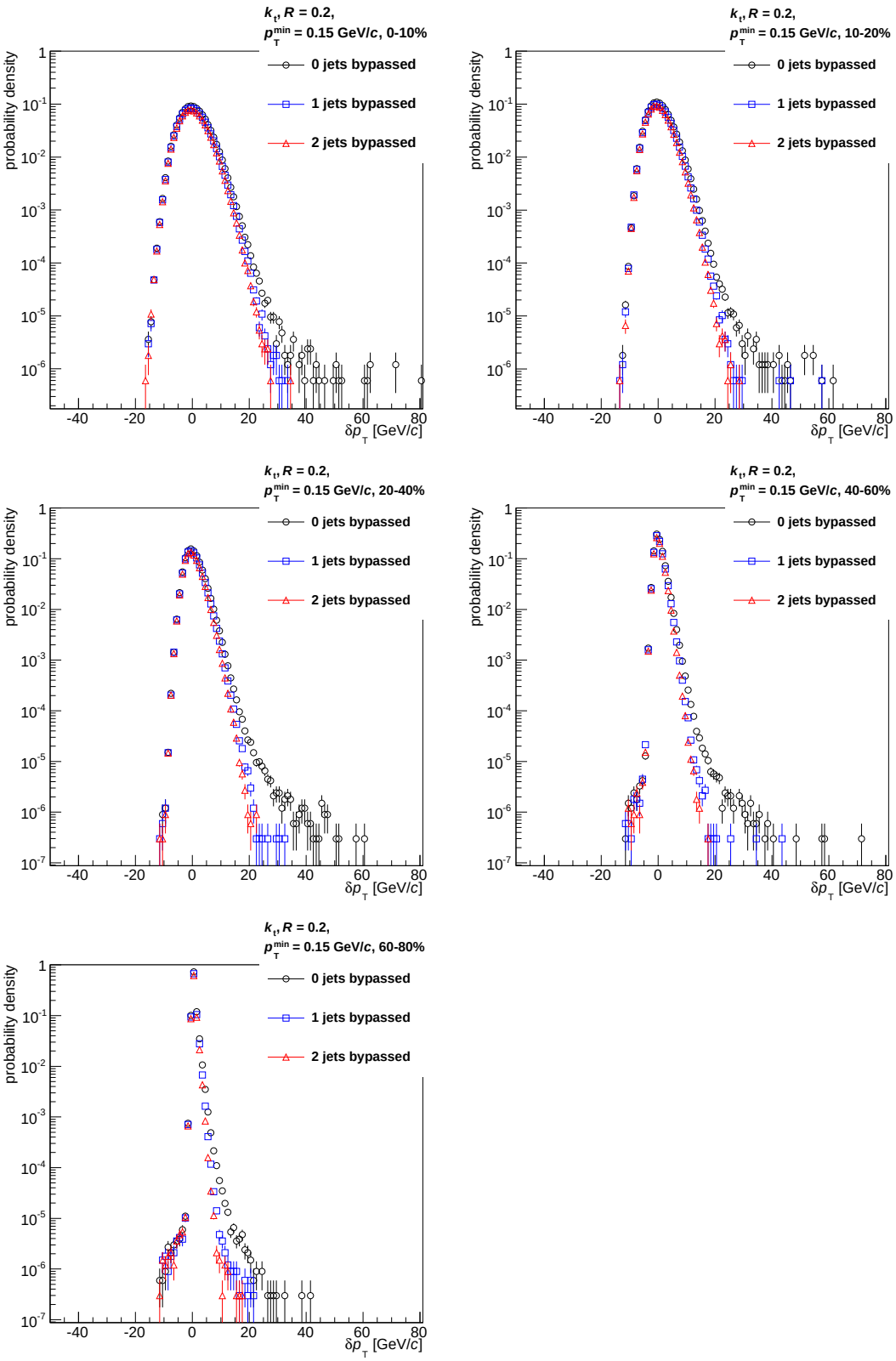

Figure 6.12: Fluctuations of background from random cones for jets reconstructed with k_t, $R = 0.2$, $p_T^{min} = 0.15$ GeV/c. Each plot shows the distribution of δp_T for one centrality bin. Pb + Pb, 2010, $\sqrt{s_{NN}} = 2.76$ TeV.

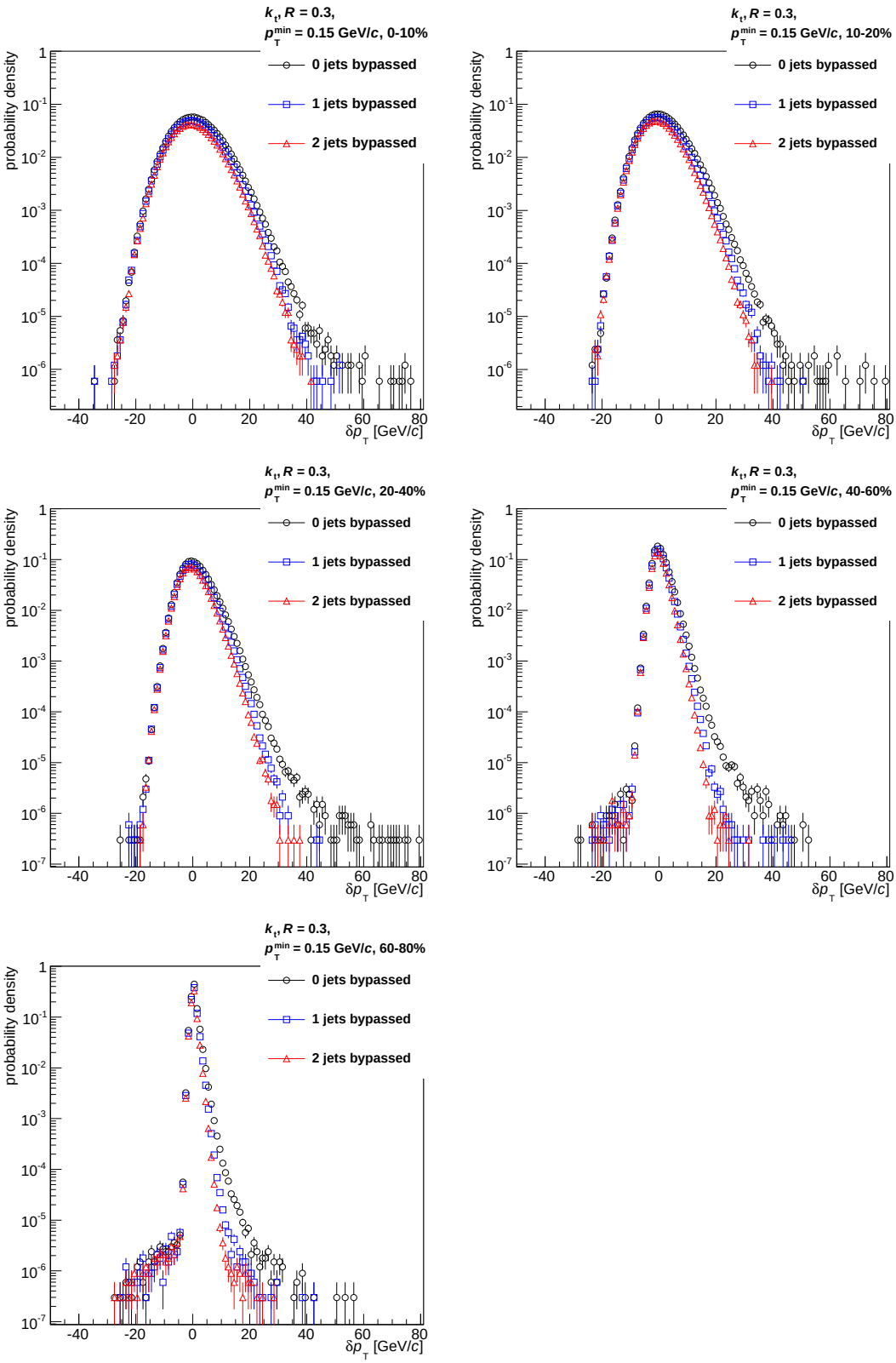

Figure 6.13: Fluctuations of background from random cones for jets reconstructed with k_t, $R = 0.3$, $p_T^{min} = 0.15\,\mathrm{GeV}/c$. Each plot shows the distribution of δp_T for one centrality bin. Pb + Pb, 2010, $\sqrt{s_{NN}} = 2.76\,\mathrm{TeV}$.

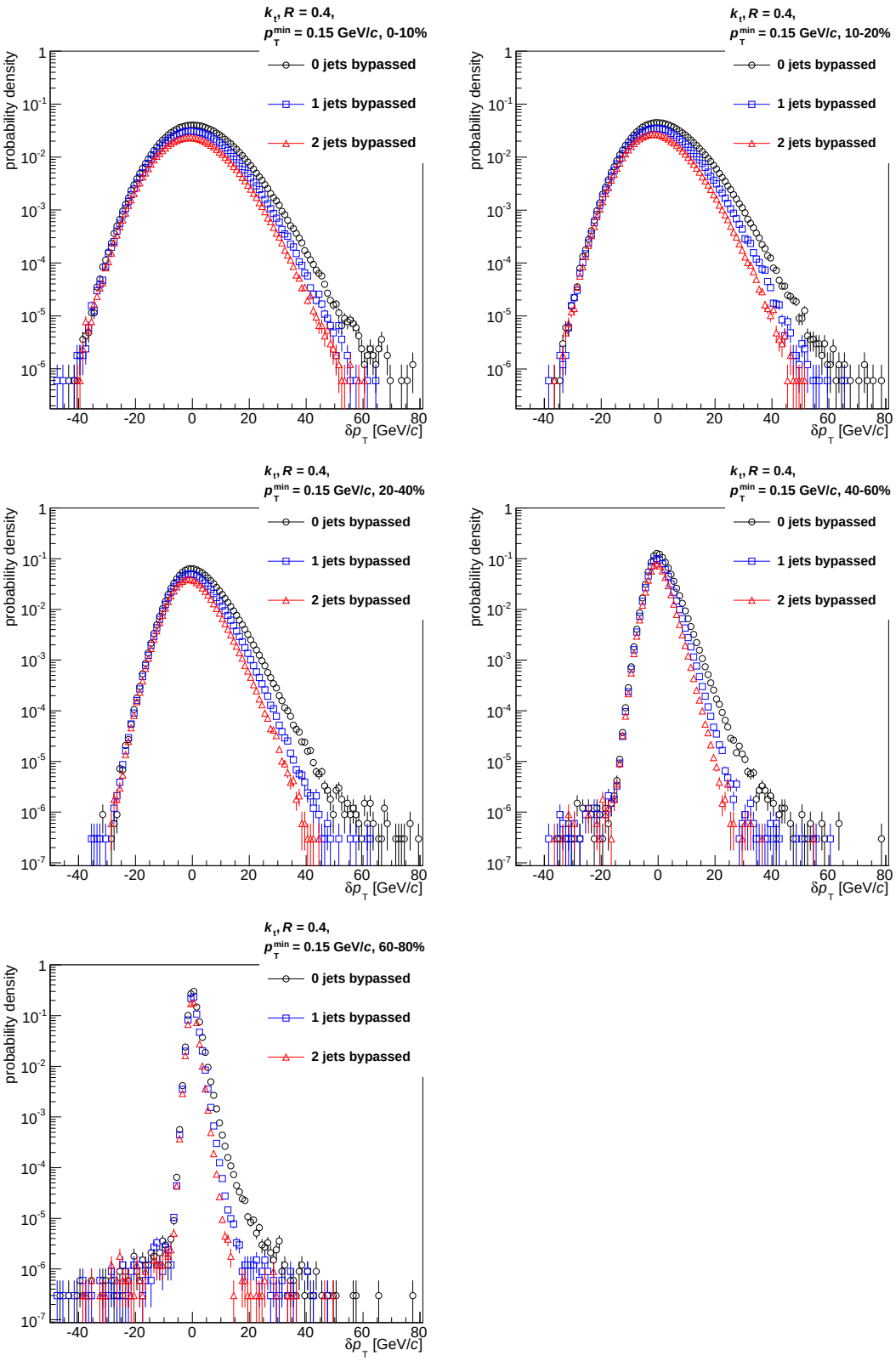

Figure 6.14: Fluctuations of background from random cones for jets reconstructed with k_t, $R = 0.4$, $p_T^{min} = 0.15\,\mathrm{GeV}/c$. Each plot shows the distribution of δp_T for one centrality bin. Pb + Pb, 2010, $\sqrt{s_{NN}} = 2.76\,\mathrm{TeV}$.

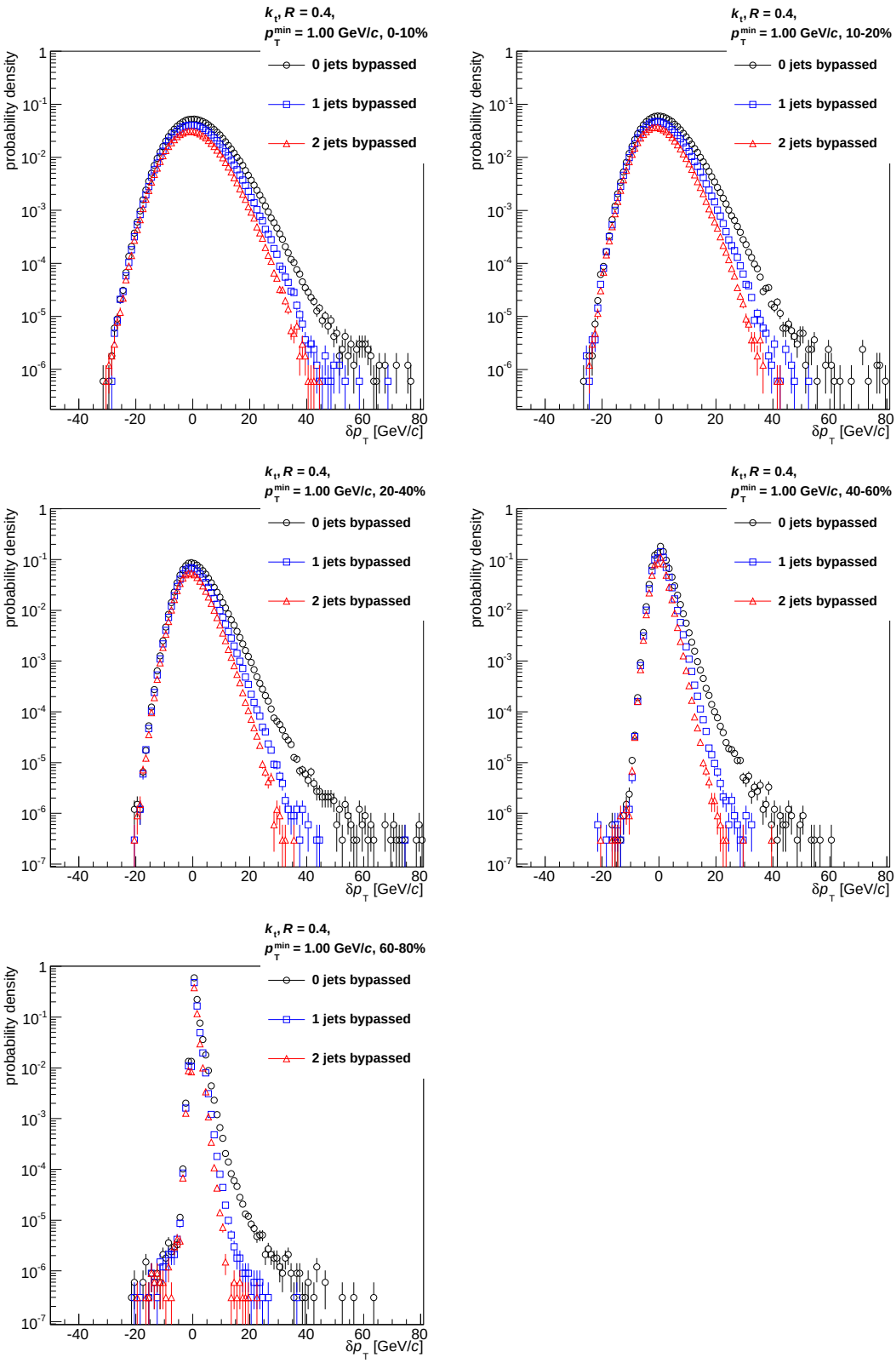

Figure 6.15: Fluctuations of background from random cones for jets reconstructed with k_t, $R = 0.4$, $p_T^{min} = 1\,\mathrm{GeV}/c$. Each plot shows the distribution of δp_T for one centrality bin. Pb + Pb, 2010, $\sqrt{s_{NN}} = 2.76$ TeV.

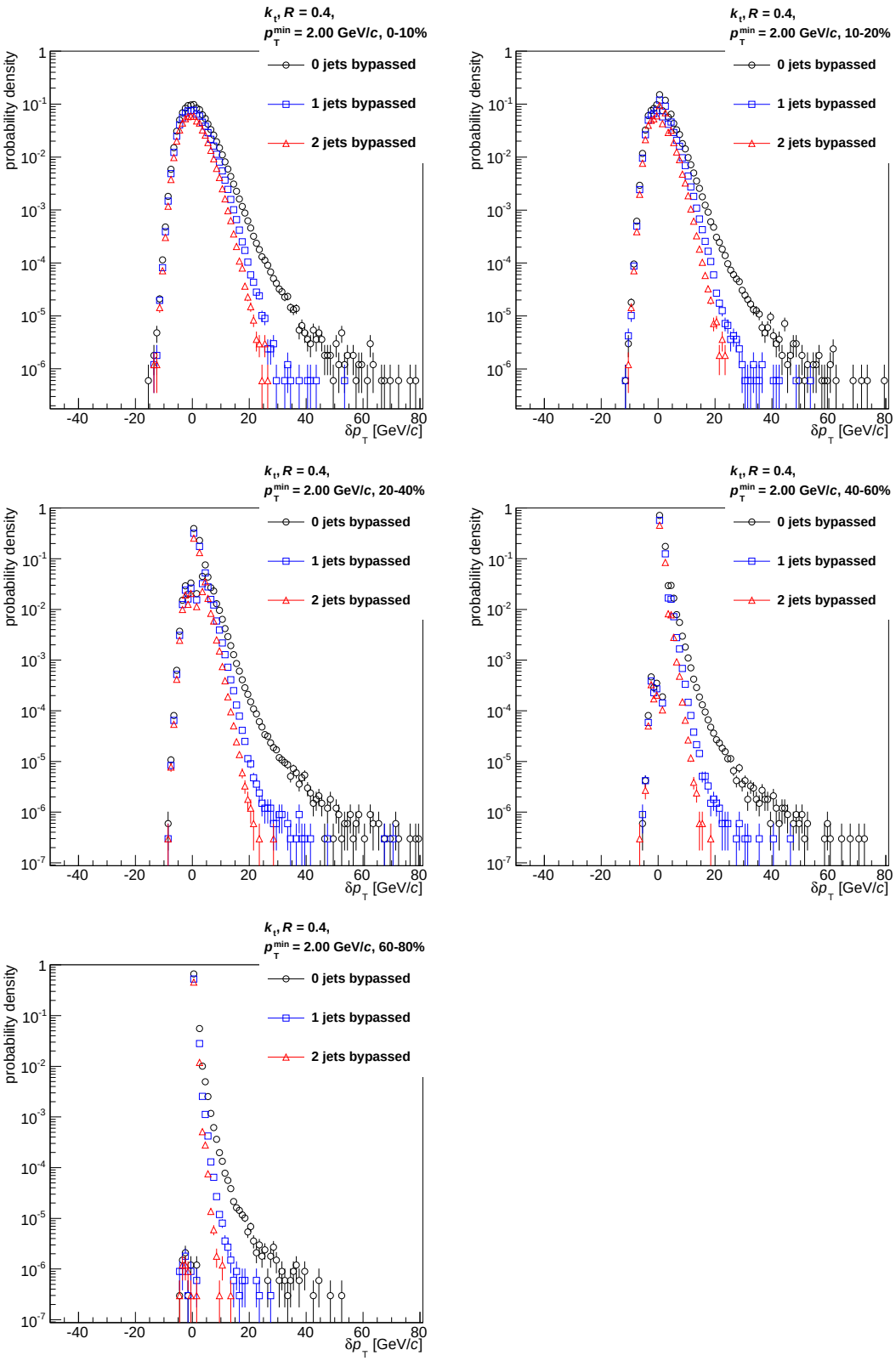

Figure 6.16: Fluctuations of background from random cones for jets reconstructed with k_t, $R = 0.4$, $p_\mathrm{T}^\mathrm{min} = 2\,\mathrm{GeV}/c$. Each plot shows the distribution of δp_T for one centrality bin. Pb + Pb, 2010, $\sqrt{s_\mathrm{NN}} = 2.76$ TeV.

jets. Therefore random cones having p_{T} close to the background value are even more probable than in previous cases. This has a direct effect on the width of tales in δp_{T} distribution for positive δp_{T} (i.e. positive deviation of p_{T} inside a random cone).

The width of the δp_{T} distribution scales with the square root of the number of tracks inside the cone [34]. Increasing the radius R increases the cone area as well which results in larger background fluctuations, i.e. wider δp_{T} distribution. Increasing the $p_{\mathrm{T}}^{\mathrm{min}}$ threshold reduces the impact of the soft-tracks contribution to the p_{T} of reconstructed jets which is manifested in smaller background fluctuations, i.e. narrower δp_{T} distribution.

The asymmetric shape of δp_{T} distribution is well described by a Γ-distribution in case of uncorrelated particle emission. Correlated fluctuations (e.g from initial anisotropy of collision) should be manifested in reduction of distribution width [34].

6.3 Jet analysis

The charged jet candidates reconstructed with the anti-k_{t} algorithm were used as "signal" jets for the jet analysis. Background subtraction was done with ρ values taken from background calculations for jets reconstructed with k_{t}, $R = 0.4$ and corresponding $p_{\mathrm{T}}^{\mathrm{min}}$. All p_{T} spectra were normalised by number of events, bin width and the width of η-range, i.e. 1.8.

6.3.1 Directions of jets

Spectra of jets in pseudorapidity and azimuth allow to display how jets are produced in different angles with respect to the collision axis. Spectra are presented for jet candidates reconstructed with the anti-k_{t} algorithm and after vector subtraction.

Pseudorapidity spectra

I created two types of reconstructed-jet-pseudorapidity spectra. The first type enables comparison of spectra for different centrality bins, the second type provides comparison of spectra in different p_{T} ranges, as defined in Table 5.9.

Plots of η spectra in centrality bins are in Figures 6.17, 6.18, 6.19, spectra in p_{T} bins are in Figures 6.20, 6.21, 6.22. Figures for chosen values of R are presented. Each figure contains three plots for different values of $p_{\mathrm{T}}^{\mathrm{min}}$. Spectra in centrality bins were normalised by number of events and by bin width, spectra in p_{T} bins were normalised by their integrals (number of jets) and by bin width.

Vector subtraction may change directions of jets. That is why there are some jets outside the tracking range $|\eta| \leq 0.9$.

There is an excess of reconstructed jets inclined closer to the collision axis. That is caused by limited acceptance of tracking detectors [9]. When comparing spectra for different $p_{\mathrm{T}}^{\mathrm{min}}$ and p_{T}, the effect seems to be stronger when soft particles are included in the jet reconstruction or when only soft jets are taken into account.

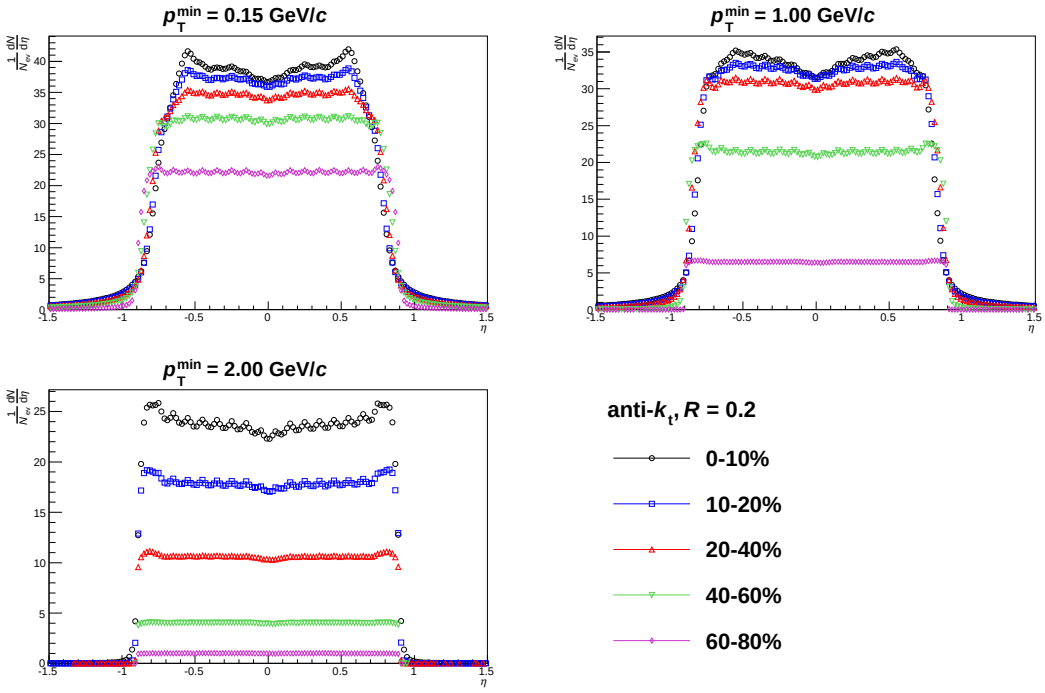

Figure 6.17: Pseudorapidity spectra of jets, in centrality bins. Pb + Pb, 2010, $\sqrt{s_{\mathrm{NN}}} = 2.76$ TeV, anti-k_{t}, $R = 0.2$.

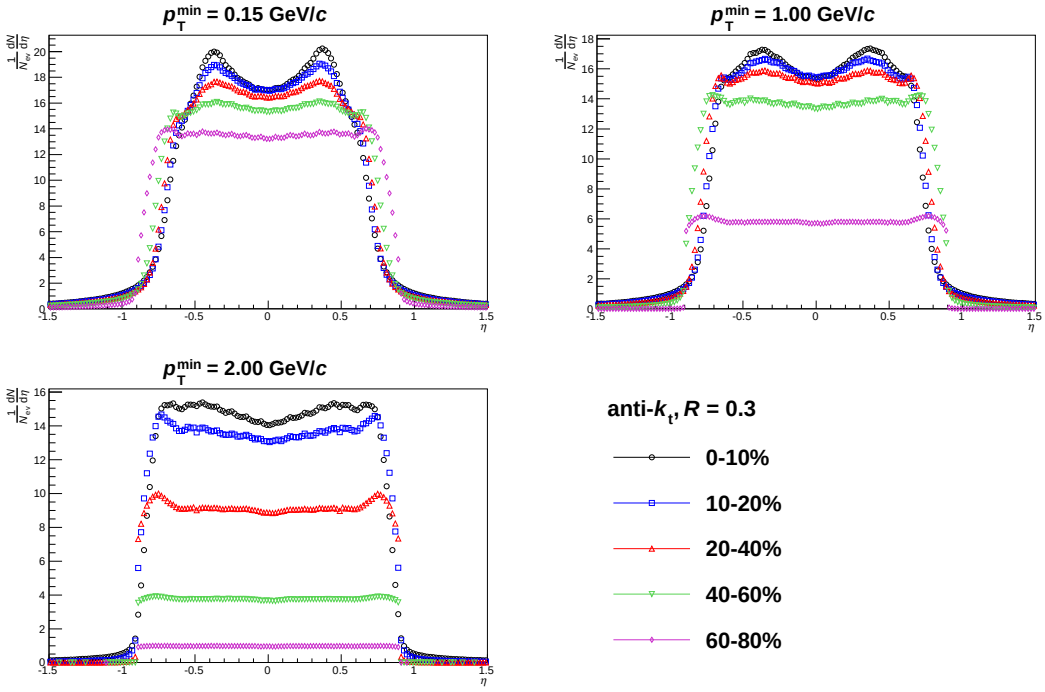

Figure 6.18: Pseudorapidity spectra of jets, in centrality bins. Pb + Pb, 2010, $\sqrt{s_{\mathrm{NN}}} = 2.76$ TeV, anti-k_{t}, $R = 0.3$.

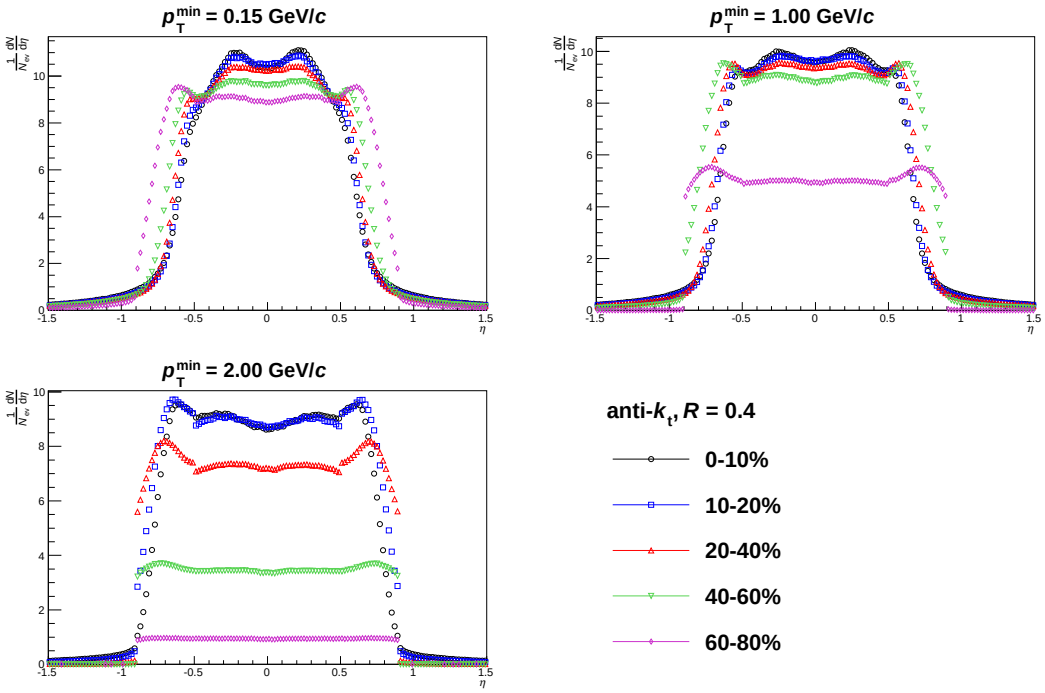

Figure 6.19: Pseudorapidity spectra of jets, in centrality bins. Pb + Pb, 2010, $\sqrt{s_{\mathrm{NN}}} = 2.76$ TeV, anti-k_{t}, $R = 0.4$.

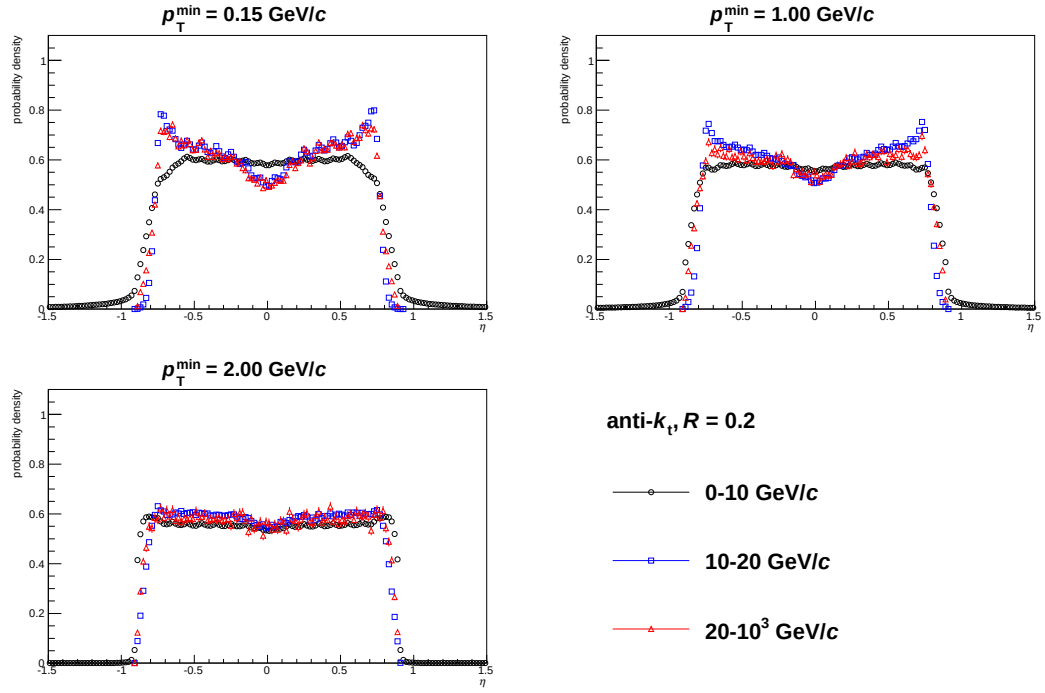

Figure 6.20: Pseudorapidity spectra of jets, in p_{T} bins. Pb + Pb, 2010, $\sqrt{s_{\mathrm{NN}}} = 2.76$ TeV, anti-k_{t}, $R = 0.2$, centrality 0–80 %.

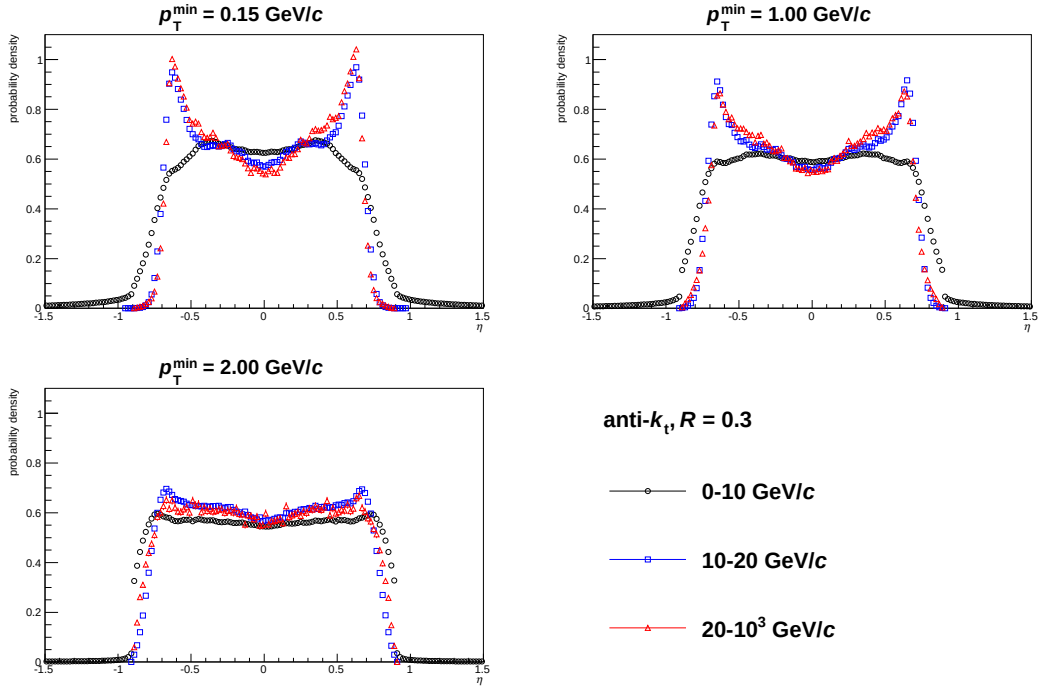

Figure 6.21: Pseudorapidity spectra of jets, in p_{T} bins. Pb + Pb, 2010, $\sqrt{s_{\mathrm{NN}}} = 2.76$ TeV, anti-k_{t}, $R = 0.3$, centrality 0–80 %.

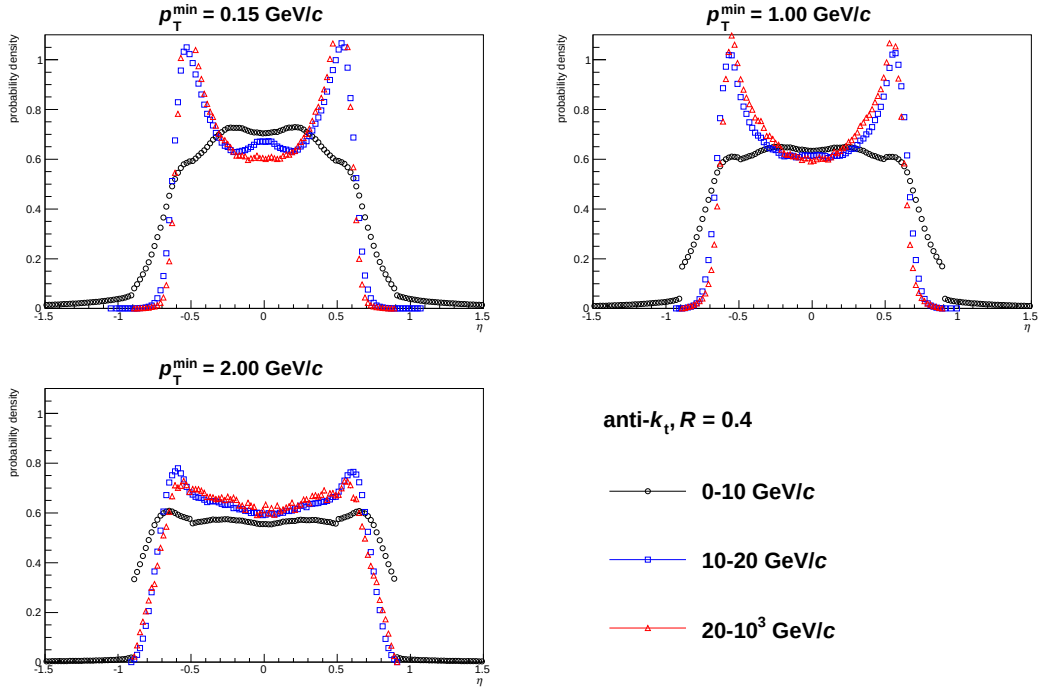

Figure 6.22: Pseudorapidity spectra of jets, in p_{T} bins. Pb + Pb, 2010, $\sqrt{s_{\mathrm{NN}}} = 2.76$ TeV, anti-k_{t}, $R = 0.4$, centrality 0–80 %.

Azimuth spectra

Figure 6.23 shows spectra of reconstructed jets in azimuth angle ϕ for $R = 0.4$ and all three values of $p_{\mathrm{T}}^{\mathrm{min}}$. Spectra were normalised by total number of events and bin width.

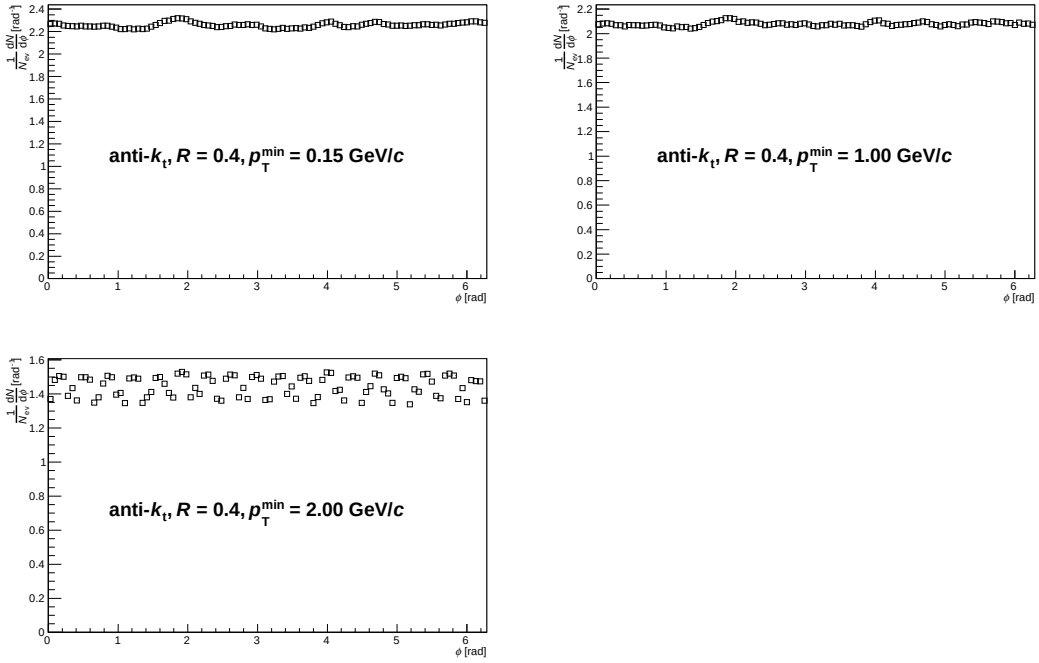

Figure 6.23: Azimuth spectra of jets. Pb + Pb, 2010, $\sqrt{s_{\mathrm{NN}}} = 2.76$ TeV, anti-k_{t}, $R = 0.4$.

Distribution of jets in azimuth seems to be uniform as expected. Visible fluctuations appear only for the highest $p_{\mathrm{T}}^{\mathrm{min}}$ value.

6.3.2 Comparison of different jet algorithms

The jet candidates were reconstructed with all jet algorithms listed above (see Table 5.11 for details) to allow basic comparison of results of various algorithms.

Number of jets per event

Figures 6.24, 6.25, 6.26 compare distributions of number N_{jets} of reconstructed jet candidates per event for all algorithms. Each figure contains plots for all centrality bins. Open symbols (labelled as "B0") correspond to the jet candidates before background subtraction, closed symbols (labelled as "B1") correspond to the candidates after (scalar) background subtraction. Distributions are normalised by number of events and bin width.

Number of jets is significantly reduced by subtraction of background. The impact of subtraction decreases with increasing $p_{\mathrm{T}}^{\mathrm{min}}$. Spectra for the UA1 algorithm have a significantly different appearance from other algorithms because of the maximal number of jets per event (see Subsection 5.4.3). In terms of distribution of number of reconstructed jets before or after subtraction, algorithms k_{t}

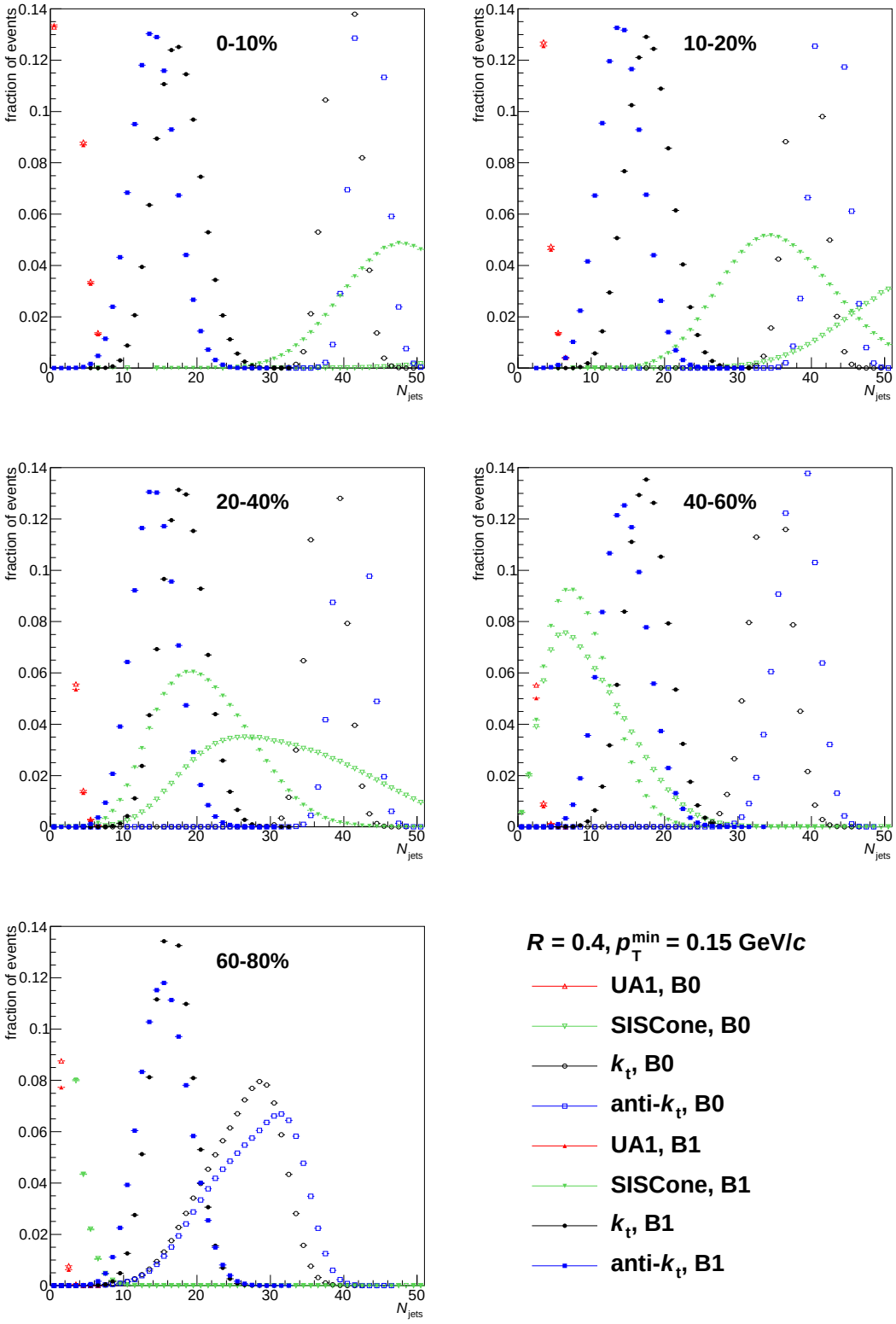

Figure 6.24: Number of jets per event for different algorithms. Pb + Pb, 2010, $\sqrt{s_{\mathrm{NN}}} = 2.76$ TeV, $R = 0.4$, $p_{\mathrm{T}}^{\mathrm{min}} = 0.15\,\mathrm{GeV}/c$, B0, B1.

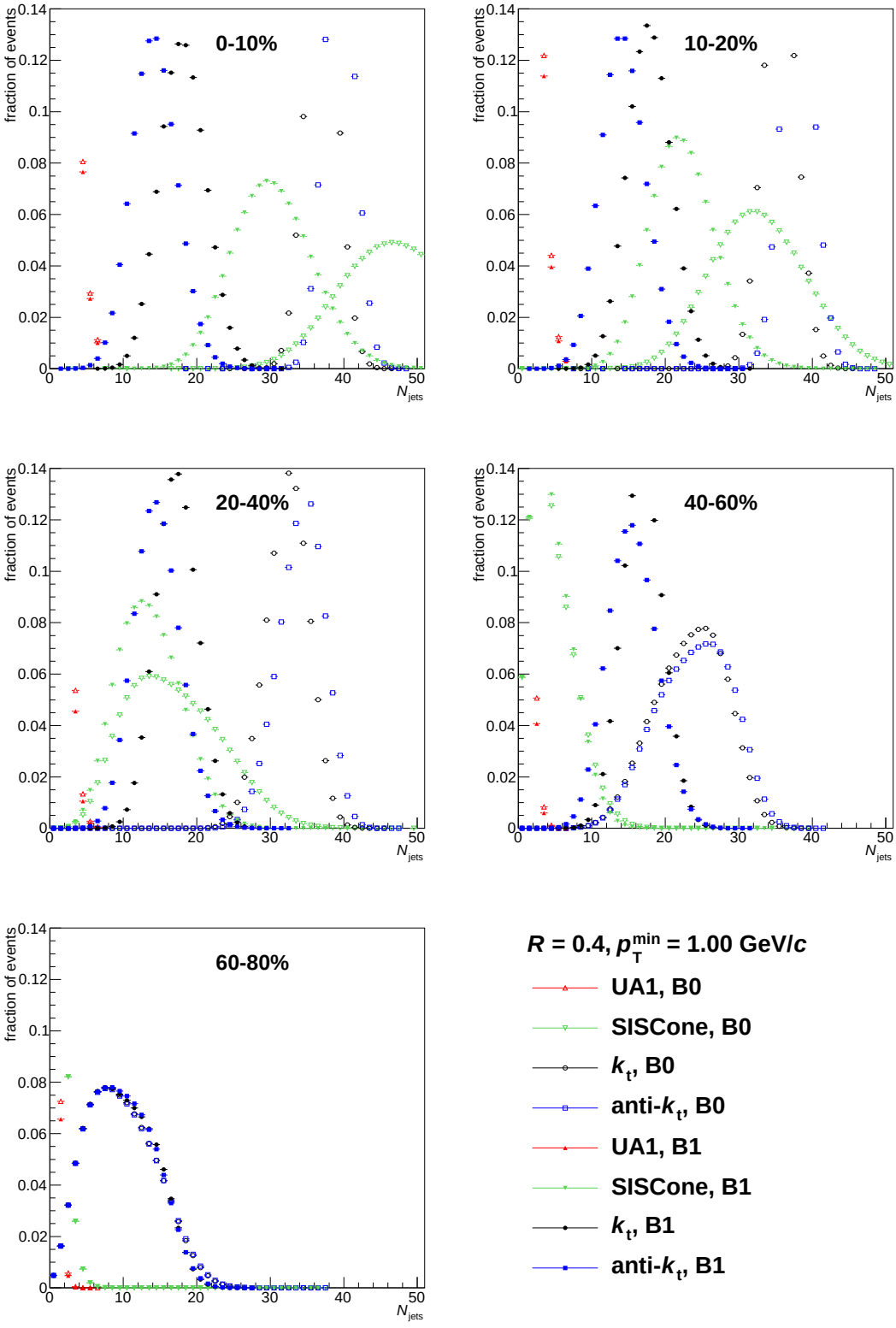

Figure 6.25: Number of jets per event for different algorithms. Pb + Pb, 2010, $\sqrt{s_{\mathrm{NN}}} = 2.76$ TeV, $R = 0.4$, $p_{\mathrm{T}}^{\mathrm{min}} = 1$ GeV/c, B0, B1.

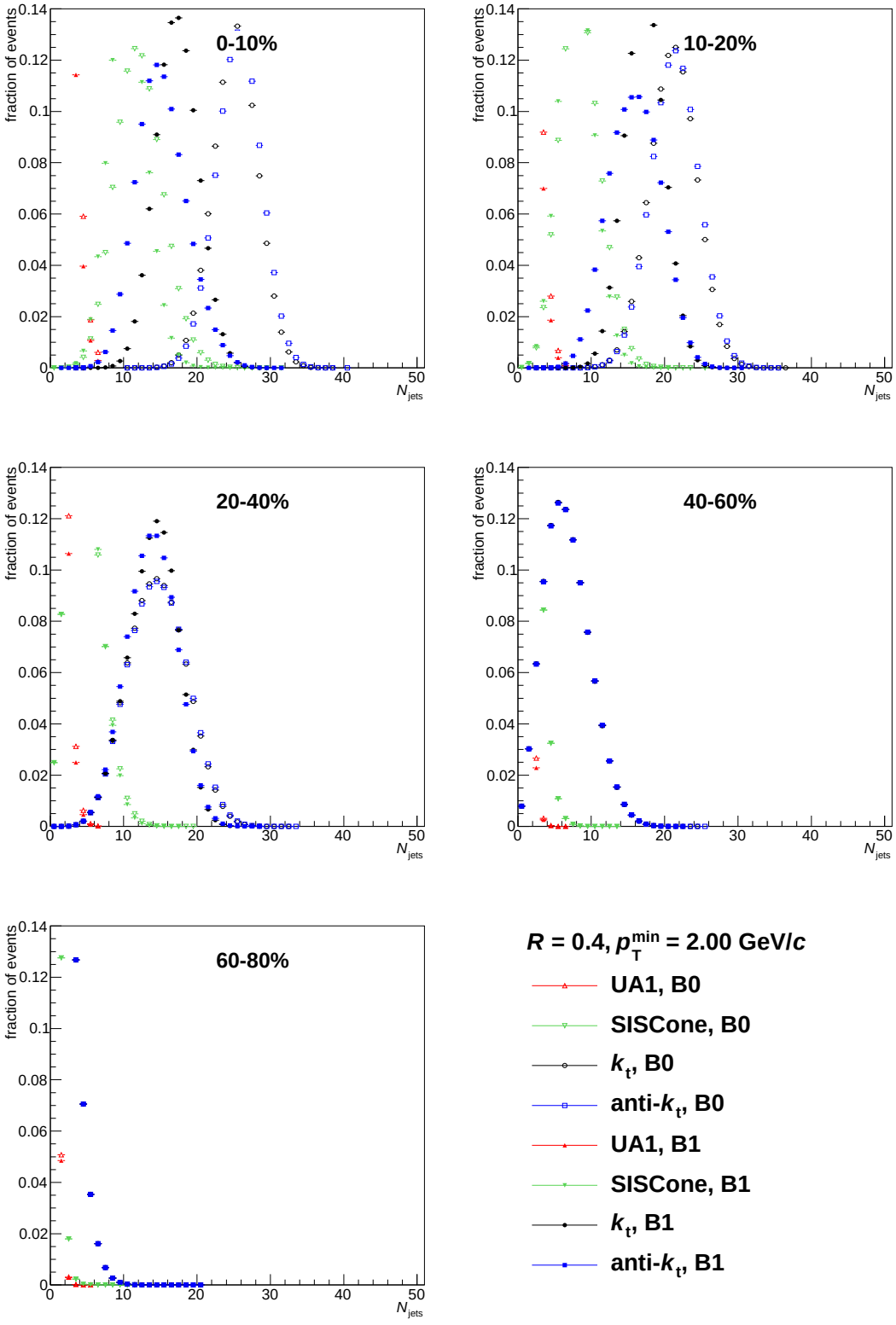

Figure 6.26: Number of jets per event for different algorithms. Pb + Pb, 2010, $\sqrt{s_{\mathrm{NN}}} = 2.76$ TeV, $R = 0.4$, $p_{\mathrm{T}}^{\mathrm{min}} = 2\,\mathrm{GeV}/c$, B0, B1.

and anti-k_t manifest similar behaviour; k_t algorithm finds slightly more jets than anti-k_t.

Jet p_T spectra

Following figures allow to compare uncorrected p_T spectra of jet candidates reconstructed with all algorithms for different values of p_T^{min}. Plots are presented in the same scheme as the plots of number of jets per event. Raw spectra before background subtraction are presented in Figures 6.27, 6.28, 6.29, spectra after (scalar) background subtraction are presented in Figures 6.30, 6.31, 6.32.

Shapes of spectra differ the most in the more central collisions and lower p_T^{min}, i.e. in spectra with the highest contribution of soft background (see the following Subsection 6.3.3). Increasing p_T^{min} or lowering centrality reduces this effect which results in more similar spectra. The higher is p_T^{min}, the weaker is dependence of the p_T-spectrum shape on the jet algorithm. Both raw and subtracted spectra for all algorithms quite overlap for all centralities in case of the highest p_T^{min}. The spectra of peripheral collisions are quite similar even for lower p_T^{min}.

Following parts of this chapter focus on the analysis of "signal"-jet candidates, reconstructed with the anti-k_t algorithm.

6.3.3 Influence of background on p_T spectra

Figures 6.33, 6.34, 6.35 show raw p_T spectra compared to the spectra after subtraction for radii $R = 0.2, 0.3, 0.4$ respectively. Raw spectra are labelled as "B0", spectra after scalar subtraction are labelled as "B1" and spectra after vector subtraction are labelled as "B2". The difference of raw and subtracted spectra, labelled as "B0 − B2", is plotted as well to show isolated contribution of the background spectrum. Each figure shows pairs of plots for the most central collisions (on the left) and for the most peripheral collisions (on the right), arranged in three rows for all values of p_T^{min} respectively.

Both methods of subtracting background contribution to the jet p_T result in (almost) identical p_T spectra.

There is an important contribution of background to the jet p_T. The relative impact of subtraction on spectra is not so large for low p_T because the number of soft jets vanished due to subtraction is compensated by the number of less soft jets with p_T reduced by the subtraction. In case of the most central collisions for $p_T \gtrsim 20$ GeV/c, the correction of p_T spectrum, applied by subtracting background p_T contribution, is of the same order as the raw (unsubtracted) spectrum. In case of the most peripheral collisions, the correction is lower than the final spectrum after subtraction. Increasing the p_T^{min} value progressively reduces the background contribution. The highest threshold $p_T^{min} = 2$ GeV/c provides a significant reduction of background even for the most central collisions.

6.3.4 Influence of R on p_T spectra

Figures 6.36, 6.37, 6.38 show how p_T spectra of reconstructed jet candidates after vector subtraction of background depend on the value of the radius R. Each figure includes plots for centrality bins for one value of p_T^{min}, each plot enables

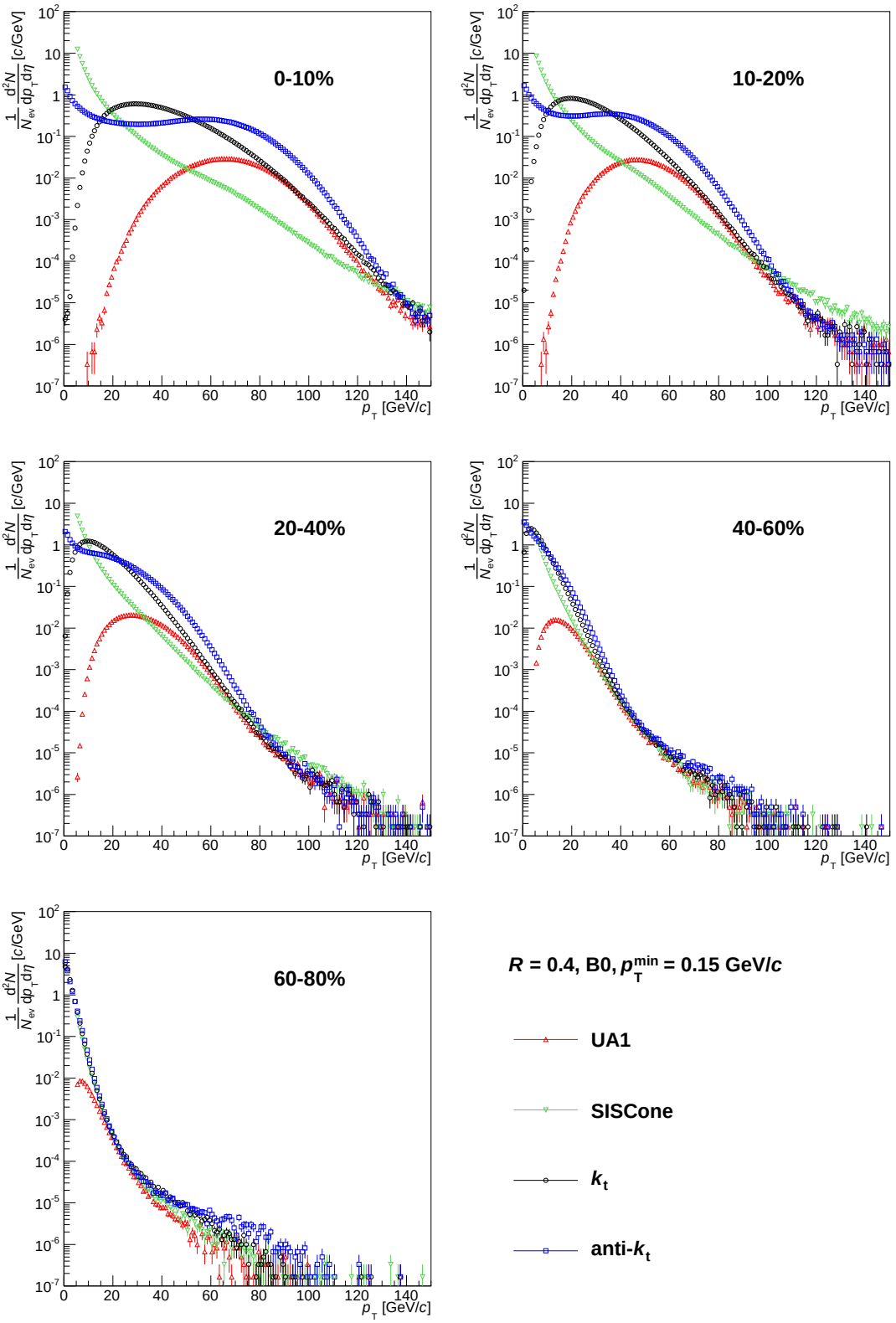

Figure 6.27: Comparison of uncorrected charged-jet-candidate inclusive p_{T} spectra before background subtraction, reconstructed with different jet algorithms. Pb + Pb, 2010, $\sqrt{s_{\mathrm{NN}}} = 2.76$ TeV, $R = 0.4$, $p_{\mathrm{T}}^{\mathrm{min}} = 0.15$ GeV/c.

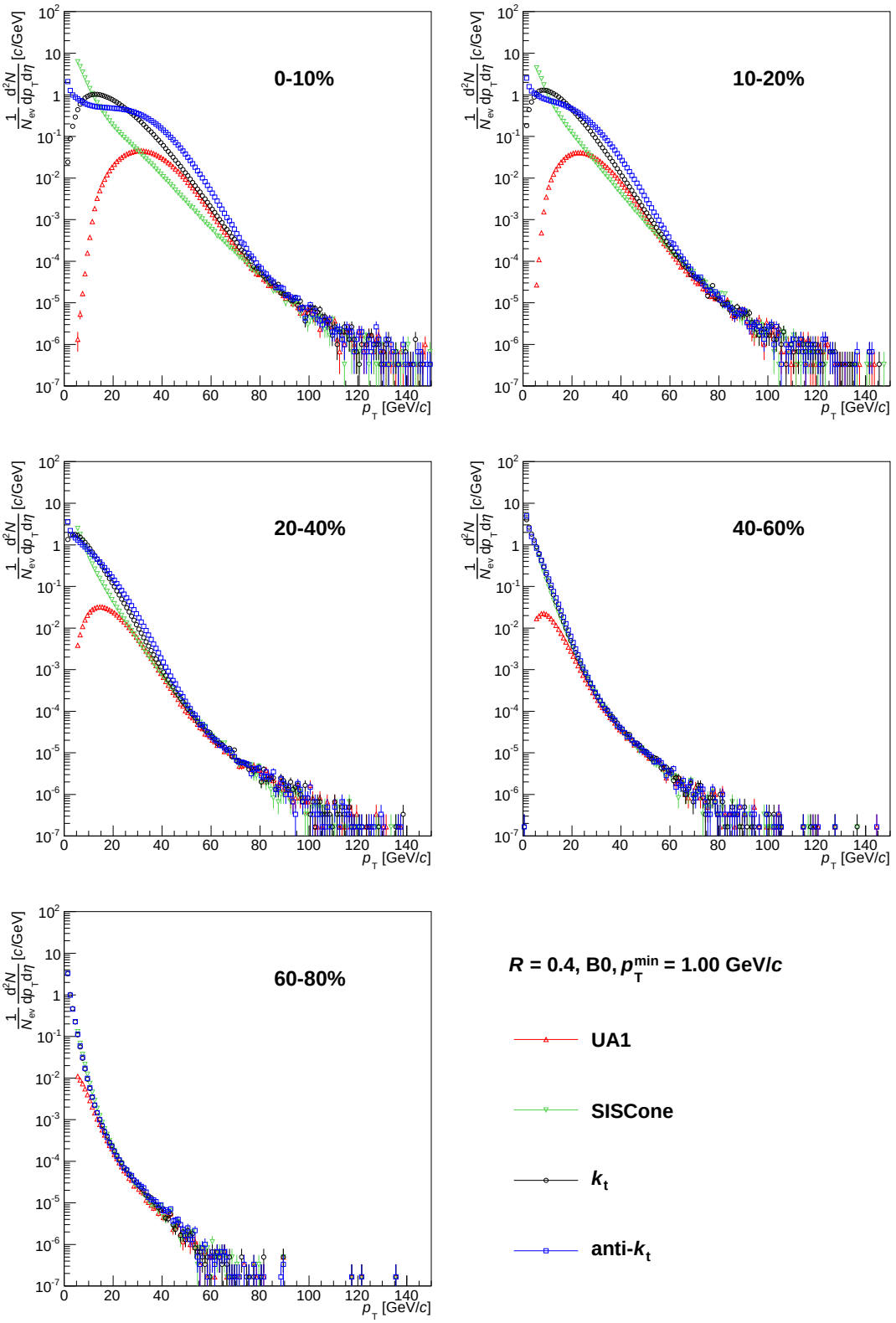

Figure 6.28: Comparison of uncorrected charged-jet-candidate inclusive p_{T} spectra before background subtraction, reconstructed with different jet algorithms. Pb + Pb, 2010, $\sqrt{s_{\mathrm{NN}}} = 2.76$ TeV, $R = 0.4$, $p_{\mathrm{T}}^{\mathrm{min}} = 1$ GeV/c.

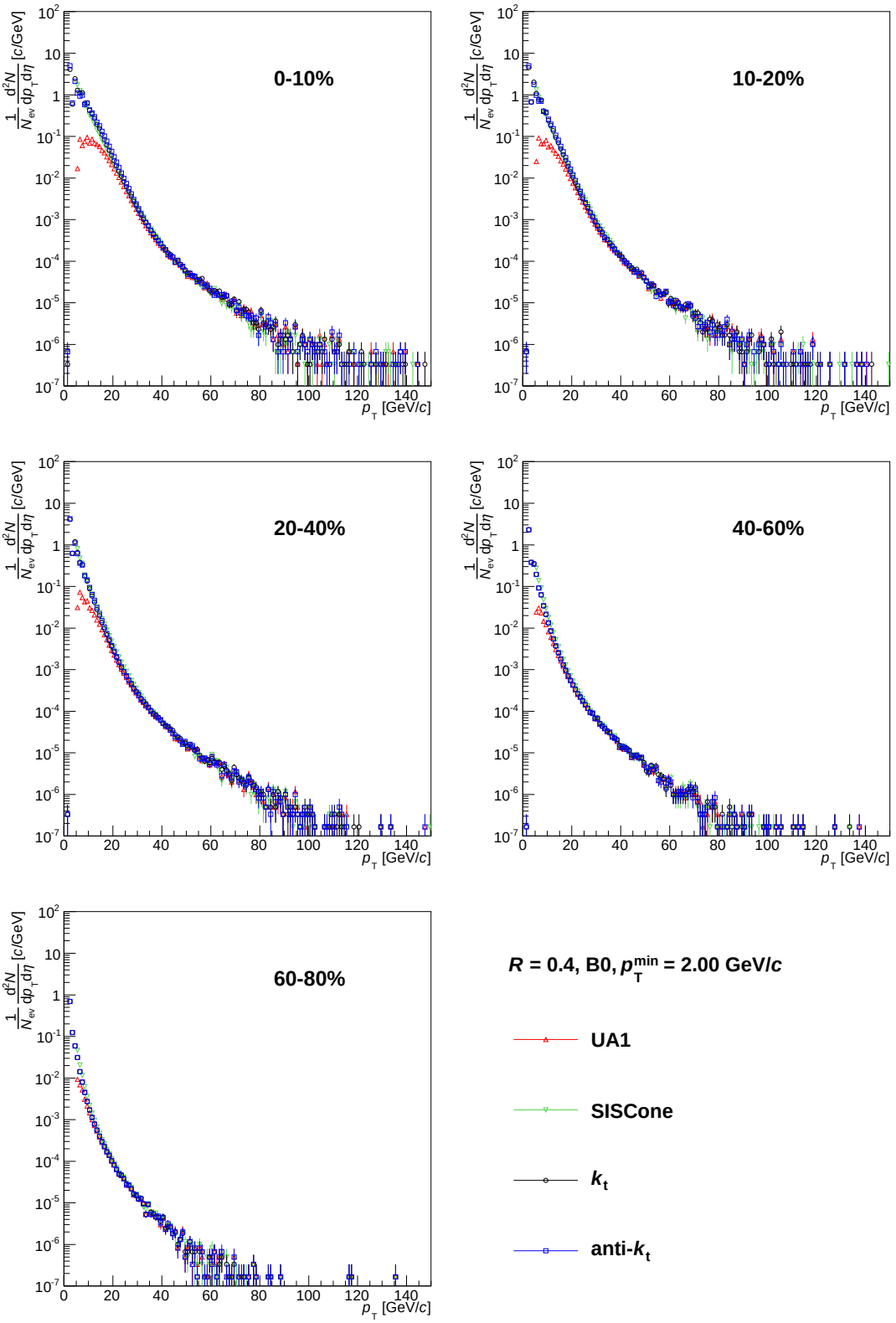

Figure 6.29: Comparison of uncorrected charged-jet-candidate inclusive p_{T} spectra before background subtraction, reconstructed with different jet algorithms. Pb + Pb, 2010, $\sqrt{s_{\mathrm{NN}}} = 2.76$ TeV, $R = 0.4$, $p_{\mathrm{T}}^{\mathrm{min}} = 2$ GeV/c.

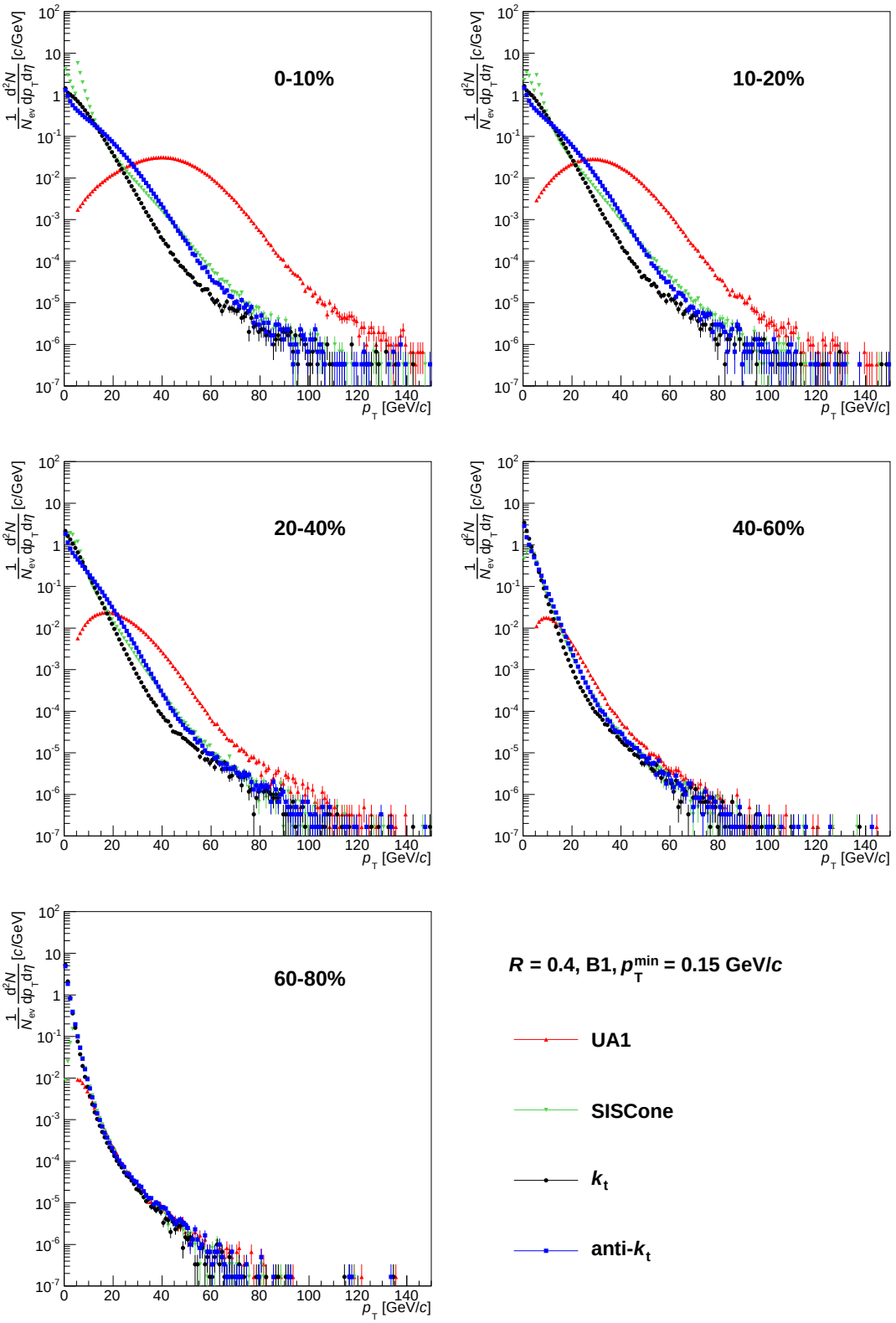

Figure 6.30: Comparison of uncorrected charged-jet-candidate inclusive p_{T} spectra after background subtraction, reconstructed with different jet algorithms. Pb + Pb, 2010, $\sqrt{s_{\mathrm{NN}}} = 2.76$ TeV, $R = 0.4$, $p_{\mathrm{T}}^{\mathrm{min}} = 0.15$ GeV/c.

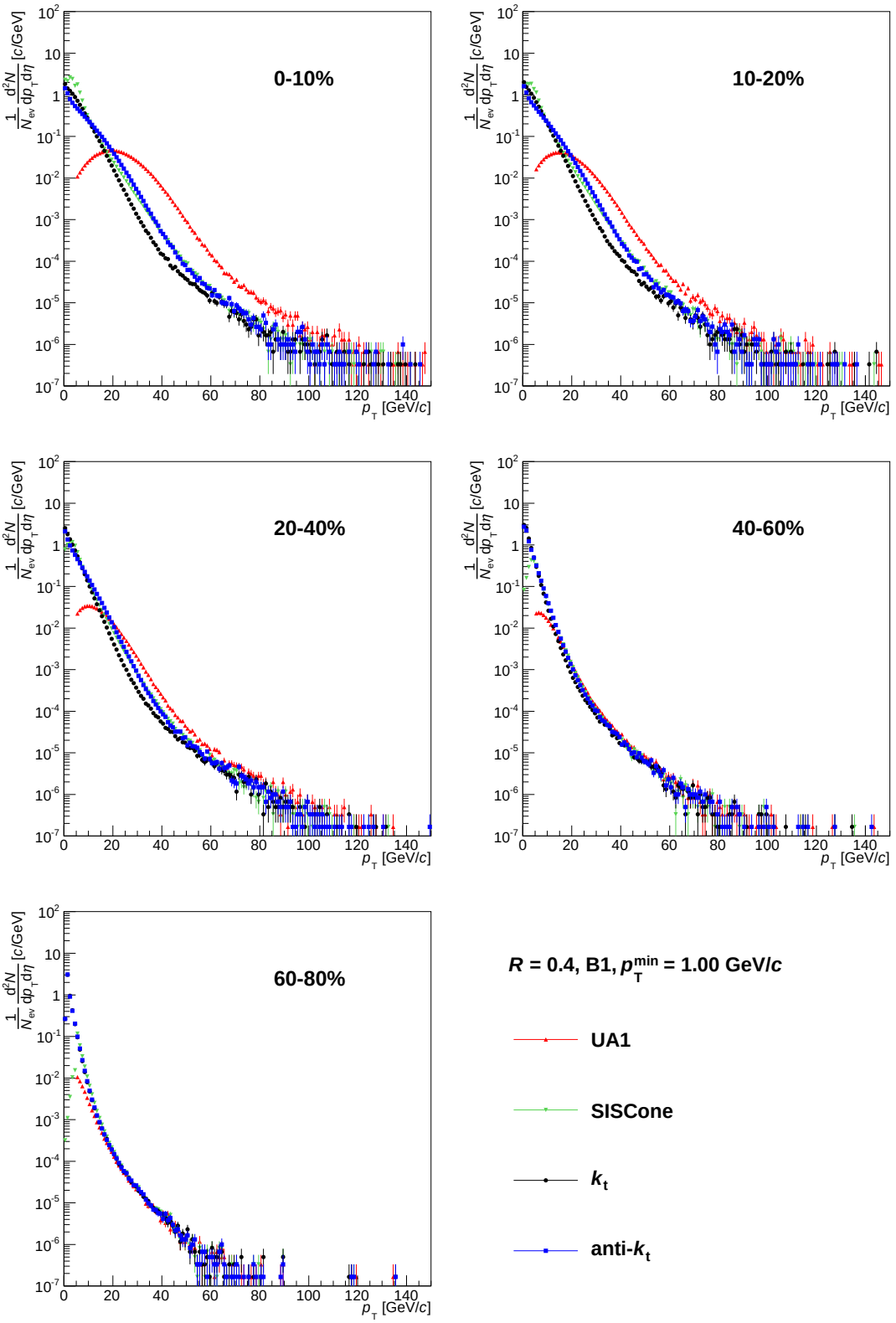

Figure 6.31: Comparison of uncorrected charged-jet-candidate inclusive p_{T} spectra after background subtraction, reconstructed with different jet algorithms. Pb + Pb, 2010, $\sqrt{s_{\mathrm{NN}}} = 2.76$ TeV, $R = 0.4$, $p_{\mathrm{T}}^{\mathrm{min}} = 1$ GeV/c.

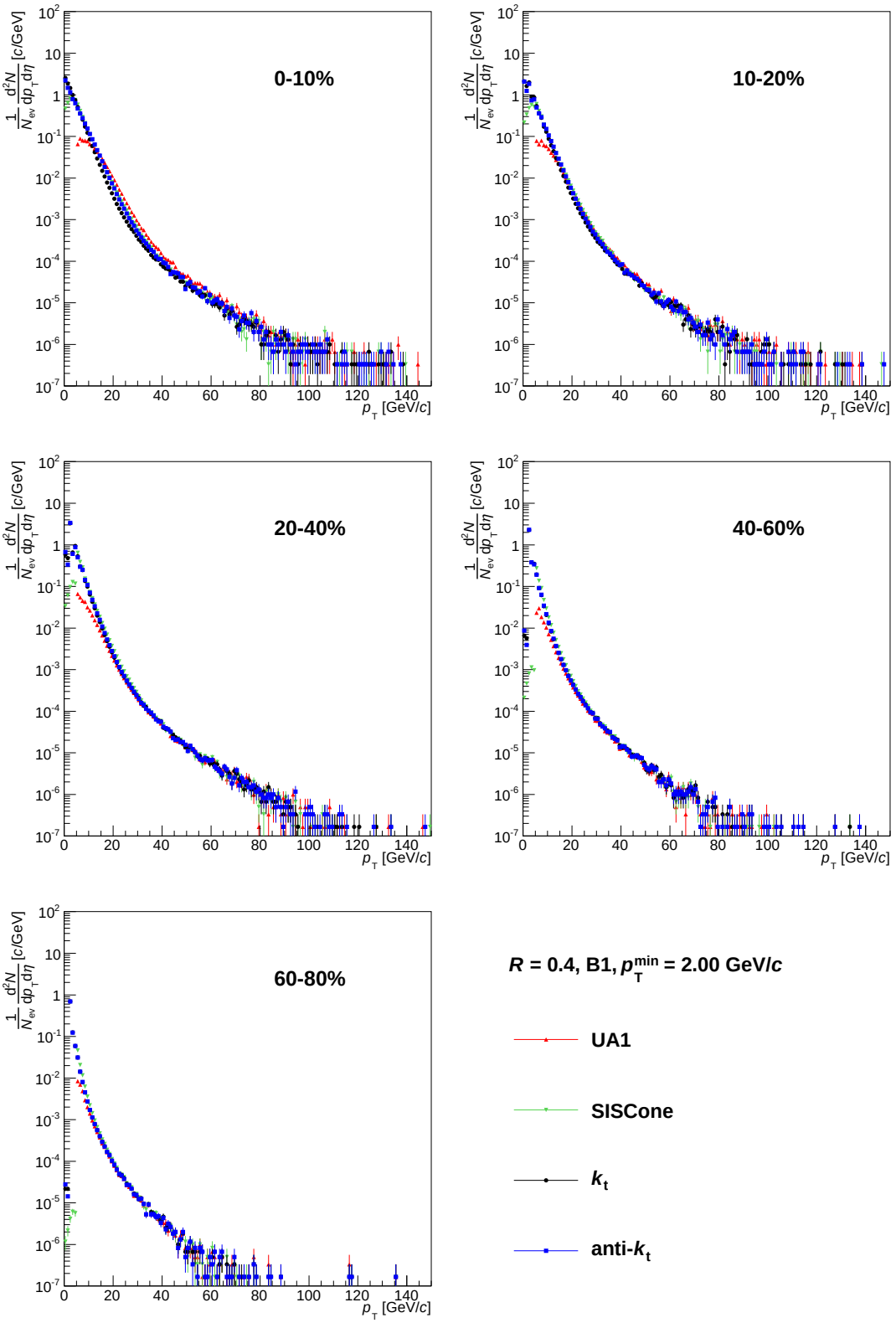

Figure 6.32: Comparison of uncorrected charged-jet-candidate inclusive p_{T} spectra after background subtraction, reconstructed with different jet algorithms. Pb + Pb, 2010, $\sqrt{s_{\mathrm{NN}}} = 2.76$ TeV, $R = 0.4$, $p_{\mathrm{T}}^{\mathrm{min}} = 2\,\mathrm{GeV}/c$.

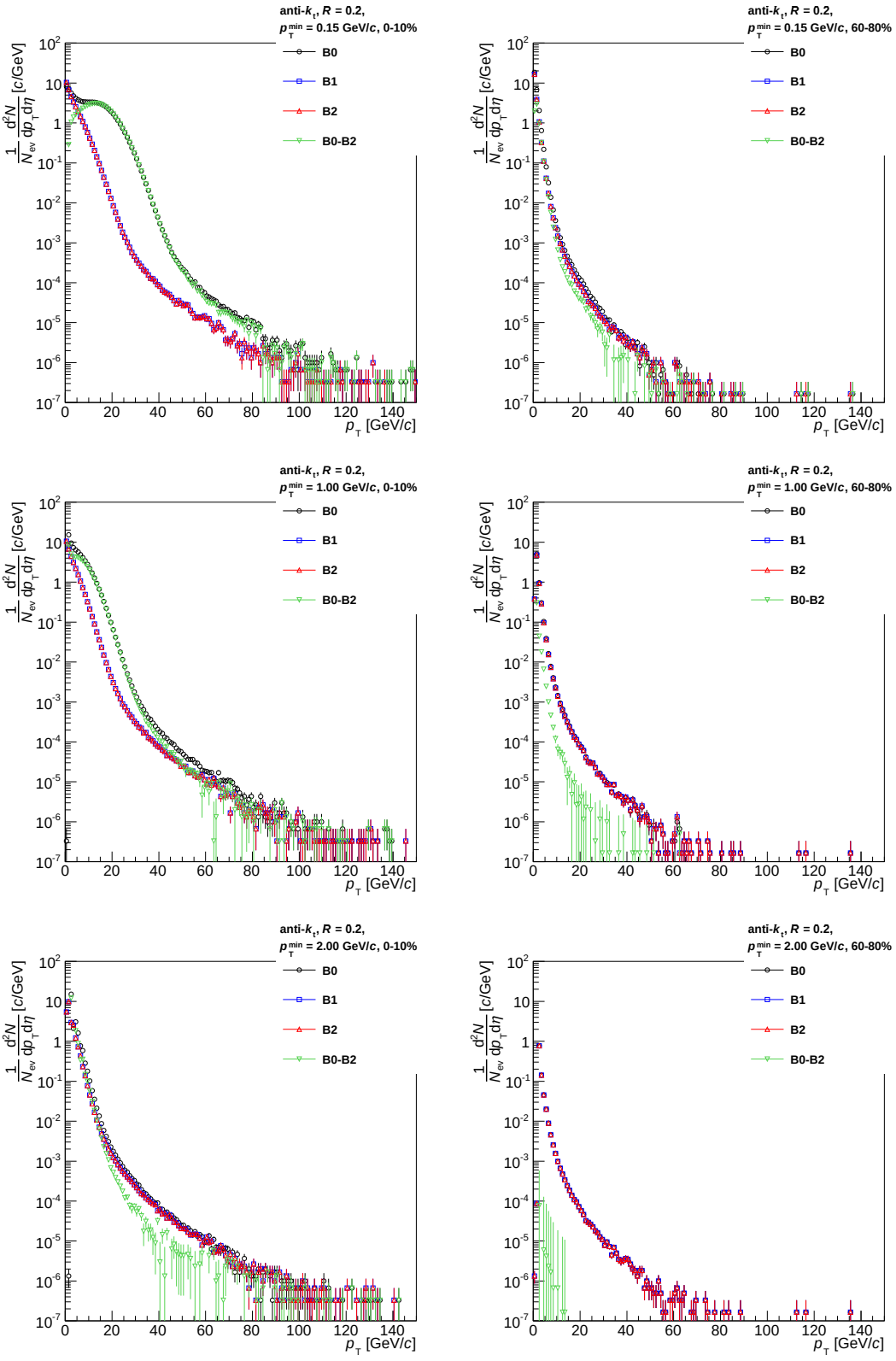

Figure 6.33: Influence of background on p_{T} spectra for the most central and the most peripheral collisions. Pb + Pb, 2010, $\sqrt{s_{\mathrm{NN}}} = 2.76$ TeV, anti-k_{t}, $R = 0.2$.

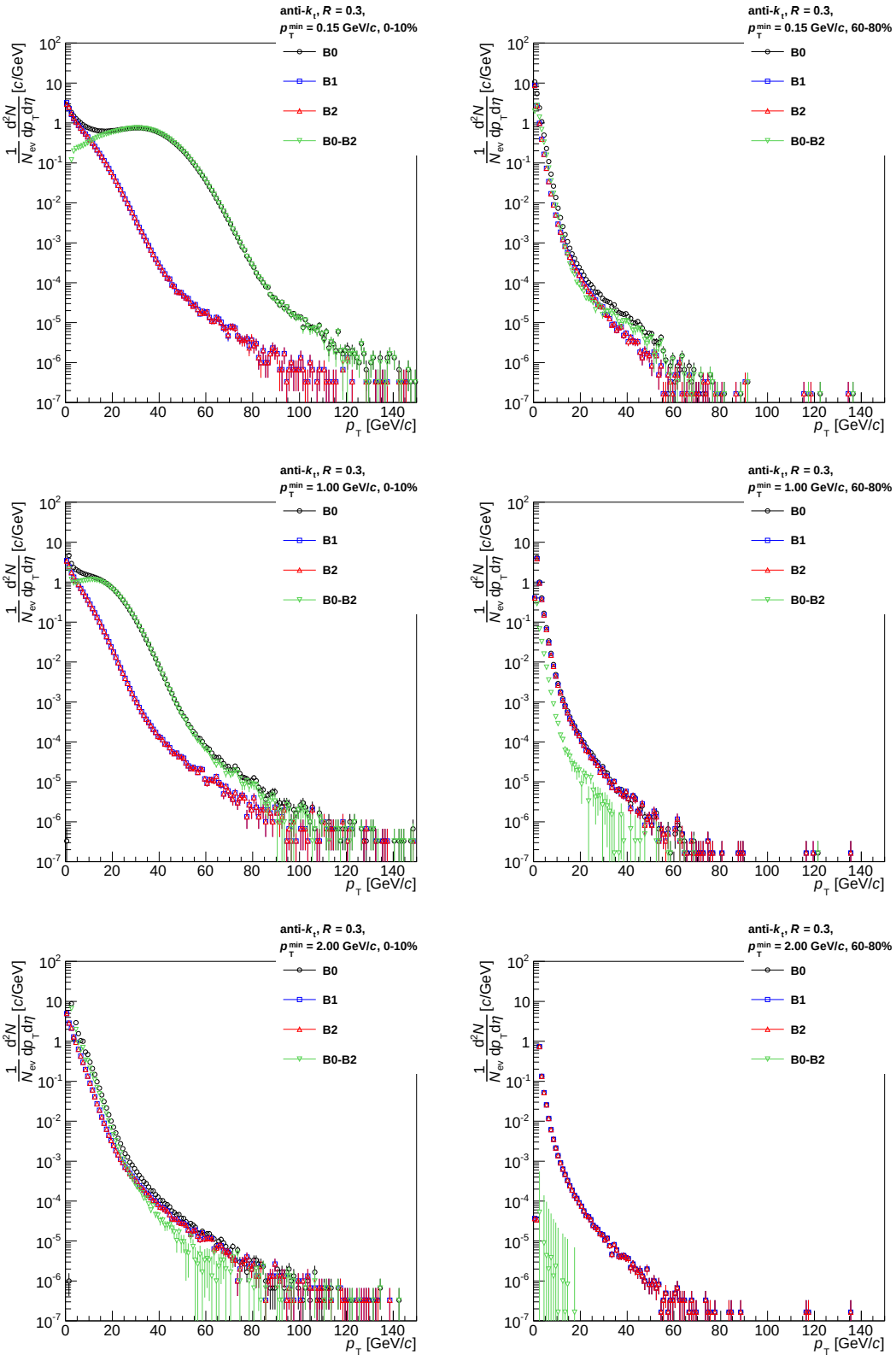

Figure 6.34: Influence of background on p_{T} spectra for the most central and the most peripheral collisions. Pb + Pb, 2010, $\sqrt{s_{\mathrm{NN}}} = 2.76$ TeV, anti-k_{t}, $R = 0.3$.

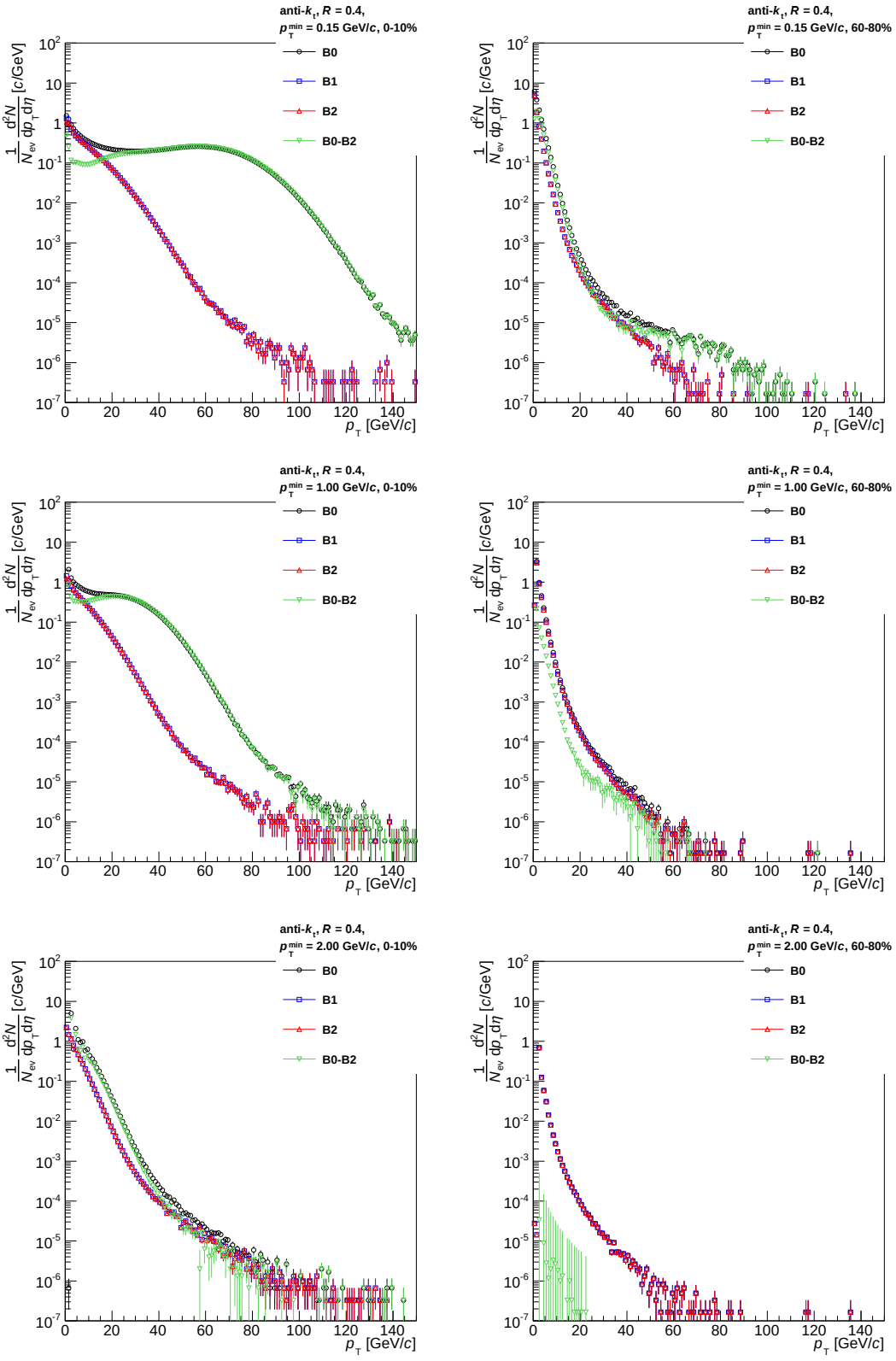

Figure 6.35: Influence of background on p_{T} spectra for the most central and the most peripheral collisions. Pb + Pb, 2010, $\sqrt{s_{\mathrm{NN}}} = 2.76$ TeV, anti-k_{t}, $R = 0.4$.

comparison of shapes of (previously presented) spectra after vector subtraction for $R = 0.2, 0.3, 0.4$.

If one assumes that the background subtraction was applied properly, it is appropriate to deduce from these figures that a broadening of jets in the central collisions relative to the peripheral collisions is observed.

If lower R was sufficient to include all the p_{T} of a jet, using higher R would add more background p_{T} to the raw jets but should not modify the p_{T} spectra after subtraction. The increase of (density of) probability of finding a jet with $p_{\mathrm{T}} \approx 40\mathrm{GeV}/c$ and decrease of probability of finding a jet with low p_{T}, both caused by increasing R, implies that wider cone is needed to include all constituents of that jet.

Because this is manifested only for the most central and semi-central collisions, whereas increasing R does not affect p_{T} spectra for peripheral collisions, it seems that jets in the central collisions are broader than jets in the peripheral collisions. The effect is stronger for lower $p_{\mathrm{T}}^{\mathrm{min}}$ which indicated that this broadening is mainly due to soft particles in jets.

Such statements are however weak since based on observation of uncorrected spectra.

6.3.5 R_{CP}

Figures 6.39, 6.40, 6.41 show the uncorrected ratio R_{CP} (see definition (2.4)) for chosen values of R. Each figure presents plots for three values of $p_{\mathrm{T}}^{\mathrm{min}}$, each plot includes data sets for all four pairs of centrality bins where the fixed reference bin is represented by the most peripheral collisions. Individual p_{T} spectra (after vector subtraction of background) were additionally normalised by the mean numbers of binary nucleon collisions, presented in Table 6.1. Spectra ratios were afterwards rebinned to bins of width of 5 GeV/c and normalised again by the rebinning factor 5. Systematic errors corresponding to $R_{\mathrm{CP}} = 1$, propagated from errors of N_{coll} presented in Table 6.1, are indicated by colour boxes.

There is an obvious strong suppression of jet production for $p_{\mathrm{T}} > 60$ GeV/c. Values of R_{CP} depend strongly on R for $p_{\mathrm{T}} < 50$ GeV/c. This dependence is suppressed in case of higher $p_{\mathrm{T}}^{\mathrm{min}}$.

However, drawing any final physics conclusions from these results would not be appropriate since the presented uncorrected jet spectra are missing further corrections such as including background fluctuations, detector effects (tracking efficiency, resolution of measurements,...) which is beyond the scope of this diploma thesis. For the sake of comparison, results of my uncorrected R_{CP} measurement are presented in Fig. 6.42 together with the ALICE preliminary results shown recently at the Hard Probes 2012 conference [35], where the mentioned corrections were applied. There is a striking difference which reminds about the importance of taking all factors which affect measurements into consideration.

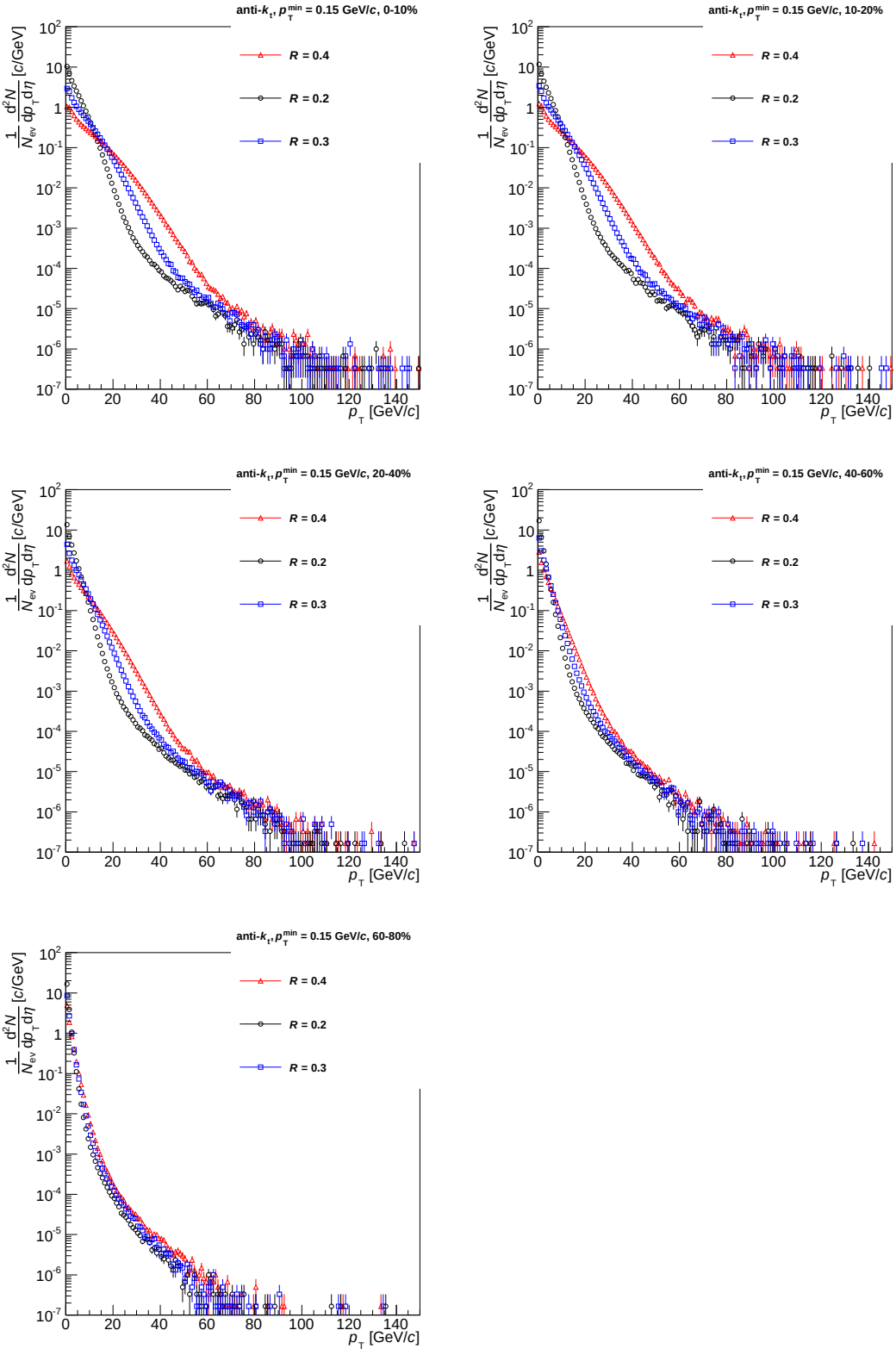

Figure 6.36: Influence of R on p_{T} spectra. Pb + Pb, 2010, $\sqrt{s_{\mathrm{NN}}} = 2.76$ TeV, anti-k_{t}, $p_{\mathrm{T}}^{\mathrm{min}} = 0.15\,\mathrm{GeV}/c$, B2.

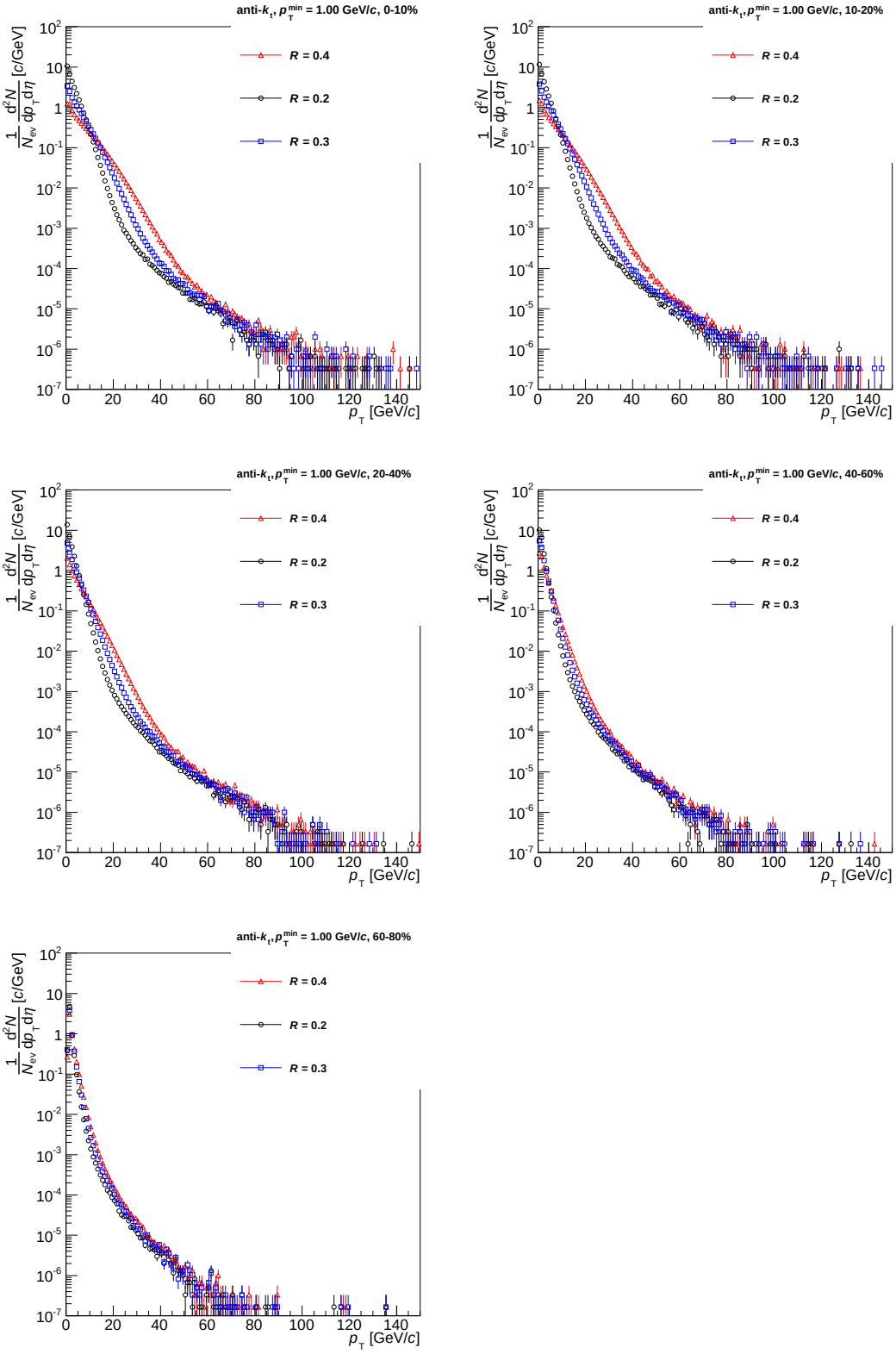

Figure 6.37: Influence of R on p_{T} spectra. Pb + Pb, 2010, $\sqrt{s_{\mathrm{NN}}} = 2.76$ TeV, anti-k_{t}, $p_{\mathrm{T}}^{\mathrm{min}} = 1$ GeV/c, B2.

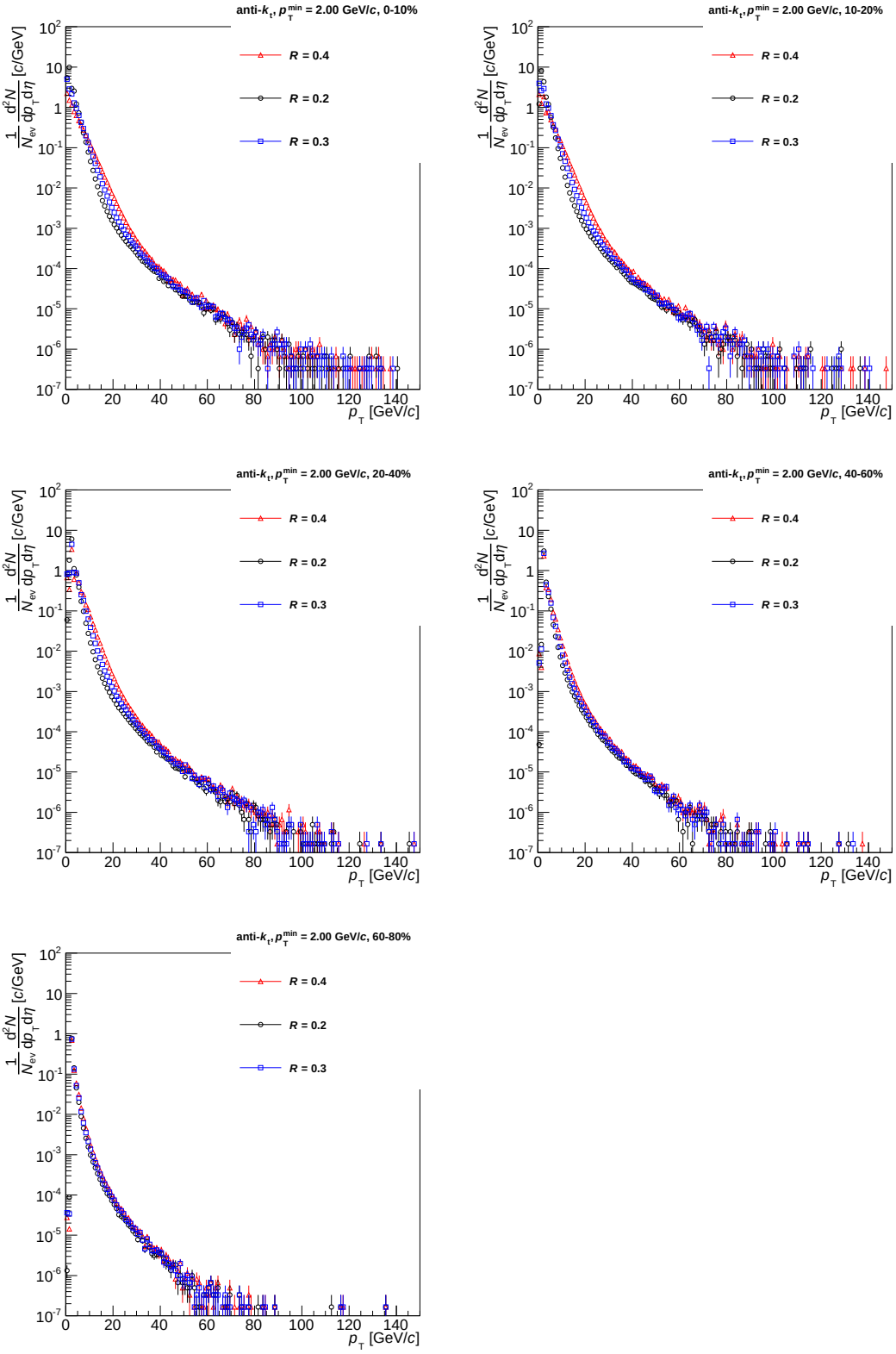

Figure 6.38: Influence of R on p_{T} spectra. Pb + Pb, 2010, $\sqrt{s_{\mathrm{NN}}} = 2.76$ TeV, anti-k_{t}, $p_{\mathrm{T}}^{\mathrm{min}} = 2\,\mathrm{GeV}/c$, B2.

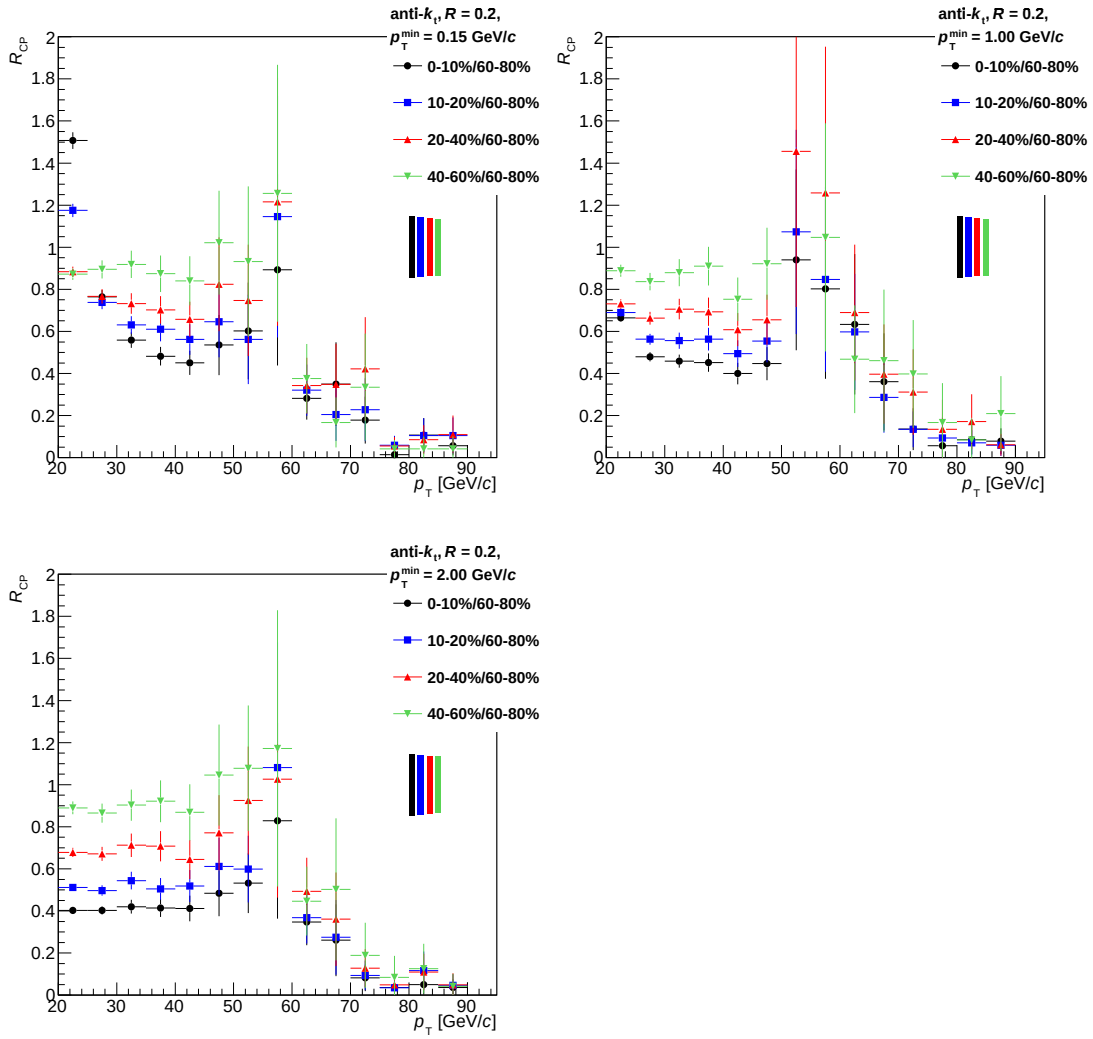

Figure 6.39: R_{CP}. Pb + Pb, 2010, $\sqrt{s_{\mathrm{NN}}} = 2.76$ TeV, anti-k_{t}, $R = 0.2$.

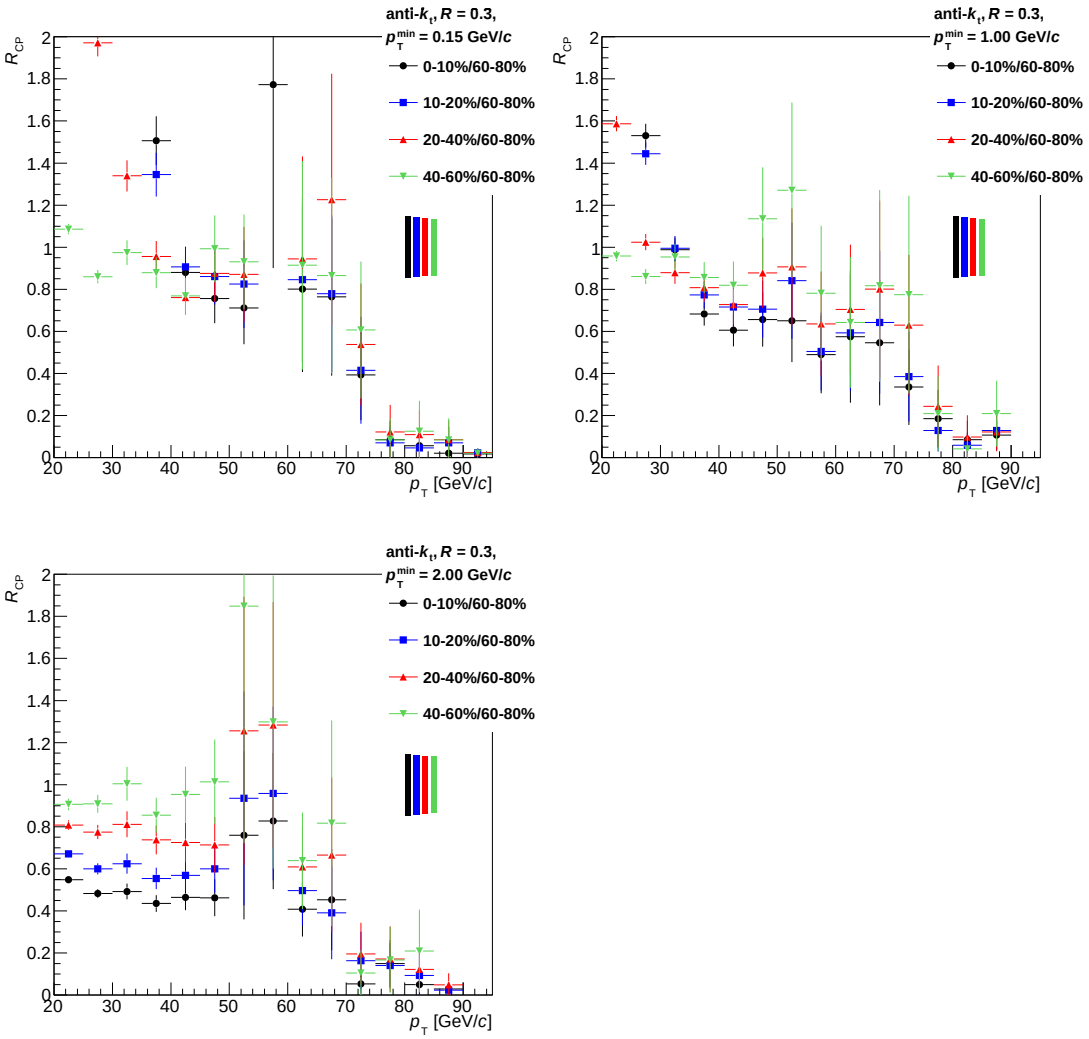

Figure 6.40: R_{CP}. Pb + Pb, 2010, $\sqrt{s_{\mathrm{NN}}} = 2.76$ TeV, anti-k_{t}, $R = 0.3$.

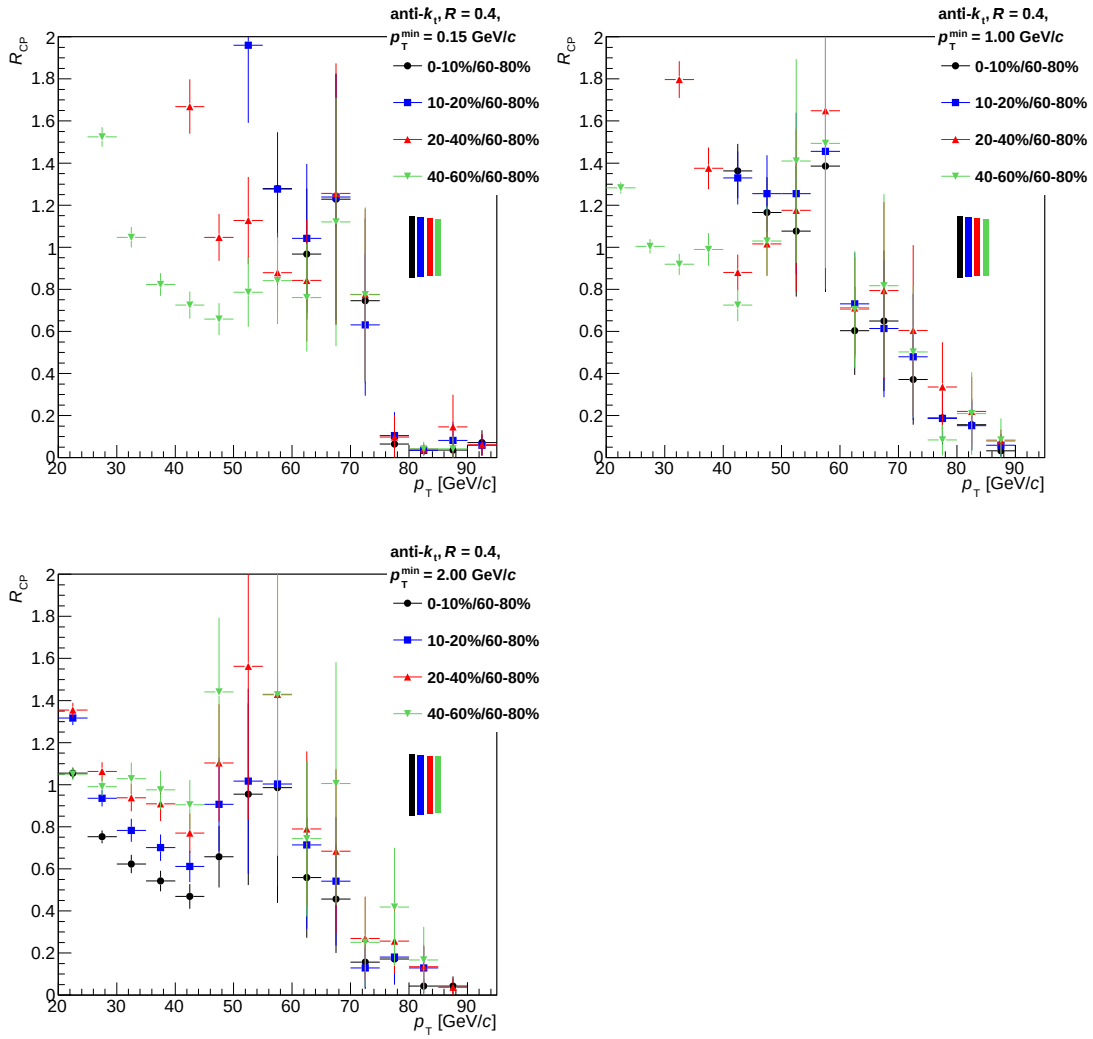

Figure 6.41: R_{CP}. Pb + Pb, 2010, $\sqrt{s_{\mathrm{NN}}} = 2.76$ TeV, anti-k_{t}, $R = 0.4$.

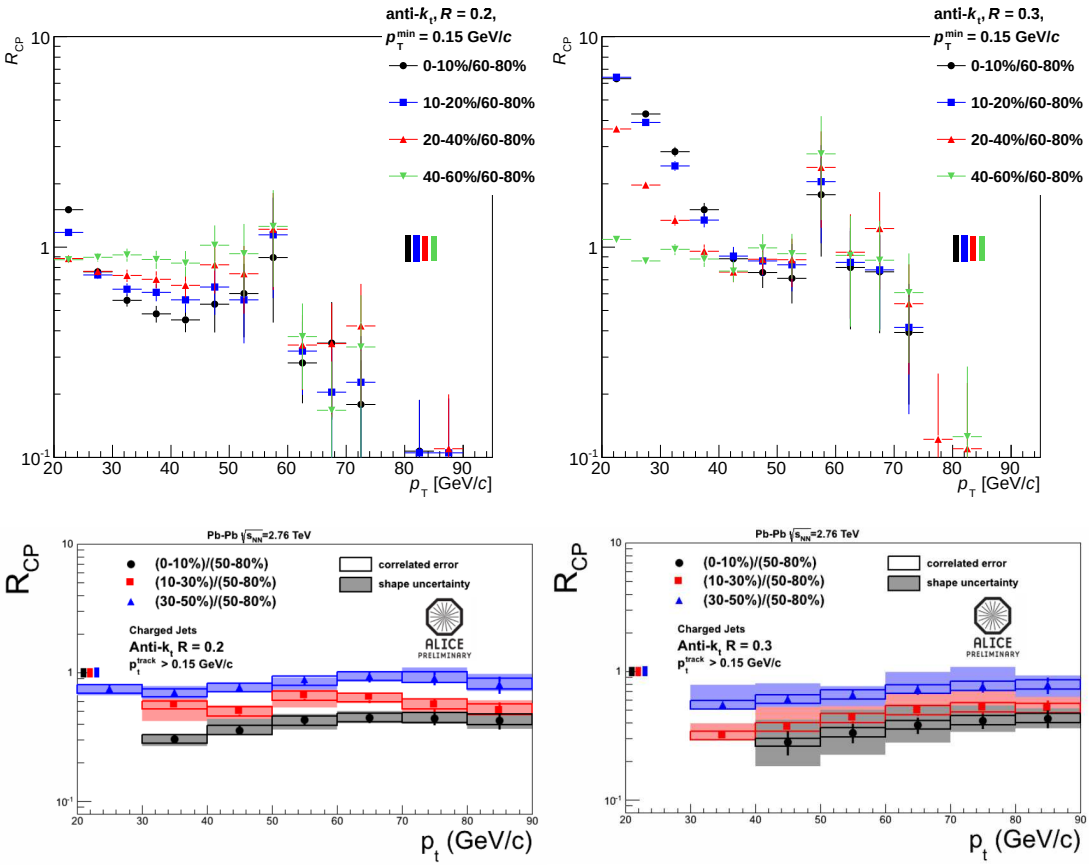

Figure 6.42: Comparison of my results (upper row) with published corrected R_{CP} [35] (lower row) for anti-k_{t}, $R = 0.2$ (left column), $R = 0.3$ (right column), $p_{\mathrm{T}}^{\mathrm{min}} = 0.15\,\mathrm{GeV}/c$. Pb + Pb, 2010, $\sqrt{s_{\mathrm{NN}}} = 2.76\,\mathrm{TeV}$.

Conclusions

The goal of this diploma thesis was to study production of charged jets in Pb+Pb collisions at $\sqrt{s_{\mathrm{NN}}} = 2.76$ TeV measured by the ALICE experiment at the LHC at CERN and to investigate its modification by the strongly interacting matter created in ultra-relativistic heavy-ion collisions.

I used charged tracks measured by the ITS and the TPC of the ALICE experiment to reconstruct jet candidates. The jet candidates were reconstructed using cone algorithms (UA1, SISCone) as well as modern sequential recombination algorithms (k_{t}, anti-k_{t}). Jet candidates were compared in terms of number of jets per event and p_{T} spectra, both before and after background subtraction. For the highest of used values of the minimum transverse momentum of tracks accepted for jet reconstruction $p_{\mathrm{T}}^{\mathrm{min}} = 2$ GeV/c, the p_{T} spectra in each bin of collision centrality look similar for all algorithms.

For the final analysis, jet candidates reconstructed with the anti-k_{t} algorithm were used as "signal" jets and candidates reconstructed with the k_{t} algorithm were used for background analysis and subtraction. I applied a scalar and a 4-vector method of background subtraction and studied obtained inclusive jet spectra.

In order to determine how underlying event affects measurements of jets, I studied in detail properties of the background density of transverse momenta and its fluctuations. In particular, I investigated the dependence on collision centrality, on resolution parameter R and on the $p_{\mathrm{T}}^{\mathrm{min}}$ threshold. The highest background density was found to be in the most central collisions, as expected. This contribution can be reduced by increasing $p_{\mathrm{T}}^{\mathrm{min}}$. I found that the reasonable range of R for estimating the background density in Pb + Pb collisions is 0.2–0.4. Lower values produce significantly underestimated density values, higher values produce larger fluctuations and slight overestimation.

I studied the background fluctuations with use of the distribution of p_{T} deviation in randomly oriented cones with respect to the mean background density. Including the hardest jet candidates leads to higher positive fluctuations. Increasing the R values increases the number of tracks inside random cones which makes the δp_{T} distribution wider. The influence of increasing $p_{\mathrm{T}}^{\mathrm{min}}$ is here manifested again by reduction of the width of the δp_{T} distribution.

Both used methods of background subtraction result in almost identical p_{T} spectra. The contribution of background to the p_{T} spectra of "signal"-jet candidates is up to several orders of magnitude higher in the most central collisions than in the peripheral collisions.

The comparison of background subtracted jet p_{T} spectra for different values of R could possibly indicate jet broadening in the central relative to the peripheral Pb + Pb collisions. Similarly, the measured R_{CP} values might point to a strong suppression of the jet production for $p_{\mathrm{T}} > 60$ GeV/c. However, a further analysis, incorporating corrections through unfolding of background fluctuations and of detector effects (efficiency of track reconstruction, momentum resolution), is needed to draw final physics conclusions.

Apart from the main topic of this thesis, I also engaged in monitoring the Silicon Drift Detectors of the ALICE experiment within a short-term project focused on studying data from drift-speed calibration.

Bibliography

[1] U. W. Heinz. *Concepts of heavy ion physics.* arXiv:hep-ph/0407360v1.

[2] K. Aamodt *et al.* [ALICE Collaboration]. *Centrality dependence of the charged-particle multiplicity density at mid-rapidity in* Pb-Pb *collisions at* $\sqrt{s_{\mathrm{NN}}} = 2.76$ TeV. Phys. Rev. Lett. **106** (2011) 032301. arXiv:1012.1657v2 [nucl-ex].

[3] U. Heinz, M. Jacob. *Evidence for a new state of matter: An Assessment of the results from the CERN lead beam programme.* arXiv:nucl-th/0002042v1.

[4] Jochen Wambach. *Phases of Strongly-Interacting Matter.* `http://physik.uni-graz.at/~dk-user/talks/Wambach20090119.pdf`.

[5] M. L. Miller, K. Reygers, S. J. Sanders, P. Steinberg. *Glauber modeling in high energy nuclear collisions.* Ann. Rev. Nucl. Part. Sci. **57** (2007) 205. arXiv:nucl-ex/0701025v1.

[6] The ALICE Collaboration *et al.* 2006. *ALICE: Physics performance report, volume II.* J. Phys. G **32** (2006) 1295. doi:10.1088/0954-3899/32/10/001.

[7] T. Renk, H. Holopainen, R. Paatelainen, K. J. Eskola. *Systematics of the charged-hadron* P_T *spectrum and the nuclear suppression factor in heavy-ion collisions from* $\sqrt{s_{\mathrm{NN}}} = 200$ GeV *to* $\sqrt{s_{\mathrm{NN}}} = 2.76$ TeV. Phys. Rev. C **84** (2011) 014906. arXiv:1103.5308v2 [hep-ph].

[8] C. Marquet, T. Renk. *Jet quenching in the strongly-interacting quark-gluon plasma.* Phys. Lett. B **685** (2010) 270. arXiv:0908.0880v2 [hep-ph].

[9] Jana Bielčíková, private communication.

[10] K. Adcox *et al.* [PHENIX Collaboration]. *Suppression of hadrons with large transverse momentum in central* Au + Au *collisions at* $\sqrt{s_{\mathrm{NN}}} = 130$ GeV. Phys. Rev. Lett. **88** (2002) 022301. arXiv:nucl-ex/0109003v2.

[11] C. Adler *et al.* [STAR Collaboration]. *Centrality dependence of high* p_{T} *hadron suppression in* Au + Au *collisions at* $\sqrt{s_{\mathrm{NN}}} = 130$ GeV. Phys. Rev. Lett. **89** (2002) 202301. arXiv:nucl-ex/0206011v2.

[12] C. Adler *et al.* [STAR Collaboration]. *Disappearance of back-to-back high* p_{T} *hadron correlations in central* Au + Au *collisions at* $\sqrt{s_{\mathrm{NN}}} = 200$ GeV. Phys. Rev. Lett. **90** (2003) 082302. arXiv:nucl-ex/0210033v1.

[13] S. Salur [STAR Collaboration]. *First direct measurement of jets in* $\sqrt{s_{\mathrm{NN}}} =$ 200 GeV *heavy ion collisions by STAR*. Eur. Phys. J. C **61** (2009) 761. arXiv:0809.1609v1 [nucl-ex].

[14] M. Płoskoń for the STAR Collaboration. *Inclusive cross section and correlations of fully reconstructed jets in* $\sqrt{s_{\mathrm{NN}}} = 200$ GeV Au + Au *and* p + p *collisions*. Nucl. Phys. A **830** (2009) 255C. arXiv:0908.1799v3 [nucl-ex].

[15] G. Aad *et al.* [ATLAS Collaboration]. *Observation of a centrality-dependent dijet asymmetry in lead-lead collisions at* $\sqrt{s_{\mathrm{NN}}} = 2.76$ TeV *with the ATLAS detector at the LHC*. Phys. Rev. Lett. **105** (2010) 252303. arXiv:1011.6182v2 [hep-ex].

[16] The CMS Collaboration. *Centrality dependence of the nuclear modification factor for charged particle transverse momentum spectra in PbPb collisions at* $\sqrt{s_{\mathrm{NN}}} = 2.76$ TeV. `http://cdsweb.cern.ch/record/1352777`.

[17] G. C. Blazey *et al. Run II jet physics*. arXiv:hep-ex/0005012v2.

[18] G. P. Salam, G. Soyez. *A practical Seedless Infrared-Safe Cone jet algorithm*. JHEP **0705** (2007) 086. arXiv:0704.0292v2 [hep-ph].

[19] M. Cacciari, G. P. Salam. *Dispelling the* N^3 *myth for the* k_t *jet-finder*. Phys. Lett. B **641** (2006) 57. arXiv:hep-ph/0512210v2.

[20] M. Cacciari, G. P. Salam, G. Soyez. *The anti-*k_t *jet clustering algorithm*. JHEP **0804** (2008) 063. arXiv:0802.1189v2 [hep-ph].

[21] ALICE — A Large Ion Collider Experiment. `http://aliceinfo.cern.ch/`.

[22] CERN Communication Group. *CERN FAQ — LHC the guide*. `http://cdsweb.cern.ch/record/1165534/files/CERN-Brochure-2009-003-Eng.pdf`.

[23] The ALICE Collaboration *et al.* 2004. *ALICE: Physics performance report, volume I*. J. Phys. G **30** (2004) 1517. doi:10.1088/0954-3899/30/11/001.

[24] R. Bellwied for the ALICE EMCal Collaboration. *ALICE EMCal physics performance report*. arXiv:1008.0413v1 [physics.ins-det].

[25] ALICE Offline Pages. `http://aliweb.cern.ch/Offline/`.

[26] Marta Verweij, private communication.

[27] CentStudies < ALICE < TWiki.
https://twiki.cern.ch/twiki/bin/viewauth/ALICE/CentStudies.

[28] K. Aamodt *et al.* [ALICE Collaboration]. *The ALICE experiment at the CERN LHC.* JINST **3** (2008) S08002.
doi:10.1088/1748-0221/3/08/S08002.

[29] MonALISA Repository for ALICE.
https://alimonitor.cern.ch/.

[30] ROOT | A Data Analysis Framework.
http://root.cern.ch/.

[31] Massimo Venaruzzo, private communication.

[32] Worldwide LHC Computing Grid.
http://wlcg.web.cern.ch/.

[33] AliEn.
http://alien2.cern.ch/.

[34] B. Abelev *et al.* [ALICE Collaboration]. *Measurement of event background fluctuations for charged particle jet reconstruction in* Pb-Pb *collisions at* $\sqrt{s_{\mathrm{NN}}} = 2.76$ TeV. JHEP **1203** (2012) 053.
arXiv:1201.2423v1 [hep-ex].

[35] Marta Verweij. *Measurement of jet spectra in* Pb-Pb *collisions at* $\sqrt{s_{\mathrm{NN}}} = 2.76$ TeV *with the ALICE detector at the LHC.* Presented at the Hard Probes 2012 conference.
http://agenda.infn.it/contributionDisplay.py?contribId=67
&sessionId=20&confId=4157.

List of Tables

List of Figures

Terminology

b impact parameter of colliding objects, see Sec. 1.3.

Big Bang hypothetical origin of the Universe.

c speed of light in vacuum.

centrality quantity directly related to impact parameter of colliding nuclei, see Sec. 1.3.

E energy.

e_{cr} critical density of energy at phase transition between hadronic matter and quark-gluon plasma.

E_{T} transverse energy, $E_{\mathrm{T}} = E \sin\theta$.

η pseudorapidity, see definition (2.1).

event recorded data of detected collision(s).

ϕ azimuth angle of spherical coordinate system.

jet collimated spray of particles associated with a cascade of successive emissions of partons induced by a parton created in an initial hard scattering.

μ_{B} baryon chemical potential.

m_{N} mass of nucleon.

N_{coll} number of binary nucleon-nucleon collisions, see definition (1.1).

N_{ev} number of events.

N_{part} number of participating nucleons, see Sec. 1.3.

p proton.

Pb lead nucleus.

p norm of the vector of momentum.

P 4-vector of momentum.

p vector of momentum.

primary vertex place of a collision.

p_{T} transverse momentum with respect to the collision axis.

$p_{\mathrm{T}}^{\mathrm{min}}$ minimum p_{T} of tracks accepted for jet reconstruction.

$\hat{q}$ transport coefficient of medium, see definition (1.5).

R resolution parameter of jet algorithms.

r distance from the z axis.

R_{AA} nuclear modification factor, see definition (2.3).

R_{CP} ratio of p_{T} spectra describing the modification of spectrum in central collisions relative to the most peripheral collisions, see definition (2.4).

ρ background density of transverse momenta, see definition (2.2).

ρ_{coll} density of production points in an overlap region of two nuclei, see definition (1.2).

$\sqrt{s_{\mathrm{NN}}}$ collision energy per nucleon pair in the centre-of-mass system, see Chap. 6.

T thermodynamic temperature.

T_{A} transverse nuclear density of nucleus A, see definition (1.3).

T_{cr} critical temperature at phase transition between hadronic matter and quark-gluon plasma.

θ polar angle of spherical coordinate system, see definition (2.1).

y rapidity.

z coordinate measured along the beam pipe axis (apparatus axis).

z_{v} z coordinate of the primary vertex.

List of abbreviations and acronyms

ALICE A Large Ion Collider Experiment,
`http://aliceinfo.cern.ch/Public/Welcome.html`.

AOD Analysis Object Data.

CERN l'Organisation européenne pour la Recherche nucléaire (European Organization for Nuclear Research),
`http://cern.ch/`.

EMCal Electromagnetic Calorimeter.

ESD Event Summary Data.

FMD Forward Multiplicity Detector.

HMPID High-Momentum Particle Identification Detector.

ITS Inner Tracking System.

LHC Large Hadron Collider,
`http://public.web.cern.ch/public/en/LHC/LHC-en.html`.

MOS Metal-Oxide Semiconductor.

PHOS Photon Spectrometer.

PMD Photon Multiplicity Detector.

PWG Physics Working Group.

QCD Quantum Chromodynamics.

QGP Quark-Gluon Plasma.

RHIC Relativistic Heavy Ion Collider.

RICH Ring Imaging Cherenkov counter.

SDD Silicon Drift Detector.

SPD Silicon Pixel Detector.

SPS Super Proton Synchrotron.

SSD Silicon Strip Detector.

TOF Time-Of-Flight detector.

TPC Time-Projection Chamber.

TRD Transition-Radiation Detector.

ZDC Zero-Degree Calorimeter.

A Table of analysed runs

Table A.1: List of analysed runs.

139510	139507	139505	139503	139465	139438	139437	139360	139329	139328
139314	139310	139309	139173	139107	139105	139038	139037	139036	139029
139028	138872	138871	138870	138837	138732	138730	138666	138662	138653
138652	138638	138624	138621	138583	138582	138579	138578	138534	138469
138442	138439	138438	138396	138364	138275	138225	138201	138197	138192
138190	137848	137844	137752	137751	137724	137722	137718	137704	137693
137692	137691	137686	137685	137639	137638	137608	137595	137549	137546
137544	137541	137539	137531	137530	137443	137441	137440	137439	137434
137432	137431	137430	137366	137243	137236	137235	137232	137231	137230
137162	137161	137135							